UAB
Universitat Autònoma
de Barcelona

Treball de Fi de Grau

Grau en Enginyeria de Sistemes de Telecomunicació

Enhancing 5G Positioning with Reconfigurable Intelligent Surfaces

Antoni Hidalgo González

Director: Francisco Jose Fabra Cervellera

Departament de Telecomunicació i Enginyeria de Sistemes

Universitat Autònoma de Barcelona

Bellaterra, Juny 29, 2025

Abstract

As carrier frequencies continue to rise in search of ever-wider bandwidths, the march toward 6G promises to make both communication and positioning more challenging. Reconfigurable Intelligent Surfaces are poised to become a cornerstone of the next-generation landscape, widening coverage at these higher bands while improving link reliability and localization accuracy.

This thesis first outlines the specific obstacles that 6G deployments must confront and explains how RIS technology can mitigate them. It then presents a full 5G NR positioning simulation that incorporates a RIS, demonstrating, through quantitative results, how such surfaces can materially enhance performance in practice and which are the difficulties to overcome.

Resum

A mesura que les freqüències portadores continuen augmentant per aconseguir amplades de banda cada cop més grans, l'arribada del 6G promet complicar tant la comunicació com la localització. Les superfícies intel·ligents reconfigurables (RIS) es perfilen com una pedra angular del panorama de la propera generació, ja que amplien la cobertura en aquestes bandes més altes alhora que milloren la fiabilitat dels enllaços i la precisió de la localització.

Aquesta tesi descriu primer els obstacles específics que cal afrontar en els desplegaments 6G i explica com la tecnologia RIS els pot mitigar. Tot seguit es presenta una simulació completa de posicionament 5G NR que incorpora una RIS i es demostra, mitjançant resultats quantitatius, com aquestes superfícies poden millorar de manera notable el rendiment pràctic i quines dificultats cal superar.

Resumen

A medida que las frecuencias portadoras siguen aumentando para lograr anchos de banda cada vez mayores, la llegada del 6G promete complicar tanto la comunicación como la localización. Las superficies inteligentes reconfigurables (RIS) se presenta como pieza clave del panorama de próxima generación, pues amplían la cobertura en estas bandas más altas y, al mismo tiempo, mejoran la fiabilidad de los enlaces y la precisión de la localización.

Esta tesis expone, en primer lugar, los obstáculos específicos que deben afrontarse en los despliegues 6G y explica cómo la tecnología RIS puede mitigarlos. Después, se presenta una simulación completa de posicionamiento 5G NR que incorpora una RIS, y se demuestra, mediante resultados cuantitativos, cómo estas superficies pueden mejorar de forma significativa el rendimiento práctico y cuáles son las dificultades que aún hay que superar.

Acknowledgments

I would like to sincerely thank Prof. Francisco Fabra for giving me the opportunity to work under his supervision and letting me expand my knowledge in this area. I am also thankful to Daniel Egea, Alda Xhafa, Lucía Pallarés and Raul Romero who kindly met with me to discuss the various RIS scenarios their ideas and feedback were very valuable to this project.

Contents

List of Figures

List of Tables

Glossary of Acronyms and Symbols

Acronyms

RIS	Reconfigurable Intelligent Surface
BS	Base Station
UE	User Equipment
LoS	Line-of-Sight
NLoS	Non-Line-of-Sight
SNR	Signal-to-Noise Ratio
MIMO	Multiple-Input Multiple-Output
OFDM	Orthogonal Frequency-Division Multiplexing
5G NR	Fifth-Generation New Radio
6G	Sixth-Generation Mobile Communications
gNB	Next Generation Node B
ToA	Time of Arrival
AoA	Angle of Arrival
CAPEX	Capital Expenditure
PRISMA	Preferred Reporting Items for Systematic Reviews and Meta-Analyses

Symbols

Symbol	Description	Unit
f_c	Carrier frequency	Hz
B	System bandwidth	Hz
d	Distance BS–UE	m
ϕ	Azimuth angle	deg
θ	Elevation angle	deg
N_{RIS}	Number of reflecting elements	–
n_{RIS}	RIS efficency	–
$\mathbf{G}$	Gain matrix from angular sweep	–
$\widehat{\mathbf{p}}$	Estimated 3-D UE position	m
SNR_{dB}	Signal-to-Noise Ratio (decibel scale)	dB

Chapter 1

Introduction

Over the last two decades, society has become accustomed to geopositioning services enabled by Global Navigation Satellite Systems (GNSS). However, the precision and even the availability of these signals collapses whenever the line of sight to the satellites is obstructed in scenarios such as urban canyons, tunnels, or indoor spaces [12].

The advent of fifth-generation cellular technology (5G) raises the bar: autonomous driving, indoor robotics, and augmented-/mixed-reality demand high-level positions with small latencies, requirements that standalone GNSS cannot fulfill [12]. 5G mitigates part of the problem through network-based positioning and the use of millimetre-wave (mmWave) spectrum, yet moving from sub-6 GHz to mmWave and on the 6G roadmap, to sub-THz makes propagation paths far more vulnerable to blockage, inflating shadow zones and further complicating reliable positioning [13].

Within this scenario, Reconfigurable Intelligent Surfaces (RIS) emerge as a linchpin for 5G-Advanced and, even more decisively, 6G. A RIS is a passive array that tailors the phase, amplitude and polarization of incident waves, creating "on-demand" reflections, focusing radio energy on target regions, and enabling localization where a direct line of sight is degraded [5]. 5G systems assisted by RIS promise proper precision in dense urban or indoor environments while consuming far less energy than active array solutions.

Looking to the next decade, standardization for a predict that 6G will operate in the sub-THz regime, fuse terrestrial and non-terrestrial segments. In that landscape, RIS shift from interesting to almost mandatory, shaping the radio environment and extending coverage where deploying extra base stations is technically or economically unviable.

1.1 Motivation and Objectives

Motivation

Fifth-generation New Radio (5G NR) promises unparalleled data rates and ultra-low latency, but at millimeter-wave frequencies it also faces severe path loss and frequent blockages, issues that undermine both coverage and positioning accuracy. Reconfigurable Intelligent Surfaces (RIS) have emerged as a powerful solution: by dynamically steering and reflecting incident wavefronts, an RIS can create virtual line-of-sight links, enhance signal strength, and introduce additional geometric diversity for localization. This thesis is driven by the need to quantify these benefits. We will begin by explaining the motivation for the use of RIS in next-generation networks, then review the underlying principles of RIS operation, and finally simulate its performance in realistic urban scenarios to evaluate how system parameters influence positioning error and how to minimize it.

Objectives

This Bachelor's Thesis sets out to achieve the following goals:

- **RIS Fundamentals.** Present the theory of intelligent surfaces, covering antenna array principles, element-level beamforming, and the reasons for integrating RIS into 5G/6G deployments.
- **5G NR–RIS System Modeling.** Develop a geometric and channel model that captures both the direct 5G NR path and the RIS-reflected path, including path-loss and array configurations.
- **Beam-Scanning Algorithm Implementation.** Build the RIS gain matrix through systematic azimuth and elevation sweeps, and implement a robust correlation-based routine to extract Angle-of-Departure estimates.
- **MATLAB Simulation and Validation.** Simulate 3D positioning accuracy, validate the results against theoretical predictions, and analyze the impact of RIS geometry, scanning resolution, and SNR.
- **Practical Deployment Guidelines.** Derive design recommendations for RIS element count, sweep step, and power thresholds in urban environments. Assess feasibility with Positioning Reference Signals (PRS) and other 5G waveforms.

Project Timeline

The thesis progressed through five well-defined phases, each with clear deliverables and timeframes:

Phase 1: Index Creation (Dec–Jan). Developed the table of contents and thesis structure, ensuring cohesive chapter flow and identifying key sections for literature, methodology, results, and conclusions.

Phase 2: Foundational Theory & Scenario Analysis (Jan–Mar). Compiled the theoretical background on Reconfigurable Intelligent Surfaces and antenna theory. During this period, we evaluated potential use-cases and methodologies, deciding whether to focus on communications or positioning applications by evaluating candidate urban scenarios and simulation feasibility.

Phase 3: MATLAB Implementation (Mar–May). Chose the positioning use-case and integrated 5G NR fundamentals into the theoretical framework. MATLAB development was initiated simultaneously: parameter initialization, beam-scanning routines, gain-matrix construction, and preliminary position/estimation scripts.

Phase 4: Scenario Selection & Simulation (May–Jun). Selected representative user-location grids and propagation environments. Executed systematic simulations in MATLAB, generating positioning error metrics across the defined grid and evaluated power and delay thresholds.

Phase 5: Theory Refinement & Thesis Composition (Jun–Jul). Polished and completed any remaining theoretical derivations. Consolidated all chapters, integrated simulation results, produced figures and tables, and finalized the document for submission.

This structured timeline ensured steady progress from conceptual groundwork to comprehensive implementation and analysis.

Methodology of the Literature Review

The literature review was planned and conducted as a transparent, traceable process, and the resulting workflow is condensed in the PRISMA 2020 diagram in Figure 1.1. From January 2017 to May 2025 I searched the main scholarly databases (mainly **IEEE Xplore** and with google advance search others **MDPI**, **APL Photonics**, **Electromagnetic Science**) together with

the **arXiv** register. The goal of this first pillar was to understand how the telecommunications sector is currently embracing Reconfigurable Intelligent Surfaces (RIS): deployment architectures, reported gains, hardware impairments and other issues. Search strings combined the descriptors "reconfigurable intelligent surface", "RIS/IRS", "5G localization", "channel modeling" and "hardware impairment" with technology qualifiers such as "5G", "6G", "mmWave" and "THz". Forty-one records were retrieved, and after eliminating two DOI-level duplicates the set provided a solid, up-to-date picture of the state of practice.

A complementary search stream was then pursued "via other methods". Books, notes, white papers from equipment vendors, Third Generation Partnership Project (3GPP) technical reports, specialized blogs (ShareTechnote, Cafetele) and tool documentation (MathWorks, PyLayers) proportioned twenty-three additional documents. This second pillar was deliberately theory-oriented: textbooks and lecture notes supplied the antenna background required to formalize concepts such as the array factor, directivity and near-field behavior, while code snippets and NR-PRS/CSI-RS specification sheets grounded the simulation framework in realistic 5G procedures.

All sixty-two unique records were selected at the title–abstract level, none were rejected. The full text assessment removed 19 papers whose scenario diverged from our outdoor 5G/6G RIS localization focus, and two whose key figures were protected by restrictive copyright.

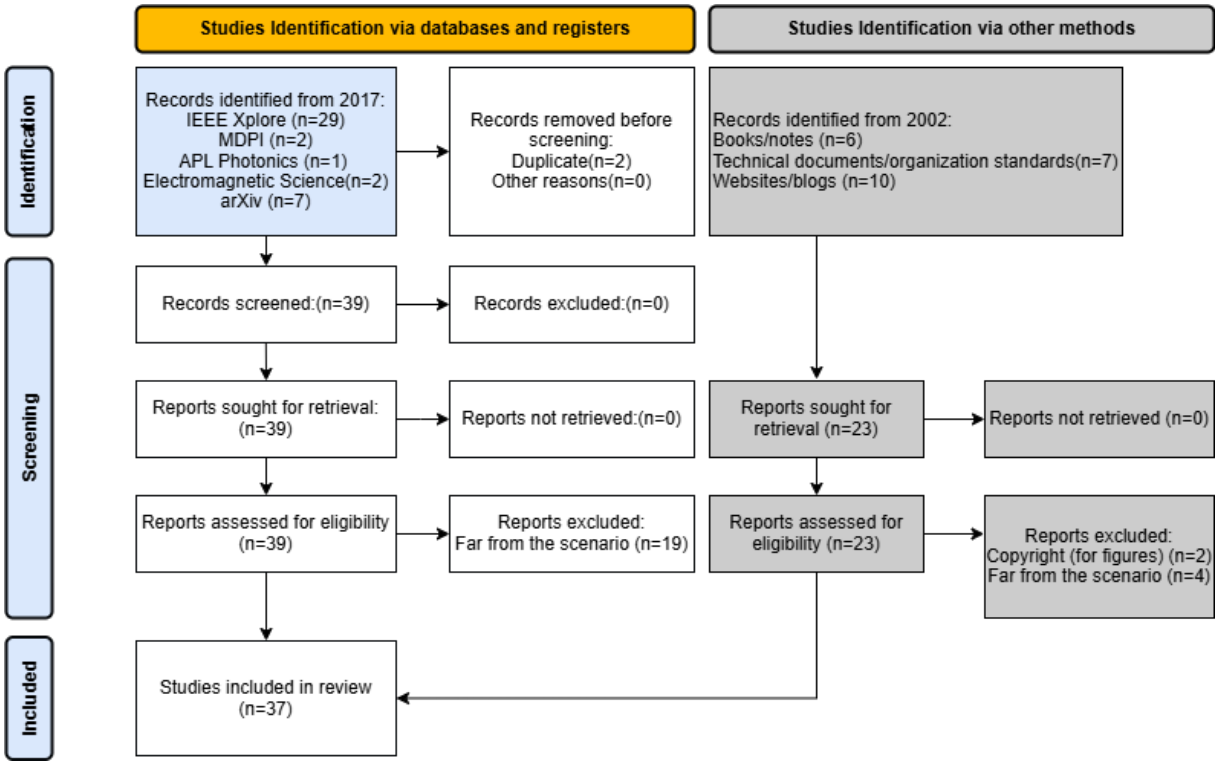

Figure 1.1: PRISMA 2020 flow diagram for the literature review.

Chapter 2

State of the Art

2.1 Overview of Wireless Communications

With the wireless communication advancements, high demand for data rates have led to the use of new frequency bands like millimeter-wave (mmWave) and terahertz (THz) frequencies. Although higher frequency bands provide significant benefits, they pose certain issues, especially towards signal propagation and interference.
This segment discusses the progress made in high-frequency wireless communications, the related reception problems, and the new methods used to mitigate interferences.[14, 15, 16].

2.1.1 Advancements in High-Frequency Wireless Communications

Ultra high frequency bands such as broadband and microwave (30 to 300 GHz) as well as THz ranging from 300 GHz to 3 THz, are being investigated in order to support supporting ultra-quick speed data transfers. The amplification of these particular frequencies is a consequence of the increased demand on the bandwidth and the data transfer rate resulting from stream applications for video and augmented reality. These include, but are not limited to, high-definition videos, virtual reality streaming, and other B5G (Beyond 5G) technology.

Current studies have proven the possibility of real-time wireless communication using a Kerr microcomb at 300GHz with data rates of over 60Gbps [17]. These studies also claim that transmission of wireless data in the GHz band can also be done using low phase noise terahertz waves. This signifies the promise 6G systems offer [18].

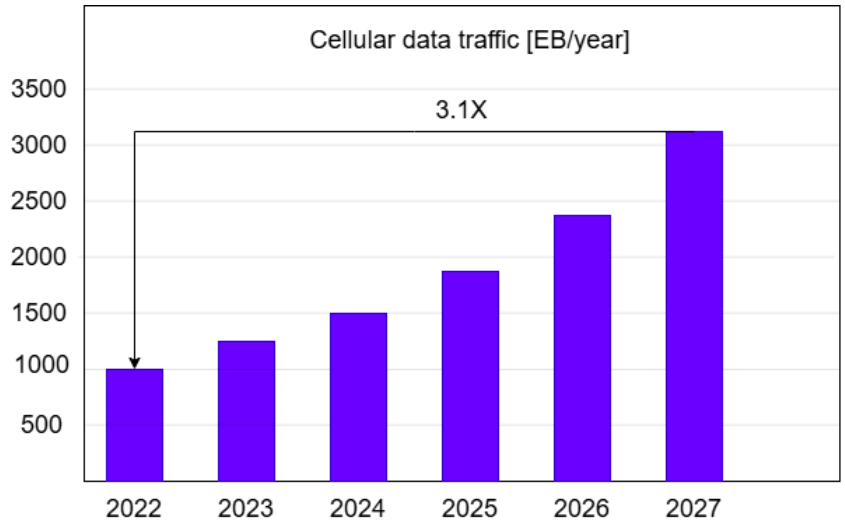

Figure 2.1: Projected growth in cellular data traffic from 2022 to 2027. Increasing data consumption necessitates the use of higher frequency bands to accommodate bandwidth demands. Adapted from Omdia, from [1]

The exponential growth in cellular data traffic, as illustrated in Fig. 2.1, emphasizes the demand for more bandwidth. Traditional sub-6 GHz frequencies are becoming saturated, which is motivating the migration to higher frequency bands.

Received Power and Frequency Dependence

The wavelength λ represents the distance that a wave travels in a complete cycle. It is related to the operating frequency f by:

$$\lambda = \frac{c}{f} \quad \text{where:} \quad \begin{cases} \lambda & \text{wavelength (m),} \\ c & \text{speed of light (m/s),} \\ f & \text{frequency (Hz).} \end{cases} \tag{2.1}$$

Equation extracted from [3]

The Friis transmission equation describes the received power P_r in free space:

$$P_r = P_t G_t G_r \left(\frac{\lambda}{4\pi r}\right)^2 \quad \text{where:} \quad \begin{cases} P_r & \text{received power (W),} \\ P_t & \text{transmitted power (W),} \\ G_t, G_r & \text{gains of transmitting and receiving antennas,} \\ r & \text{distance between antennas (Tx to Rx) (m),} \\ \lambda & \text{wavelength.} \end{cases} \tag{2.2}$$

The effective aperture of an antenna, A_ef, is the aperture by means of which power in an incoming electromagnetic wave is effectively collected and transferred to electrical power by the antenna. Mathematically, it is expressed as:

$$A_{ef} = \frac{D_r \lambda^2}{4\pi} \quad \text{where:} \quad \begin{cases} A_{ef} & \text{effective aperture } (\text{m}^2), \\ D_r & \text{directivity of the receiving antenna,} \\ \lambda^2 & \text{squared wavelength.} \end{cases} \tag{2.3}$$

Equation extracted from [19]

These equations illustrate how higher frequencies result in smaller antennas but also increased path loss, requiring more precise beamforming and higher directivity antennas.

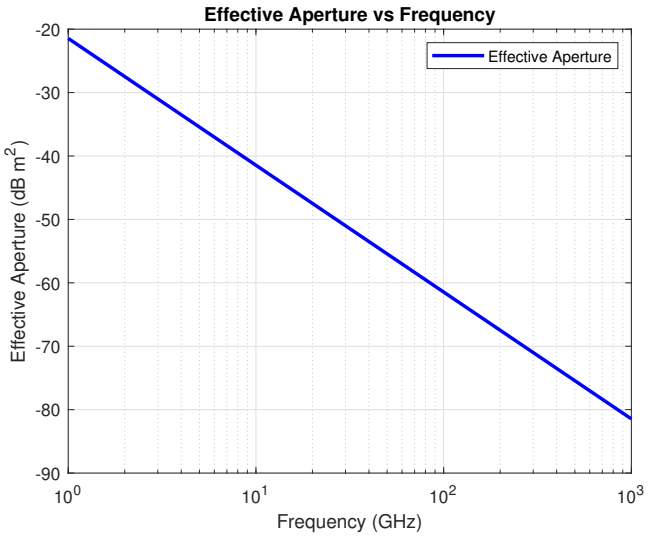

Figure 2.2: Effective aperture of an antenna as a function of frequency. The plot is shown in dB scale, illustrating the inverse relationship between frequency and effective aperture.

When the frequency is increased to support higher bandwidth requirements, the equivalent wavelength diminishes. For instance, within the sub-6 GHz band, the wavelengths are between around 5 cm and 50 cm. But for millimeter-wave (mmWave) bands (30-300 GHz), the wavelengths reduce to the millimeter scale (1 mm to 10 mm), and in the terahertz (THz) band (300 GHz - 3 THz), the wavelengths reduce further to the sub-millimeter scale.

Higher frequency bands provide greater bandwidth and faster data rates but it also carries some challenges in communication.

2.1.2 Challenges in High-Frequency Signal Reception

Despite promising prospects, high-frequency signal propagation faces several challenges [14]:

Propagation Loss

Higher frequencies experience greater loss of free space path, which requires advanced techniques to maintain signal strength over distances. For example, free space losses:

$$\text{FSPL} = \left(\frac{4\pi df}{c}\right)^2 \quad \text{where:} \begin{cases} d & \text{distance transmitter-to-receiver (meters),} \\ f & \text{frequency of the signal (Hz),} \\ c & \text{speed of light in a vacuum (} 3 \times 10^8 \text{ m/s).} \end{cases} \tag{2.4}$$

Equation extracted from [3]

Atmospheric Absorption

Gases like oxygen and water vapor absorb high-frequency signals, leading to attenuation, especially in the THz range.

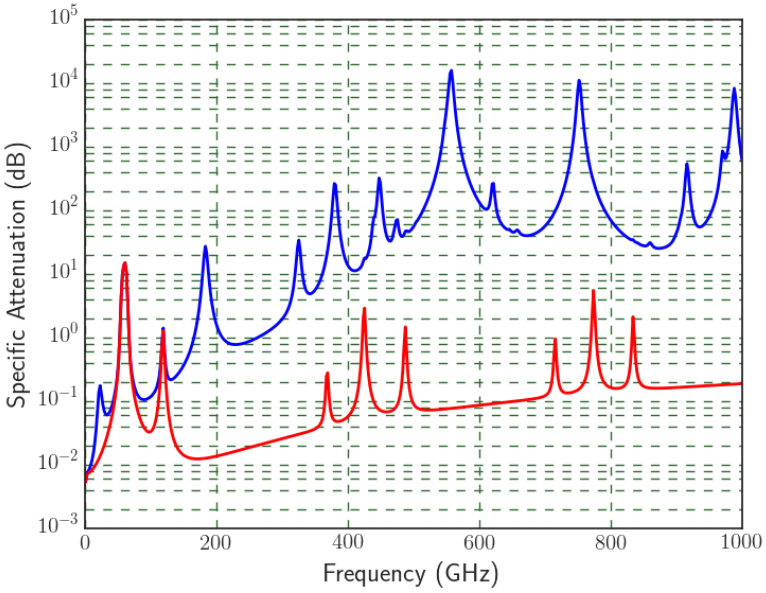

Figure 2.3: **Blue line:** total molecular absorption (O_2+H_2O) under standard conditions (21 °C, 7.5 g/m^3 of water vapor). **Red line:** specific attenuation due to water vapor only. Source: PyLayers from [2].

Obstruction Sensitivity

High-frequency signals are particularly sensitive to blockages caused by obstacles in their propagation path.

Fresnel Zones:
An example of this obstruction are the fresnel zones, which are a series of ellipsoidal regions between a transmitter and a receiver that define areas where obstacles can impact the signal. The principle is based on constructive and destructive interference of electromagnetic waves.

The intersection of Fresnel ellipsoids with an obstruction plane creates circular zones. These zones define regions where obstacles can block or disrupt the signal.

The radius of the n-th Fresnel zone at an obstacle located at a distance d_1 from the transmitter and d_2 from the receiver is given by:

$$r_n = \sqrt{n\lambda \frac{d_1 d_2}{d_1 + d_2}} \quad \text{where:} \begin{cases} r_n & \text{radius of the } n\text{-th Fresnel zone (m)}, \\ \lambda & \text{wavelength of the signal (m)}, \\ d_1, d_2 & \text{distances transmitter/receiver-to-obstacle (m)}. \end{cases} \tag{2.5}$$

Equation extracted from [3]

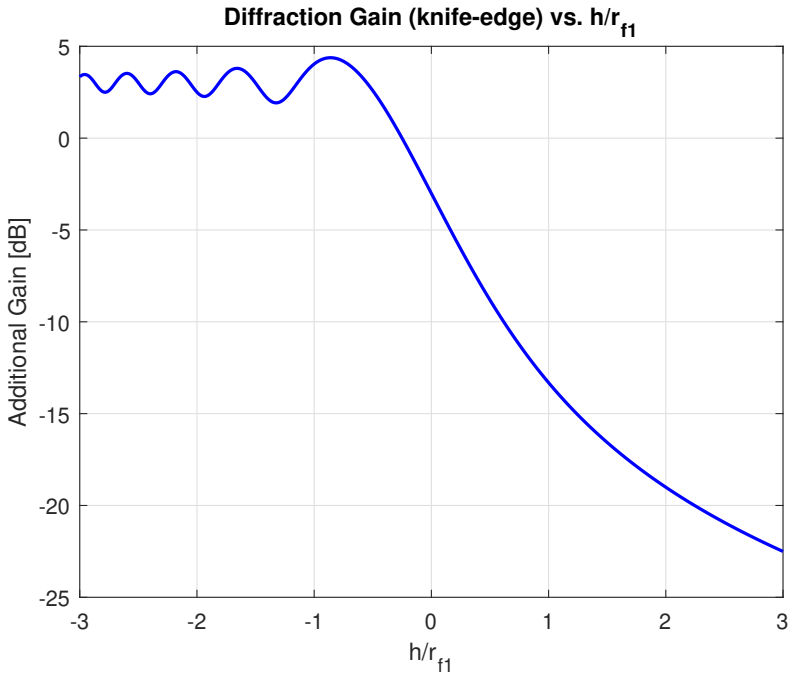

Figure 2.4: Additional gain over free space as a function of the height relative to the first Fresnel radius (h/r_1). Adapted from [3]

In urban areas, where there are numerous obstacles such as buildings and vehicles, the issues with the higher frequencies are more severe. When there are obstacles within the first Fresnel zone ($n = 1$), signal strength and quality are greatly affected by diffraction.

Multipath Effects in High-Frequency Wireless Communications

Multipath propagation is among the severe challenges to high-frequency wireless communication in the millimeter-wave (mmWave) and Terahertz (THz) frequency ranges [20] applied in 6G and future generations. It happens when the transmitted signal arrives at the receiver via several paths as a result of reflection, diffraction, and scattering by objects in the environment. The phenomenon causes constructive and destructive interference and therefore results in signal degradation.

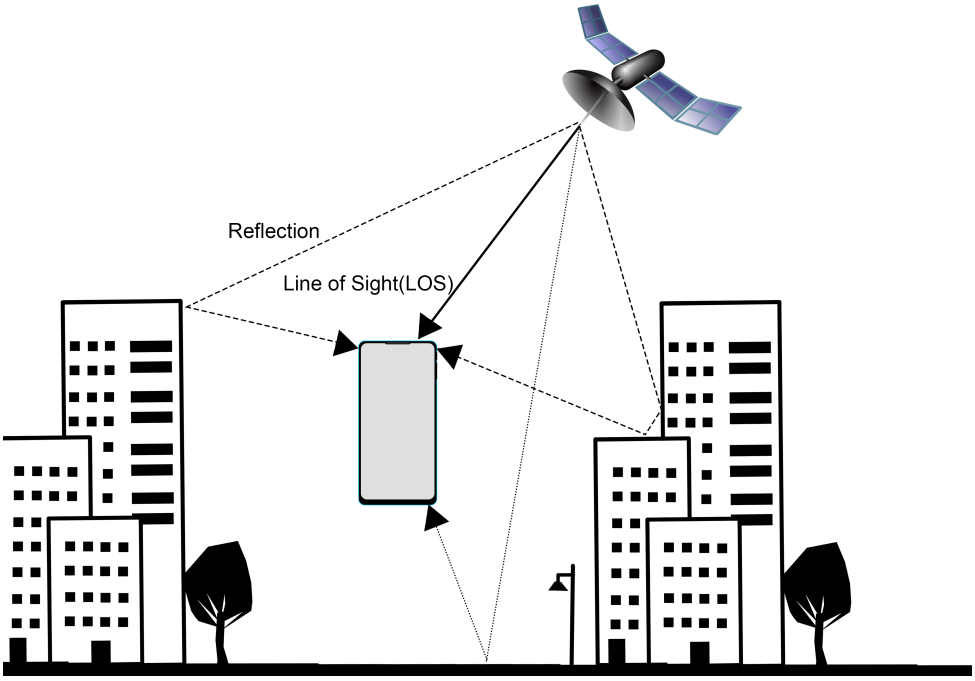

Figure 2.5: Illustration of multipath propagation in high-frequency wireless communication. A transmitted signal from a satellite reaches the receiver through multiple paths due to reflections, diffractions, and scattering from surrounding objects such as buildings. This phenomenon leads to constructive and destructive interference, resulting in signal degradation, fading, delay spread, and Doppler shift.

Multipath Propagation Mechanisms: At high frequencies, multipath effects are exacerbated due to the shorter wavelengths, which make the signals more susceptible to obstacles such as buildings, vehicles, and even atmospheric particles. The main mechanisms of multipath propagation include:

Reflection

Reflections occur when signals encounter smooth surfaces such as walls, glass, and metal structures. At THz frequencies, reflections can be highly directional due to the short wavelength, which affects link reliability and requires precise beam steering.

Diffraction

Diffraction occurs when a wave encounters an obstacle and bends around it. While significant at lower frequencies, diffraction is weaker at mmWave and THz bands due to the small wavelength, resulting in higher penetration losses and reduced coverage in non-line-of-sight (NLoS) conditions.

Scattering

At higher frequencies, such as millimeter-wave (mmWave) and Terahertz (THz) bands, scattering becomes a dominant propagation mechanism due to the reduced wavelength, which makes most surfaces appear rough. The primary scattering mechanisms at these frequencies include diffuse scattering, specular reflection with scattering loss, material-dependent scattering, angle dependency, and frequency dependency.

Diffuse scattering occurs when electromagnetic waves encounter rough surfaces, causing energy to be dispersed in multiple directions rather than reflecting in a single, specular direction. The extent of diffuse scattering is influenced by the surface roughness, which is characterized by parameters such as the root mean square (RMS) height and correlation length.

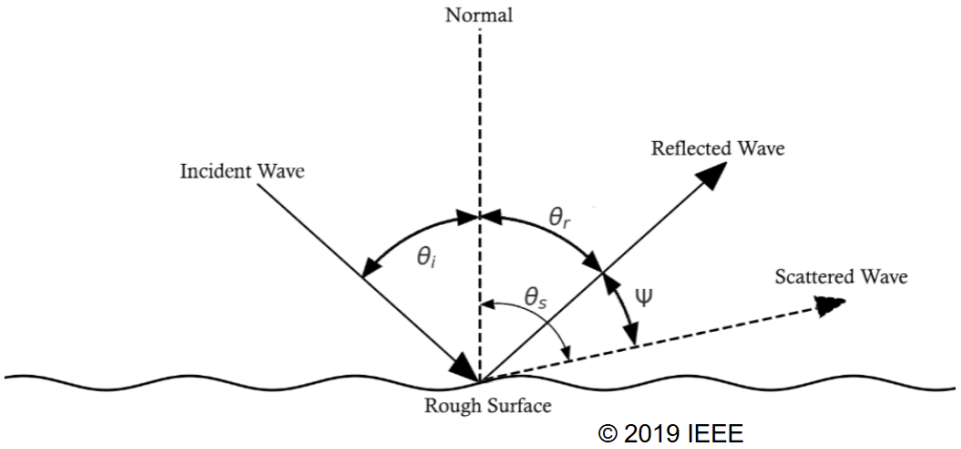

Figure 2.6: Diagram of wave reflection and scattering over a rough surface. Adapted from [4] Copyright 2019 IEEE. Used with permission.

Specular reflection with scattering loss occurs at high frequencies, where even seemingly smooth surfaces can introduce scattering loss, reducing the reflected power. The scattering loss factor, which accounts for the energy scattered away from the specular reflection, increases as frequency rises.

Material-dependent scattering varies with different materials having varying surface roughness and dielectric properties, leading to different scattering behaviors. Rougher surfaces tend to scatter more energy compared to smoother ones, which maintain higher reflection dominance.

The incident angle significantly impacts scattering behavior, with higher angles leading

to increased specular reflection, while lower angles introduce more diffuse scattering. At grazing angles, reflection dominates, whereas at normal incidence, scattering effects are more pronounced.

Effects of Multipath Propagation

Multipath propagation can severely impact high-frequency communication performance in several ways. One key issue is fading, which occurs due to phase differences between multiple signal components. Depending on the coherence time and delay spread, fading can be classified into flat fading, where the entire signal bandwidth is affected equally (often requiring power control or equalization), or frequency-selective fading, where different frequencies experience different attenuation. The latter can lead to inter-symbol interference (ISI) [20] and degrade data transmission.

Another significant effect is delay spread and inter-symbol interference (ISI), which arise when signals arrive at slightly different times due to multipath propagation. This causes overlapping symbols at the receiver, reducing data integrity, particularly problematic for high-data-rate applications.

Finally, Doppler shift becomes an issue when the transmitter, receiver, or reflectors are in motion. Frequency shifts due to the Doppler effect can impact synchronization and increase the complexity of channel estimation.

To address these challenges, while keeping a proper signal level, modern devices must adapt using advanced techniques such as beamforming, reconfigurable intelligent surfaces, and adaptive filtering. These methods help mitigate the effects of obstacles and ensure reliable communication in complex environments.

2.2 Definition of Reconfigurable Intelligent Surfaces (RIS)

In this section, we will explain the operating principles of RIS and discuss the fundamental concepts of electromagnetic and signal processing on which they are based.

α The constant phase offset applied between elements to steer the main beam in a desired direction.

ψ The total electrical angle seen by the array, combining spatial phase progression $kd\cos\theta$

Table 2.1: Definition of Symbols

Symbol	Description	Units
α	Progressive phase shift between array elements	rad
beginequation 3pt] ψ	Electrical scan angle ($kd\cos\theta + \alpha$)	rad
a_n	Amplitude coefficient of the n-th antenna element	–
k	Wave number ($2\pi/\lambda$)	rad/m
E	Radiated electric field (far-field)	V/m
N	Radiation intensity (power per unit solid angle)	W/sr

with the progressive shift α.

a_n The weighting factor that sets the excitation amplitude of each individual antenna element, shaping the overall array pattern.

k The spatial frequency of the wave, defined by the free-space wavelength λ, determines phase change per unit distance.

E The magnitude of the electric field radiated by the antenna in the far-field region, proportional to the element pattern and array factor.

N The radiated power per unit solid angle, representing how the antenna directs energy into space.

2.2.1 Antenna Arrays

As demonstrated in Section 2.1.1, the increasing trend toward higher frequencies has led to progressively smaller antennas. This transition makes directivity a critical parameter in modern communication systems. Since higher frequencies suffer from greater free-space path loss, it is essential to focus the transmitted and received energy in a desired direction.

To achieve enhanced directivity and effectively choose the angle of reception, antenna arrays play a fundamental role. By arranging multiple antennas in a structured configuration, we can steer and shape the radiation pattern dynamically, improving overall performance.

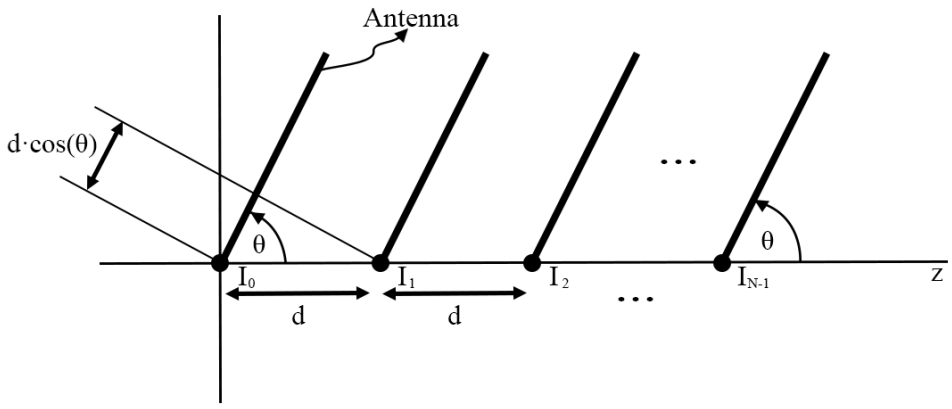

Figure 2.7: Linear Antenna Array

Figure adapted from [21]

A uniform linear array, as depicted in Figure 2.7, consists of N elements spaced at a distance d, each with a progressive phase shift α. The total radiated intensity can be expressed as:

$$\vec{N}(\vec{r}) = \vec{N_0}(\vec{r}) \cdot \sum_{n=0}^{N-1} I_n e^{jk_z nd} \tag{2.6}$$

where:

$$I_n = a_n e^{jn\alpha} \quad \text{with:} \quad \begin{cases} \alpha & \text{progressive phase shift} \\ a_n & \text{amplitude coefficient of each antenna} \end{cases} \tag{2.7}$$

The electric angle ψ represents the phase difference between consecutive elements in the far-field region:

$$\psi = k_z d + \alpha = kd\cos\theta + \alpha \tag{2.8}$$

The array factor $AF(\psi)$ is the constructive and destructive radiation product of several antennas. It is a crucial parameter that defines the overall beamforming effect of the antenna array:

$$AF(\psi) = \sum_{n=0}^{N-1} a_n e^{jn\psi} \tag{2.9}$$

Finally, the total radiated field incorporating the array factor is given by:

$$\vec{E}(\vec{r}) = \vec{E_0}(\vec{r}) \cdot FA(\psi) \tag{2.10}$$

Equations extracted from [21]

This formulation shows that beamforming is controlled by the array factor $FA(\psi)$, allowing us to steer and enhance directivity at desired angles. By tuning α and adjusting a_n, we can optimize the radiation pattern, enabling highly directive and efficient transmission and reception at high frequencies.

The visible margin defines the angular region where the main lobe and significant side lobes of the array factor are contained. This range extends from $\alpha - kd$ to $\alpha + kd$, as indicated by the dashed vertical lines in Figure 2.8. Mathematically, it is expressed as:

$$\alpha - kd \leq \psi \leq \alpha + kd \tag{2.11}$$

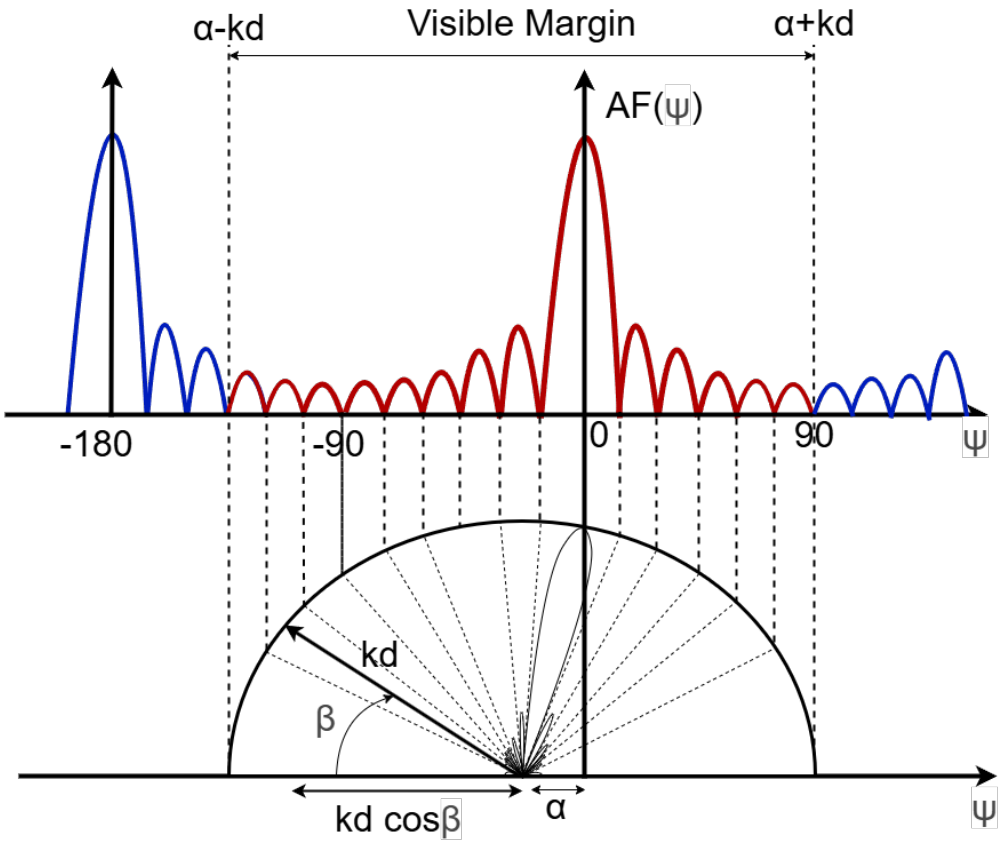

Figure 2.8: Visible margin and radiation pattern symmetry for an antenna array oriented along the z-axis. The visible margin extends from $\alpha - kd$ to $\alpha + kd$, defining the main beam and the significant side lobes of the array factor $AF(\psi)$. The lower plot illustrates the symmetrical radiation pattern in the XY plane, highlighting the influence of $kd\cos\beta$ on beamforming.

Figure adapted from [22]

This interval determines the effective beamforming region, where the array elements constructively interfere to form a strong directive pattern. Outside this margin, the radiated power diminishes, and the contributions from the array become negligible.

Additionally, if there is only one line of antennas, there will exist a revolution symmetry of the array factor, which means that the radiation pattern repeats in the XY plane.

Directivity and Antenna Arrays

The directivity D of an antenna array quantifies how concentrated the radiated energy is in a specific direction compared to an isotropic radiator. As seen in Figure 2.8, the visible margin defines the angular region where the main lobe and significant side lobes of the array factor $FA(\psi)$ are contained. Directivity is mathematically expressed as:

$$D = \frac{|FA_{\text{MAX}}|^2}{\frac{1}{2kd}\int_{\text{MV}} |FA(\psi)|^2 d\psi}$$

equation extracted from [21]

Where FA_{MAX} represents the maximum value of the array factor, which defines the peak radiation intensity. The denominator accounts for the total radiated power, integrated over the visible margin (MV), describing the energy distribution across the beamwidth. The term kd corresponds to the wavenumber multiplied by the inter-element spacing, which influences phase progression and beamforming accuracy.

Figure 2.8 illustrates how the array factor determines the beam shape, and directivity is directly related to the width of the main lobe. Increasing the number of antennas N leads to a narrower main beam, reducing side lobes and increasing overall directivity.

This result shows that for larger antenna arrays, the energy is more focused, improving angular resolution and signal reception.

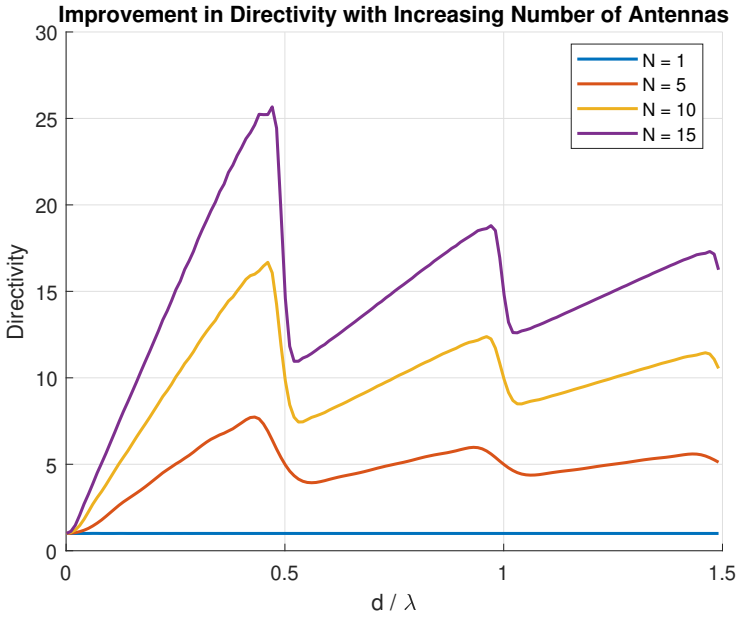

Figure 2.9: Example of directivity improvement with an increasing number of antennas in an array. A larger number of antennas results in a narrower main lobe, reducing side lobes and enhancing beamforming accuracy.

2.2.2 Definition of RIS

Reconfigurable Intelligent Surfaces (RIS) represent an innovative technology in wireless communications designed to intelligently manipulate the propagation of electromagnetic waves [23, 6]. Unlike conventional transmission and reception systems, RIS consists of a structured array of passive or semi-passive (also there are active [23]) elements that can dynamically adjust their reflection, refraction, or scattering properties [6, 24]. These elements are engineered using advanced electromagnetic materials and can be programmed to alter the phase, amplitude, and polarization of incident signals [25, 5].

RIS can be considered as a two-dimensional artificial structure composed of multiple unit cells, each capable of independent tuning [5]. This tunability allows RIS to control the wireless propagation environment by directing or reshaping signals to optimize communication performance. Unlike traditional arrays, which actively amplify and regenerate signals, RIS operates in a nearly-passive mode, significantly reducing energy consumption while enhancing signal coverage and capacity [5].

A key application of RIS is its ability to establish virtual Line-of-Sight (LoS) connections in non-Line-of-Sight (NLoS) scenarios. By intelligently reflecting incoming signals towards intended receivers, RIS can mitigate the impact of obstacles, such as buildings or natural terrain, that

typically degrade wireless connectivity [16]. This makes RIS particularly valuable for enhancing wireless communications in dense urban environments, factories, and underground settings.

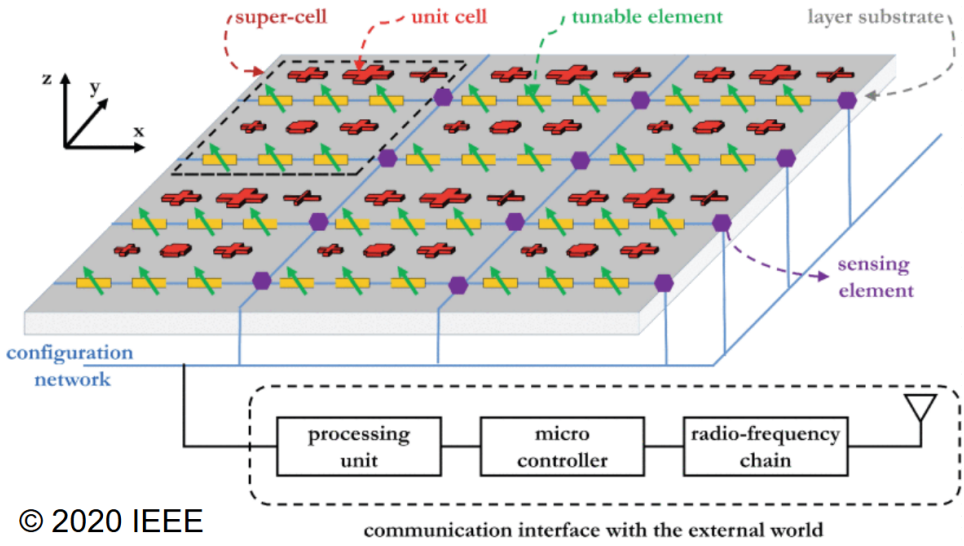

Figure 2.10: Structure of a Reconfigurable Intelligent Surface (RIS) with programmable elements [5]. Copyright 2020 IEEE. Used with permission.

RIS can function in different operational modes, including reflective and transmissive. In reflective mode, RIS behaves like an intelligent mirror, directing signals to enhance reception[5]. In transmissive mode, it acts as a lens, allowing signals to pass through and be redirected towards specific targets [5].

Additionally, recent developments in Active RIS have addressed limitations of passive RIS, where signals are simply redirected. Active RIS integrates amplification elements that can improve the signal-to-noise ratio (SNR) and overcome path loss issues, providing a significantly greater gain compared to passive RIS [23].

2.3 Technological Challenges and Applications

While RIS offers a transformative approach to wireless communication, several technological challenges must be addressed to enable its widespread deployment and maximize its potential benefits.

2.3.1 Technological Challenges

Multiplicative Fading and Path Loss Modeling

One of the inherent limitations of RIS technology is the multiplicative fading effect. Since an RIS-assisted communication link consists of two segments (transmitter-to-RIS and RIS-to-receiver), the overall path loss is significantly higher than in direct transmission scenarios. This issue is further exacerbated by the passive nature of RIS, which does not amplify signals but merely redirects them [26]. Recent studies have proposed refined path loss models that consider distance, surface size, and unit cell properties, leading to more accurate signal propagation estimates [26].

Channel Estimation Complexity

Unlike conventional wireless systems, where base stations and user equipment actively transmit and receive signals, RIS operates without active transmission components. This makes channel estimation significantly more challenging, as accurately estimating the interaction between the transmitter, RIS, and receiver requires sophisticated algorithms with minimal overhead [23].

Hardware Constraints and Control Mechanisms

The effectiveness of RIS depends critically on the performance of its tunable elements. Current implementations rely on electronic control mechanisms such as PIN diodes, varactors, and MEMS-based (Micro-Electro-Mechanical Systems) actuators, each presenting trade-offs in switching speed, power consumption, and phase resolution [6, 25]. Additionally, material-based control methods, including liquid crystals and graphene offer opportunities for continuous tuning but introduce challenges related to fabrication complexity and environmental stability [25].

2.3.2 Applications of RIS Technology

RIS-Enhanced Wireless Communications

RIS plays a crucial role in enhancing wireless networks by providing intelligent signal routing, particularly in environments with high signal attenuation. Experimental implementations of RIS-assisted communication systems have demonstrated significant improvements in spectral efficiency, power gain, and signal reliability [5, 27].

Wireless Power Transfer (WPT)

Beyond communication, RIS has been explored as a means to optimize wireless power transfer. By precisely adjusting the phase and direction of electromagnetic waves, RIS can focus energy onto specific targets, thereby improving power delivery efficiency for remote IoT devices and battery-free sensors [23].

Localization Applications

RIS technology is also being investigated for radar and sensing applications. By controlling the reflection properties of incident signals, RIS can enhance radar detection in NLoS scenarios, offering improved target localization and tracking. This capability is particularly relevant for security, autonomous navigation, and environmental monitoring systems [23]. Furthermore, RIS is also capable to enhance the positioning in LOS scenarios [28], producing additional measures of angle and time.

RIS-Integrated UAV Networks

The integration of RIS with unmanned aerial vehicles (UAVs) is a promising approach to improve wireless connectivity in remote and disaster-stricken areas. RIS-equipped UAVs can dynamically reconfigure wireless links to ensure stable and high-quality communication in challenging environments [23].

Brain-Controlled RIS

A groundbreaking application of RIS involves brain-computer interfaces, where RIS elements are controlled through neural signals. This concept, often referred to as electromagnetic brain-computer metasurfaces, has been experimentally validated, showcasing the possibility of human cognitive control over wireless propagation environments [23].

2.4 Existing RIS Providers

The development of Reconfigurable Intelligent Surfaces (RIS) has attracted significant attention from industry leaders, telecommunications companies, and research institutions [5, 27]. Several companies and organizations are actively involved in RIS research, prototyping, and commercialization. This section provides an overview of key industry players and their contributions to RIS technology.

2.4.1 Telecommunications Companies

ZTE Corporation

Zhongxing New Telecommunications Equipment has made substantial investments in RIS technology as part of its advancements toward 6G networks. The company has developed RIS-enabled solutions aimed at improving wireless coverage and spectral efficiency. Additionally, ZTE has actively participated in standardization efforts within organizations such as the *3rd Generation Partnership Project (3GPP)* and the *International Telecommunication Union (ITU)* [27].

SK Telecom

South Korea's SK Telecom is actively researching and developing RIS solutions for 6G networks. The company has demonstrated interest in integrating RIS into next-generation wireless networks, particularly in urban and high-density environments [27].

NTT DOCOMO

Nippon Telegraph and Telephone Corporation (NTT DOCOMO) has been a pioneer in the deployment and testing of RIS technology. It has partnered with companies like AGC Inc. and Metawave Corporation to develop transparent metasurfaces for enhanced wireless communication. The company has conducted real-world trials of RIS to assess its impact on signal propagation [27].

2.4.2 RIS Hardware Developers

AGC Inc.

AGC Inc., a Japanese materials and glass manufacturer, has played a crucial role in the development of transparent metasurfaces for RIS applications. The company collaborated with NTT DOCOMO to create RIS-enabled smart glass, allowing for improved indoor signal penetration [27].

Metawave Corporation

Metawave Corporation specializes in the development of intelligent metasurfaces for high-frequency communication. Their work includes designing RIS solutions for millimeter-wave

(mmWave) and sub-terahertz communication, enabling better signal reflection and coverage extension [27].

2.4.3 Standardization and Research Initiatives

To this day, there is not yet a RIS standard defined as a part of a 5G/6G system. However, there are a lot of initiatives in order to standardize the RIS technology. An example of them are:

6G-LICRIS Project

The 6G-LICRIS (Liquid Crystal Reconfigurable Intelligent Surfaces) project focuses on integrating RIS into mobile networks. The project is exploring liquid crystal-based RIS as a cost-effective and energy-efficient alternative to semiconductor-based solutions [27].

ETSI ISG RIS

The *ETSI Industry Specification Group for RIS* is working on defining RIS technology specifications and regulatory requirements. Companies like Rohde & Schwarz are actively contributing to ETSI's standardization efforts to ensure the seamless integration of RIS into future wireless communication networks [5].

2.4.4 Electromagnetic-Field Regulations Applicable to a RIS

Reconfigurable Intelligent Surfaces will be subject to the very same EMF constraints that already apply to 5 G base-stations. Any surface that coherently redirects down-link energy must respect the public-safety ceiling of $S_{\text{inc}} = 10W\,m^{-2}$ (above 2GHz) laid down by ICNIRP and mirrored by ITU-T, the FCC, the WHO, and most regional regulators [29]. Cui et al. [29] show that a RIS can approach—or even exceed—this limit when operated in two distinct modes:

- **Reflective-only (RO):** every unit cell behaves like a passive mirror; the local field barely rises above the background, so compliance is essentially guaranteed.
- **Beam-forming (BO):** phase-aligned cells create an N^2-type array gain that can push the peak field beyond the $10\text{W}\,m^{-2}$ cap unless mitigations are applied.

Their parametric study confirms that RO mode is intrinsically safe indoors, whereas BO mode remains compliant outdoors provided the panel is (i) mounted at least ~ 4 m above

ground, (ii) separated from the gNB by $\gtrsim$20 m, and (iii) subject to software caps on the fraction of simultaneously energised elements. In short, a RIS inherits the current 5 G EMF obligations, and sensible siting plus dynamic element-control are sufficient to keep it within those bounds.

Chapter 3

Theoretical Foundations of RIS

.

3.1 RIS Architecture

Reconfigurable Intelligent Surfaces (RISs) are engineered to dynamically manipulate electromagnetic (EM) wave propagation by integrating several functional layers [6]. This section provides an overview of the RIS architecture, emphasizing the key components and technologies that enable its reconfigurability and efficient operation.

3.1.1 Overview and Layered Structure

The RIS architecture is typically organized into three main layers, each fulfilling a distinct role in the overall system functionality.

Metasurface Layer: The core of an RIS is its metasurface, composed of a dense array of meta-atoms. Each meta-atom is designed to tailor the phase, amplitude, and polarization of an incident Electromagnetic wave [24]. This layer forms the fundamental mechanism by which the RIS controls wave propagation.

Control Unit: Operating in real time, the control unit processes channel state information and computes the biasing signals required to adjust each tunable element. Modern implementations frequently employ FPGA-based (Field Programmable Gate Array) platforms to achieve the low latency and high parallelism necessary for dynamic operation [6].

Communication Interface: This layer establishes connectivity between the RIS and the broader wireless network. It enables the exchange of configuration data and channel measurements, thereby facilitating the formation of virtual line-of-sight (LoS) paths and mitigating

interference [30].

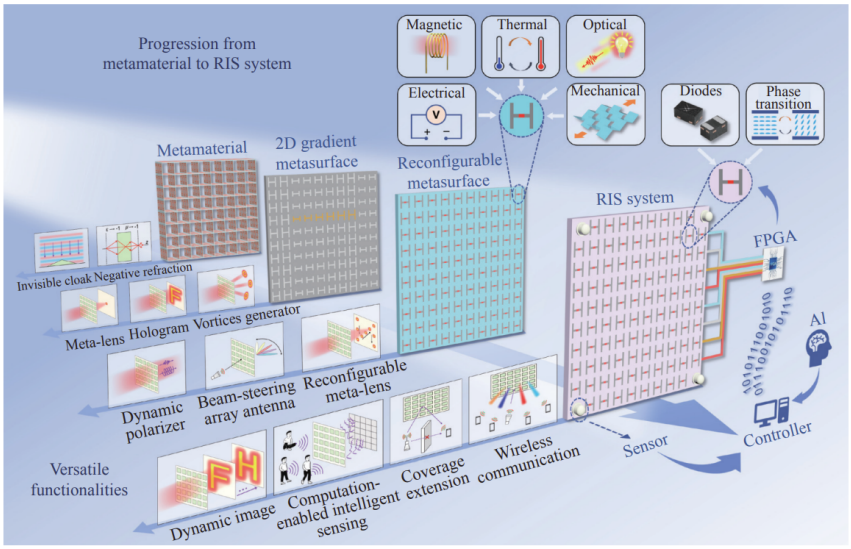

Figure 3.1: Block diagram of the evolution of the layered RIS architecture. From a metamaterial to a complex RIS architecture. Illustration reproduced from [6], CC BY 4.0.

3.1.2 Metasurface Layer and Tunable Elements

This subsection delves deeper into the metasurface layer, detailing the constituents of each meta-atom and their roles in wave manipulation.

Meta Elements: The basic scattering units of the metasurface are metallic patches or resonant structures. Their design is strictly governed by electromagnetic theory to ensure the continuity of tangential fields at material interfaces [25, 24].

Tunable Elements: Active components embedded within or adjacent to the meta elements dynamically adjust the local impedance of each meta-atom. This continuous control over phase and amplitude is achieved using devices such as varactors, MEMS switches, and, notably, PIN diodes[6].

Substrate Materials: Low-loss dielectric substrates provide mechanical stability and influence the effective permittivity and resonant behavior of the meta-atoms [24].

Figure 3.2 shows a schematic representation of a typical RIS meta-atom.

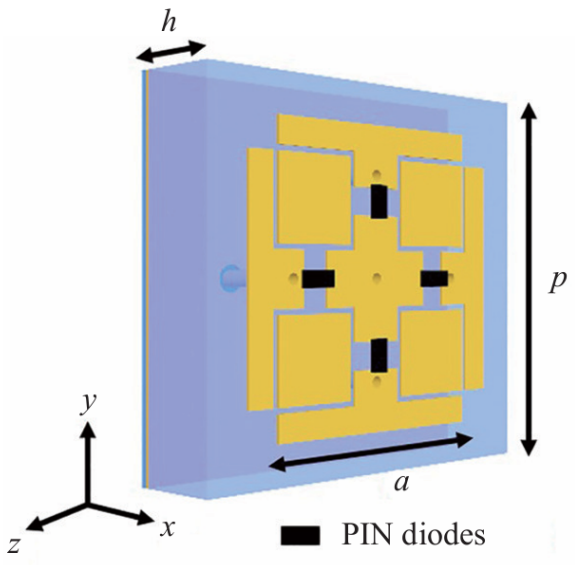

Figure 3.2: Schematic of a RIS meta-surface element with 2 polarizations. The structure features a metallic resonant patch printed on a dielectric substrate with integrated tunable elements for dynamic phase control. Illustration Illustration reproduced from [6], CC BY 4.0.

3.1.3 Diodes in RIS Architecture

Diodes play a critical role in enabling the reconfigurability of RIS meta-atoms.

PIN Diodes: PIN diodes are integral to achieving discrete phase control in RIS meta-atoms. By altering the effective impedance of the resonant elements, they allow for precise phase adjustments. For instance, a spiral unit cell may incorporate three PIN diodes, enabling the structure to switch among distinct phase states, where the phase shift is twice the rotation angle of the meta-atom [6].

Fast Switching: The intrinsic switching speed of PIN diodes, which can be on the order of tens of nanoseconds, permits rapid reconfiguration. This fast response is essential for real-time beam steering and adaptive signal control in RIS-assisted wireless communications [6].

Dual-Polarization Control: Independently controlling diodes in different orientations enables RISs to manipulate both left-hand and right-hand circular polarizations, thereby enhancing the device functionality [6].

Quantized Control: The discrete nature of diode switching supports quantized control schemes (e.g., 1-bit, 2-bit, or 3-bit phase modulation), which helps balance design complexity with per-

formance, particularly in large-scale arrays [6].

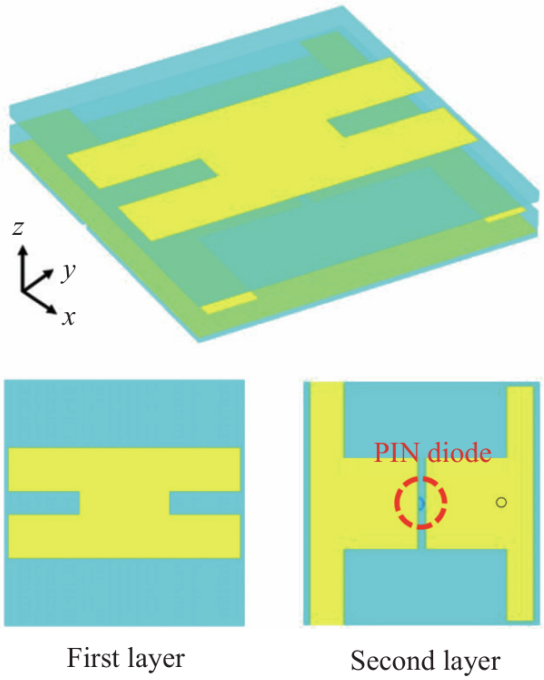

Figure 3.3: Schematic representation of a PIN diode. Illustration reproduced from [6], CC BY 4.0.

3.1.4 Control Unit

The final layer of the RIS architecture ensures effective integration with the broader wireless system.

Control Unit: This unit processes channel state information and computes the necessary biasing signals for each tunable element. FPGA-based systems are typically employed to achieve the required low latency and parallel processing capabilities [6].

Chapter 4

5G Positioning Model and PRS

Essential OFDM Grid Terms

Abbrev.	**Meaning**	**Key Facts**
SCS	Sub-carrier Spacing	$SCS = 15\ \text{kHz} \times 2^{\mu}$ (higher $\mu \rightarrow$ wider spacing).
SF	Sub-frame	5G NR: contains 2^{μ} slots.
Slot	—	Duration $= \frac{1\,\text{ms}}{2^{\mu}}$. It is the smallest time unit the gNB schedules.
PRB	Physical Resource Block	12 sub-carriers $\times$ SCS.
ToA	Time of Arrival	Propagation delay from transmitter to receiver; used for ranging.
AoA	Angle of Arrival	Incident angle of the received wavefront; basis for UE positioning.
AoD	Angle of Departure	Emission angle at the transmitter (e.g., gNB or RIS) toward the UE.
Fs	Sampling Frequency	Number of samples acquired per second.

4.1 5G NR Frame Structure

5G NR is the official air interface for 5G networks, as defined in 3GPP Release 15 (TS 38.300)[31]. It's frame structure is a core element of modern cellular networks, enabling flexibility in resource allocation and system performance. This section offers a comprehensive overview of the NR frame.

4.1.1 Overview

The NR frame is defined to span 10 ms and is subdivided into 10 sub-frames of 1 ms each. This hierarchical time structure supports dynamic scheduling and adapts to a wide range of deployment scenarios. Figure 4.1 illustrates the overall organization of the 5G NR frame.

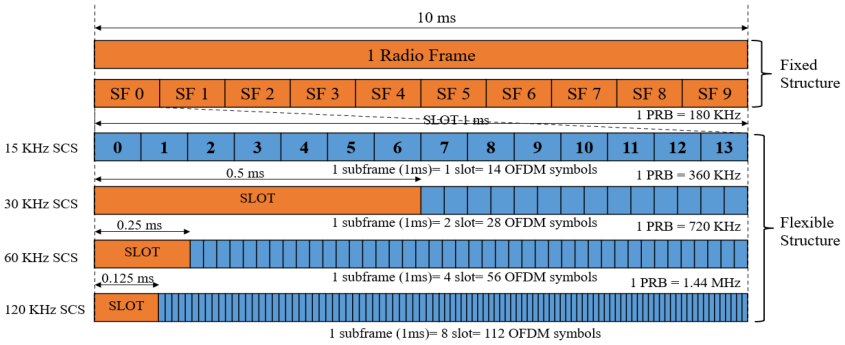

Figure 4.1: Overview of the 5G NR frame structure, detailing the division into frames, subframes, and slots. Figure reproduced from [7], CC BY 4.0.

4.1.2 Numerologies and Subcarrier Spacing

A key feature of 5G NR is its flexible numerology, which is defined by the subcarrier spacing (SCS). This parameter is given by

$$SCS = 15 \times 2^{\mu}\,\text{kHz},$$

where μ represents the numerology index. By adjusting μ, the system can vary the symbol duration and the slot configuration to optimize performance for different applications, ranging from enhanced mobile broadband to ultra-reliable low-latency communications. A detailed diagram of the numerology options and resource allocation is provided in Figure 4.1.

Table 4.1: TS 38.211 - v17.2.0 Table 4.3.2-1. Detailed representation of 5G NR numerologies and resource allocation, highlighting variations in subcarrier spacing and slot duration. Table extracted from [11].

μ	$N^{\text{slot}}_{\text{symb}}$	$N^{\text{frame},\mu}_{\text{slot}}$	$N^{\text{sub-frame},\mu}_{\text{slot}}$
0	14	10	1
1	14	20	2
2	14	40	4
3	14	80	8
4	14	160	16
5	14	320	32
6	14	640	64

4.1.3 Time-Frequency Grid and Frame Configuration

The time-frequency grid in 5G NR is engineered to maximize spectral efficiency. Each 10 ms frame is divided into sub-frames and further partitioned into slots. The slot duration is inversely related to the subcarrier spacing; for instance, when $\mu = 0$, a slot typically lasts 1 ms, whereas higher numerologies produce shorter slot durations. This granular configuration allows for precise resource scheduling and efficient handling of diverse traffic types [11].

4.1.4 Resource Blocks and Resource Elements

At the fundamental level of the NR frame, resources are allocated in the form of Resource Blocks (RBs). Each RB consists of 12 subcarriers over the duration of one slot. These blocks are further segmented into Resource Elements (REs), which are the smallest units for modulation and coding. This structure supports advanced techniques such as adaptive modulation and beamforming, ensuring robust performance even under challenging channel conditions [11].

4.2 Positioning Reference Signals (PRS)

4.2.1 Definition and Purpose

Positioning Reference Signals (PRS) are specialized signals introduced in the 5G New Radio (NR) standard to enable high-accuracy positioning capabilities in diverse wireless scenarios. Their design aims to facilitate precise time-of-arrival (ToA) and angle-of-arrival (AoA) measurements, as well as accurate assessment of received signal strength, even under complex multipath or non-line-of-sight conditions. By embedding PRS periodically within the NR frame, user equipment (UE) can acquire reliable measurements that inform localization algorithms and ultimately improve the accuracy of position estimates [11].

4.2.2 Transmission in the NR Frame

In practice, PRS are transmitted within designated *PRS occasions* that can recur periodically across the 5G NR frame. The specific time-frequency resources allocated to PRS vary according to network deployment requirements and service-level agreements. For instance, certain sub-frames or slots might be reserved for broadcasting PRS, ensuring minimal interference from data transmissions and improving the signal-to-noise ratio (SNR) for positioning measurements.

When integrated into the NR time-frequency grid, the placement of PRS can also consider:

Muting patterns: Networks can schedule PRS transmissions in a way that reduces overlap among neighboring gNBs, mitigating inter-cell interference.
Flexible periodicity: Operators can adapt the interval between PRS occasions based on UE mobility, increasing the frequency of positioning updates in rapidly changing environments.
Numerology dependencies: The subcarrier spacing and symbol duration, determined by the chosen numerology, can influence the density and precision of PRS transmissions.

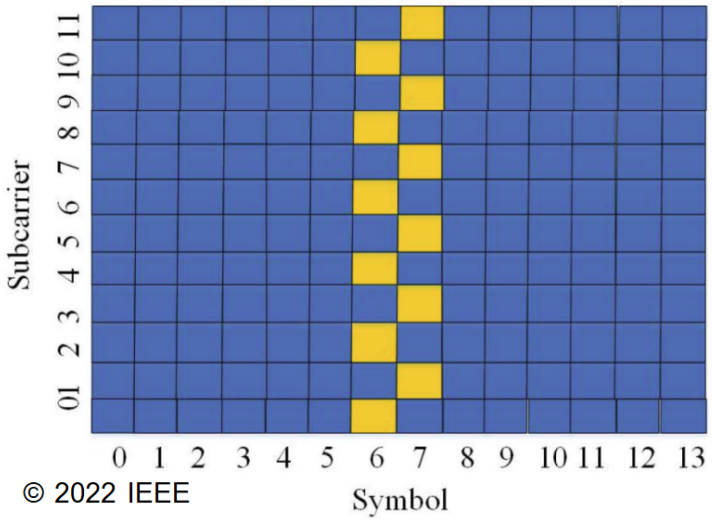

Figure 4.2: Conceptual mapping of PRS within a 5G NR frame, illustrating how PRS resources can be allocated to specific symbols and subcarriers. Figure reproduced from [8]. Copyright 2022 IEEE. Used with permission

4.2.3 PRS-Based Measurements

Once the UE detects PRS signals, it undertakes several critical measurements:

Time of Arrival (ToA): By measuring the exact arrival time of PRS relative to a known reference, the UE can estimate its distance to the transmitting gNB. This distance measurement forms the basis for various multilateration techniques.

Angle of Arrival (AoA): When the UE (or gNB) employs antenna arrays, PRS can enable accurate directional measurement of the signal. This directional information adds geometric diversity to positioning algorithms.

4.3 Integration of RIS in PRS-Based Positioning

Reconfigurable intelligent surfaces (RISs) have emerged as a key technology for enhancing positioning accuracy in next-generation wireless networks. By dynamically reconfiguring their reflection properties, RISs enable the manipulation of the radio propagation environment to overcome common challenges in localization such as non-line-of-sight (NLoS) conditions, multipath interference, and limited coverage.

4.3.1 Motivation for RIS-Enabled Positioning

Integrating RISs with positioning reference signals (PRS) is motivated by several critical factors:
Mitigation of NLoS and Multipath Effects: In urban or indoor environments, direct line-of-sight (LoS) conditions are often obstructed, and multipath propagation can lead to significant localization errors. RISs can reflect and steer incident PRS signals into shadowed regions, effectively mitigating these issues.
Extended Coverage in Obstructed Areas: In scenarios where conventional access points (APs) fail to provide sufficient coverage (e.g., tunnels or dense urban areas), RISs can extend the coverage area by redirecting signals towards users, thereby enabling reliable positioning.
Enhanced ToA and AoA Estimations: By providing additional controllable reflection paths, RISs enrich the geometric diversity of the received signal set. If the RIS is pre-loaded with phase shifts, the elevation and azimuth AoD can be estimated.

4.3.2 RIS Configuration for PRS

To exploit the benefits of RISs for PRS-based positioning, proper configuration and calibration are essential:

Dynamic Phase-Shift Programming: Each RIS element is equipped with a tunable phase shifter, which allows the surface to steer the incident wave in a desired direction. The received signal at the RIS can be modeled as

$$y_{\mathrm{RIS}}(n,\phi,\theta) = \left(d(\tau_{\mathrm{gNB-R}}) + d(\tau_{\mathrm{R-UE}}) + y_{gNB}(n)\right) G_{R-UE}(\phi,\theta) n_{RIS} + w(n), \tag{4.1}$$

where n_{RIS} is the power splitting ratio, $G_{\mathrm{R-UE}}$ is the matrix gain between the RIS and the UE with the components of each azimuth and elevation angle gains, further explained in 5.3.1, $d(\tau_{\mathrm{BR}})$ and $d(\tau_{\mathrm{R-UE}})$denotes the distance from the sampled delay from the RIS path.
Channel Estimation and Calibration: Since RISs are passive devices that reflect PRS signals, they do not generate their own signals. Advanced RIS architectures incorporate sensing

capabilities by splitting the received power so that a portion is used for channel estimation. This dual functionality can be crucial for calibrating both the RIS state (position and orientation) and the UE [28]. However, for simplicity, in our simulation there will be no estimation from the RIS part, as it will be fully-passive.

The code implemented in order to configure the received signal from the RIS in MATLAB is:

```
    % ADD RIS DELAY AND PATH LOSS
% 1) Distances gNB-to-RIS and RIS-to-UE
d_g2r     = norm(gNBPos{idxMin} - ris.Pos);  % m
d_r2u     = norm(ris.Pos     - UEPos);      % m

% 2) Delay in samples
delay_g2r = round((d_g2r/c) * ofdmInfo.SampleRate);
delay_r2u = round((d_r2u/c) * ofdmInfo.SampleRate);
totalDelay= delay_g2r + delay_r2u ;

% 3) Path-loss constants
PLlin_g2r = 10^( nrPathLoss(plCfg,fc,true, gNBPos{idxMin}(:), ris.Pos(:)) / 10 )
    ;
PLlin_r2u = 10^( nrPathLoss(plCfg,fc,true, ris.Pos(:),      UEPos(:)) / 10 );

% Use the gNB{1} tx signal
txRef    = txWaveform{idxMin};      % nSamples 1
nSamp    = numel(txRef);
numGphi     = numel(gain(:,1));
numGth = numel(gain(1,:));
outLen   = totalDelay + nSamp;

% Pre-aloccate: outLen numGphixnumGth
rxRIS = zeros(outLen,numGphi, numGth);

% For each RIS coefficient:
for k = 1:numGphi
    for l = 1:numGth
    % a) Attenuation  g N B RIS
    RISsignal = txRef / sqrt(PLlin_g2r);

    % b) Aplicar ganancia del RIS (vector     gain    )
    RISsignal = RISsignal * gain(k,l)*ris.A;

    % c) Attenuation  R I S UE
    RISsignal = RISsignal / sqrt(PLlin_r2u);
    RISsignal_nodelay(:,k,l) = RISsignal; %To later calculate SNR
    % d) Padding for the total geometric delay
    rxRIS(:,k,l) = [ zeros(totalDelay,1);    % ceros first
                     RISsignal ];                  % processed signal
    end
```

```
end

% Match the samples in RIS and gNB
lenGNB = size(rxWaveform,1);
lenRIS = size(rxRIS(:,1),    1);
diflen = abs(lenRIS - lenGNB);
% If RISrx is larger, we padd
if lenRIS > lenGNB
    rxWaveform_padded = [ rxWaveform;
                          zeros(diflen, 1) ];
else
   rxWaveform_padded = rxWaveform;
   rxRIS(end+1:end+diflen, :, :) = 0;
end
```

First, we convert each propagation distance into a discrete sample delay by dividing by the speed of light and then scaling by the system sampling frequency. In mathematical terms, the delay in samples for the total path is

$$N_{g\text{-}r} = \text{round}\Big(\frac{D_{g\text{-}r}}{c} \times F_s\Big), \tag{4.2}$$

$$N_{r\text{-}u} = \text{round}\Big(\frac{D_{r\text{-}u}}{c} \times F_s\Big), \tag{4.3}$$

which tells us approximately (because of the round) how many time steps the wave spends in flight.

Afterwards, the reflected RIS waveform is generated by applying the gain coefficients per angle to the original signal, effectively sculpting the beam in the desired direction. Afterwards, the Path loss is applied, considering an Urban Macro scenario. Finally, we align direct and reflected RIS signals in the discrete-time domain, shifting each by its computed sample delay, so that they can be coherently summed and processed together in the correlation and positioning stages.

4.3.3 Benefits and Expected Performance Gains

The deployment of RISs in PRS-based positioning systems is expected to bring several benefits:

Improved Localization Accuracy: RISs can be configured to selectively enhance the desired signal components while suppressing interfering multipath components, thus improving the reliability and precision of ToA and AoD estimates.

Energy-Efficient and Cost-Effective Positioning: As RISs operate largely in a passive mode, with only minimal active circuitry required for control and sensing they offer an energy-efficient solution. This makes them particularly attractive for dense urban deployments where energy consumption and deployment costs are critical factors.

Chapter 5

Practical Implementation and Experiments

In this chapter, it is presented the development and evaluation of a fully operational Reconfigurable Intelligent Surface (RIS) within a simulation environment. The objective is to replicate the physical behavior of a real-world RIS as closely as possible, incorporating element efficiency, array geometry, and beam-steering characteristics, while capitalizing on the flexibility and cost savings that this RIS could afford in comparison to a Base Station.

5.1 System Design and Setup

5.1.1 Hardware Components

In this work, a purely simulation-based model of a fully passive array-based Reconfigurable Intelligent Surface (RIS) is adopted . The RIS is represented as a planar array of scattering elements whose phase responses are fixed (preloaded) for every azimuth and elevation steering angle, and each element has an efficiency of 80%. By using precomputed phase-shift values, we avoid the need for real-time control hardware, thereby simplifying the system, reducing its expense, and focusing the study on propagation behavior.

The simulated RIS is visualized as a two-dimensional array of antenna elements distributed along the Y and Z axes. In our coordinate system, the RIS lies in the YZ plane (normal to the $-X$ axis), with N_Y elements along the vertical (Z) direction and N_Z elements along the horizontal (Y) direction. Each element is modeled as an isotropic radiator with unit amplitude and a phase offset determined by the target steering directions. By representing the RIS in this

way, we can readily compute array factors, beam patterns, and far-field scattering characteristics using standard antenna-array theory.

5.1.2 Software and Simulation Tools

Simulations will be executed in MATLAB R2024b on a workstation configured with the following specifications:

- **CPU**: 11th Gen Intel® Core™ i7-1165G7 @ 2.80 GHz (4 cores, 8 threads)
- **Memory**: 32 GB DDR4
- **GPU**: Intel® Iris Xe Graphics (integrated)
- **Storage**: 466 GB NVMe SSD (CT500P3SSD8)
- **Operating System**: Windows 11 Home (64-bit)

The MATLAB environment is extended with Communications Toolbox, 5G Toolbox, 6G exploration library for 5G enviroments The one-dimensional array factor routine `array1d` from [21] was extended to a two-dimensional implementation, `array2d`. This new function computes the full array factor over both azimuth and elevation angles and returns the corresponding gain coefficient for the corresponding direction. The simulation framework combines two specialized toolboxes:

The "NR Positioning Using PRS" example (version from 02/04/2025), which provides routines for 5G NR Positioning Reference Signal generation, channel modeling and positioning algorithms. Its waveform-generation and channel-estimation functions have been interfaced with a passive RIS model [9].
The "Model Reconfigurable Intelligent Surfaces with CDL Channels" example, offering risArray and risChannel modules for element-wise array geometry, CDL-based propagation models and beam-steering utilities. Was useful to compare gain coefficients, and were used some of the channel properties [32].

5.2 Implementation Details

5.2.1 Configuration Parameters

The key parameters defining the simulation scenario are summarized in Table 5.1.

Carrier and OFDM	
Carrier frequency	$f_c = 3$ GHz
Wavelength	$\lambda = c/f_c \approx 0.10$ m
Subcarrier spacing	$\Delta f = 15$ kHz
FFT size	$N_{\text{fft}} = 1024$
Sampling rate	$F_s = 15$ MHz
RIS Geometry and Reflection	
RIS dimensions	$N_Y \times N_Z \times N_{\text{pol}} = 50 \times 50 \times 1$
Element spacing	$d_y = d_z = \lambda/2 \approx 0.05$ m
Total elements	$50 \times 50 \times 1 = 2{,}500$
Reflection amplitude	$A = 0.8$ (80 %)
PRS Configuration	
Number of gNBs	5
PRS periodicity	$T_{\text{PRS}} = 10$ slots
PRS slot offsets	$\{0, 2, 4, 6, 8\}$
Resource blocks	$N_{\text{RB}} = 52$
PRS symbols	12 per transmission
Path-loss model	ITU Urban macro (UMa), LOS only
Additive noise SNR	10 dB at 5km radius

Table 5.1: Summary of configuration parameters for the joint PRS-OTDOA-RIS simulation.

Carrier, OFDM and PRS configuration parameters are used directly from the NR positioning example, ensuring consistency with standardized 5G NR signal structures and avoiding any manual re-parameterization. In contrast, the RIS geometry and reflection settings were chosen to evaluate end-to-end link performance: a 50×50 element array provides sufficient aperture gain to mitigate some of the additional path loss introduced by the cascaded gNB-RIS-UE propagation, while a half-wavelength inter-element spacing ($d = \lambda/2$) guarantees beam coverage over the full 180° front-facing hemisphere of the surface. This design balances array size, element efficiency, and angular scanning range to evaluate effective received power at the UE. Moreover, the SNR parameter is designed to be 10 dB at the radius of the coverage of the gNBs (5 km)

5.3 Complete Code Implementation

The entire MATLAB implementation employed in this work is publicly available at

github.com/RIS-Positioning-with-5G-NR-using-PRS

The important script parts are still listed and explained.

5.3.1 Control Algorithms

Symbol	Parameter	Description
ϕ	Azimuth AoD	Horizontal angle of departure measured from a reference direction
θ	Elevation AoD	Vertical angle of departure measured above the horizontal plane
$\alpha_\phi, \alpha_\theta$	Phase shifts	Relative phase offsets applied to the transmitted signal element
Ψ	Electrical angle	Angle of the electric field vector relative to a reference axis

Table 5.2: Definitions of angular parameters and phase shift

Gain-Matrix Associated with Azimuth Values

The gain matrix **G** is a look-up table that relates each steered azimuth angle to the array-factor gain observed in that direction. It is later employed to estimate the user's angle of departure (AoD). The construction procedure is explained below for the beam azimuth sweep at $\phi = \{270°, 265°, ..., 90°\}$.

Steering angles and progressive phase shift: For a uniform linear RIS with element spacing $d = \lambda/2$ ($kd = \pi$), the progressive phase shift that steers the main lobe towards ϕ_i, which arrives within 270^{o} and 90^{o}, so that in order to transform this azimutal angle into cartessian. The formulation is

$$\alpha_\phi + kd = \pi\big(1 + \cos(\phi_i - 90°)\big) \tag{5.1}$$

$$\boxed{\alpha_\phi = -\sin\phi_i} \tag{5.2}$$

where α_ϕ denotes the electrical angle of the main-beam peak in ϕ_i.

Array-factor evaluation: With the steering vector fixed to $\Delta\Psi_i$, the azimuth array factor is

$$\boxed{\mathrm{AF}_{\phi_i}(\Psi) = \sum_{n=1}^{N_\Psi - 1} e^{j\,n\left(\Psi - \alpha_{\phi i}\right)}.} \tag{5.3}$$

Directivity calculation: for a comparison between beams, the directivity at the real angle lobe peak is computed as

$$\boxed{D(\phi_{estimated}) = \frac{2kd_y \left|\mathrm{AF}_{\phi_i}(\Psi_{\mathrm{real}})\right|^2}{\Delta\Psi \sum_{VM} \left|\mathrm{AF}_{\phi_i}(\Psi)\right|^2}}, \tag{5.4}$$

Assuming that the RIS element efficiency includes the gain efficiency, we will have the estimated gain for each angle:

$$\mathbf{G}_{\phi\mathbf{i}} = \left[\, D(270^\circ),\ D(265^\circ), \ldots, D(90^\circ)\right] n_{RIS}. \tag{5.5}$$

where d_y is the element spacing in the y-direction, $\Delta\Psi$ is the electrical-angle sampling step, and $\mathrm{AF}_{\phi_\mathrm{i}}$ denotes the azimuth array factor. The on-axis gain is obtained at $\Psi = \Psi_{\max} = \alpha_{\phi i}$. Repeating the calculation for every ϕ_i produces the azimuth gain vector, which will have $\frac{270-90}{N_\phi}$ steps.

Association with the real AoD

Because the user's true AoD, ϕ_{real}, is known in simulation. In this scenario, the $\phi_{real} = 180^\circ$(which in cartesian will ecuate to $\phi_{real,cartesian} = 90^\circ$) its electrical counterpart $\Psi_{\mathrm{real}} = -kd\sin\phi_{\mathrm{real}}$ is calculated and the corresponding gain G_{real} (or D_{real}) is read directly from $\mathbf{G}$. During on-line operation, the beam that maximises $\mathbf{G}$ (or $\mathbf{D}$) provides the AoD estimate.

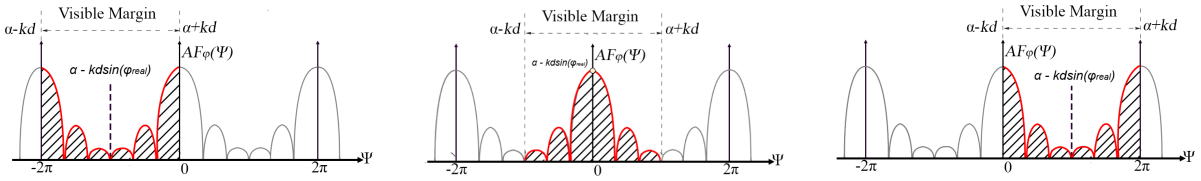

(a) $\phi = 270^\circ \Rightarrow \alpha_\phi = -\pi$ (b) $\phi = 180^\circ \Rightarrow \alpha_\phi = 0$ (c) $\phi = 90^\circ \Rightarrow \alpha_\phi = \pi$

Figure 5.1: Array-factor peak (hatched area) for the three steering directions used to populate the gain matrix. As ϕ moves from 270° to 90°, the main lobe, and therefore the visible margin, slides from left to right along the Ψ-axis.

Because each RIS element is assumed isotropic, the array factor equals the radiation pattern; hence the peak of $\mathbf{G}$ directly identifies the AoD. In the example sweep, a marker located at $\Psi = 0$ (Fig. 5.1b) implies an estimated AoD of 180°.

This example, extrapolated to an $N_y \times N_z$ RIS that steers both in azimuth and elevation, illustrates how the two-dimensional *gain matrix* is assembled. Let the azimuth sweep be $\boldsymbol{\phi} = [\,270^\circ,\ 175^\circ, \ldots,\ 90^\circ\,]$ ($N_\phi = 19$) and the elevation sweep $\boldsymbol{\theta} = [\,-30^\circ,\ -19.47^\circ, \ldots,\ -1.85^\circ\,]$ ($N_\theta = 30$) which in cartesian (From 90° to 0°) we have to add 90°, like the azimuth case . For every azimuth-elevation pair (ϕ_i, θ_j) the main lobe is steered by applying the progressive phase shifts, and the

$$\alpha_{\phi i} = -kd\sin\phi_i, \qquad \alpha_{\theta j} = -kd\sin\theta_j, \tag{5.6}$$

along the y- and z-axes, respectively. The on-axis azimuth directivity

$$D_{\mathrm{az}}(\phi_i) = \frac{2kd_y \left|AF_{\mathrm{az}}(\Psi_{real})\right|^2}{\Delta\Psi \sum_{MV} \left|AF_{\phi}(\Psi)\right|^2}, \quad \Psi_{real} = -kd\sin\phi_{real}, \tag{5.7}$$

and the elevation directivity

$$D_{\mathrm{el}}(\theta_j) = \frac{2k\,d_z \left|AF_{\mathrm{el}}(\Phi_{real})\right|^2}{\Delta\Phi \sum_{\Phi} \left|AF_{\mathrm{el}}(\Phi)\right|^2}, \quad \Phi_{real} = -kd\sin\theta_{real}, \tag{5.8}$$

are evaluated independently. The composite gain for that steering direction is obtained by multiplying the two contributions:

$$\boxed{G_{ij} = D_{\mathrm{az}}(\phi_i)\; D_{\mathrm{el}}(\theta_j) n_{RIS}}. \tag{5.9}$$

Collecting all products produces the two-dimensional *gain matrix*

$$\mathbf{G} = \begin{bmatrix} D_{\mathrm{az}}(270^\circ)\, D_{\mathrm{el}}(-30^\circ) & D_{\mathrm{az}}(270^\circ)\, D_{\mathrm{el}}(-19.47^\circ) & \cdots & D_{\mathrm{az}}(270^\circ)\, D_{\mathrm{el}}(-1.85^\circ) \\ D_{\mathrm{az}}(265^\circ)\, D_{\mathrm{el}}(-30^\circ) & D_{\mathrm{az}}(265^\circ)\, D_{\mathrm{el}}(-19.47^\circ) & \cdots & D_{\mathrm{az}}(265^\circ)\, D_{\mathrm{el}}(-1.85^\circ) \\ \vdots & \vdots & \ddots & \vdots \\ D_{\mathrm{az}}(90^\circ)\, D_{\mathrm{el}}(-30^\circ) & D_{\mathrm{az}}(90^\circ)\, D_{\mathrm{el}}(-19.47^\circ) & \cdots & D_{\mathrm{az}}(90^\circ)\, D_{\mathrm{el}}(-1.85^\circ) \end{bmatrix} n_{\mathrm{RIS}} \tag{5.10}$$

The entry with the highest value in $\mathbf{G}$ provides the azimuth AoD estimate. The MATLAB function created to form the gain-matrix was *calculateRISCoeff*:

```
function [thList, phiList, gain] = calculateRISgainCoeff(enableRIS, risCh, ueAz
    , ueTh, ris)
% calculateRISgainCoeff   RIS coefficients with controlled beamwidth via
    tapering and iterative pattern plotting
%   enableRIS: flag to enable RIS optimization
%   risCh    : hpre6GRISChannel object
%   ueAz     : known UE azimuth (rad)

% 1) Constants & RIS geometry
c      = physconst("lightspeed");
lambda = c/risCh.CarrierFrequency;

risSize = risCh.RISSize;  % [M N P]
M = risSize(1);
N = risSize(2);

dz = ris.dx/lambda;
```

```
dy = ris.dy/lambda;


anY = ones(1,M);
anZ = ones(1,N);

phiList = deg2rad(180):-deg2rad(5):deg2rad(90);



thList = [
  -0.523598775598303, -0.339836909454126, -0.252680255142078,
    -0.201357920790330, ...
  -0.167448079219690, -0.143347568905365, -0.125327831168065,
    -0.111341014340964, ...
  -0.100167421161560, -0.0910347780374153, -0.0834300866106150,
    -0.0769991406568236, ...
  -0.0714894498855205, -0.0667161484102252, -0.0625407617964915,
    -0.0588575059470812, ...
  -0.0555841732809176, -0.0526559082615699, -0.0500208568057700,
    -0.0476370626244031, ...
  -0.0454702124169971, -0.0434919707901158, -0.0416787324225779,
    -0.0400106743539889, ...
  -0.0384710274073283, -0.0370455098120920, -0.0357218823980788,
    -0.0344895959616788, ...
  -0.0333395092613021, -0.0322636616682469
];

alphaListY = -2*pi * dy * sin(phiList);
alphaListZ = -2*pi * dz * sin(thList);
K    = numel(phiList);
L    = numel(thList);

if ~enableRIS
    % RIS turned OFF
    gain = zeros(K,L);
    return;
end


for k = 1:K

    for n = 1:L
       % We extract the gain from the specific phiList(k) and thList(n)
    [gainFA,~,~,~]=array2d(anY,anZ,alphaListY(k),alphaListZ(n),dy,dz,ueAz,ueTh,
    phiList,thList);

```

```
55      gain(k,n)       = gainFA;
56      end
57  end
58  end
```

The routine `calculateRISCoeff` generates the full two-dimensional gain map $G(\phi_k, \theta_n)$ for the RIS scan grid in a single pass. First, the carrier wavelength $\lambda = c/f_c$ is obtained from `risCh`, and the physical element spacings d_y, d_z are normalised to d_y/λ and d_z/λ for an $M \times N$ square aperture. A coarse azimuth sweep $\phi_k \in [180°, 90°]$ with 5 degree spacing and a 30-point log-spaced elevation sweep $\theta_n \in [-30°, -1.8°]$ is used for the longitudinal step; The commented code in Section 6.4.3 can collapse this matrix to a three-point micro-scan around the UE to cut runtime.

For every (ϕ_k, θ_n) pair the elemental phase shifts $\alpha_y = -2\pi(d_y/\lambda)\sin\phi_k$ and $\alpha_z = -2\pi(d_z/\lambda)\sin\theta_n$ are pre-computed and passed to the function `array2d` (adapted from [21]). Two nested loops fill the $K \times L = 19 \times 30$ matrix with the resulting array factors. If `enableRIS`=0 the routine simply returns a zero matrix.

```
1      function [gain,FAaz,FAth,Daz]=array2d(anY,anZ,alfaY,alfaZ,dy,dz,angAz,angEl,
       phi,th)
2
3   % Modified function from Josep Parron, I added one dimension extra
4
5   %Verificando las entradas
6   [M,N]=size(anY);
7   if (M~=1) | (N<1), error('an debe ser un vector fila'); end;
8   aux=size(alfaY);
9   if (aux~=1), error('alfa tener dimensiones 1x1');end;
10  aux=size(dy);
11  if (aux~=1), error('d tener dimensiones 1x1');end;
12  if (dy<0), error('d tiene que ser mayor que cero');end;
13  aux=size(sw);
14  if (aux~=1), error('sw tener dimensiones 1x1');end;
15
16  %Angulo electrico
17  dpsi = pi/1000;
18  lenY = 2*pi*(1+2*dy);
19  lenZ = 2*pi*(1+2*dz);
20  n_ptosY = lenY/dpsi;
21  n_ptosZ = lenZ/dpsi;
22  psi_phi=linspace(-pi-2*pi*dy+alfaY,+pi+2*pi*dy+alfaY,n_ptosY);
23  psi_th = linspace(-pi-2*pi*dy+alfaZ,+pi+2*pi*dy+alfaZ,n_ptosZ);
24  %Diagrama de radiacion en el espacio electrico
25  FA_az=abs(freqz(anY,1,psi_phi));
26  FA_el=abs(freqz(anY,1,psi_th));
27  %Angulo real
```

```
28
29 phiList = linspace(phi(1), phi(end), 2*360 + 1);
30 thList = linspace(th(1), th(end), 2*360 + 1);
31 angfa= linspace(pi,0, 2*360+1);
32 %psi=k*d*cos(th)+alfa
33 psi_re_az=2*pi*dy*cos(angfa)+alfaY;
34 psi_re_th=2*pi*dz*cos(angfa)+alfaZ;
35 %Diagrama de radiacion en el espacio real
36 FAaz=abs(freqz(anY,1,psi_re_az));
37 FAth=abs(freqz(anZ,1,psi_re_th));
38 %Calculo directividad
39 raz=find((psi_phi > min(psi_re_az)) & (psi_phi < max(psi_re_az)));
40 rel=find((psi_th > min(psi_re_th)) & (psi_th < max(psi_re_th)));
41 [~, phiest] = min(abs(angfa - angAz + pi/2));            % mejor azimut
42 Daz=4*pi*dy*abs(FAaz(phiest)).^2/dpsi/sum(abs(FA_az(raz).^2));
43
44 [~, thest] = min(abs(angfa  - (pi/2- angEl)));              % mejor elevación
45 Del=4*pi*dz*abs(FAth(thest)).^2/dpsi/sum(abs(FA_el(rel).^2));
46 gain=Daz*Del;
47
48 end
```

`array2d` translates the continuous array-factor theory into a fully discrete routine:

It checks the input vectors and spacings, then builds a fine electric-angle grid of 721 points in order to emulate a continuous sweep. Using `freqz`, it evaluates the azimuth and elevation array factors on that grid, effectively reproducing the aperture's Fourier response in the discrete domain. The grid is converted back to real angles, the sample nearest to the desired steering direction is identified, ensuring the code matches the theoretical beam center to within a fraction of a degree. Finally, it computes azimuth and elevation directivities from the sampled peaks and multiplies them to obtain the composite gain passed to the OTDOA simulator.

5.4 Experimentation Scenarios

5.4.1 Baseline (Without RIS)

In the baseline scenario 5.2, the user-equipment (UE) position is estimated using standard PRS-based TDOA measurements, without any assistance from a reconfigurable intelligent surface (RIS).

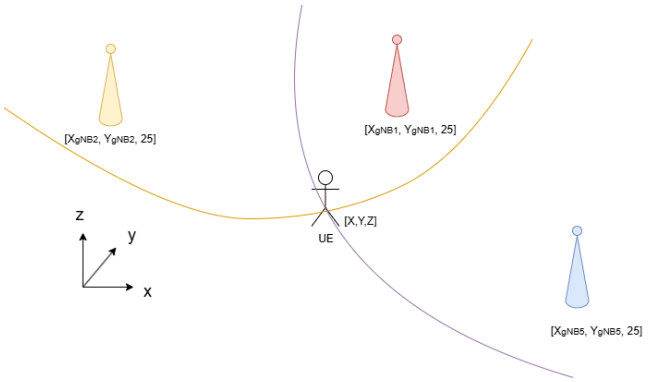

Figure 5.2: Three-gNB (2 gNB discarded) OTDOA geometry.

First, each gNB periodically transmits a Positioning Reference Signal (PRS) embedded within its downlink resource grid (Fig. 5.3). The PRS occupies a known set of subcarriers and OFDM symbols that are orthogonal across gNBs, enabling the UE to distinguish signals from different transmitters. In our experiments we use the MATLAB PRS Toolbox to generate the composite grid of PDSCH data and PRS from five gNBs; shaded regions in gray denote the PDSCH symbols, while colored hatch patterns indicate the PRS from each gNB .

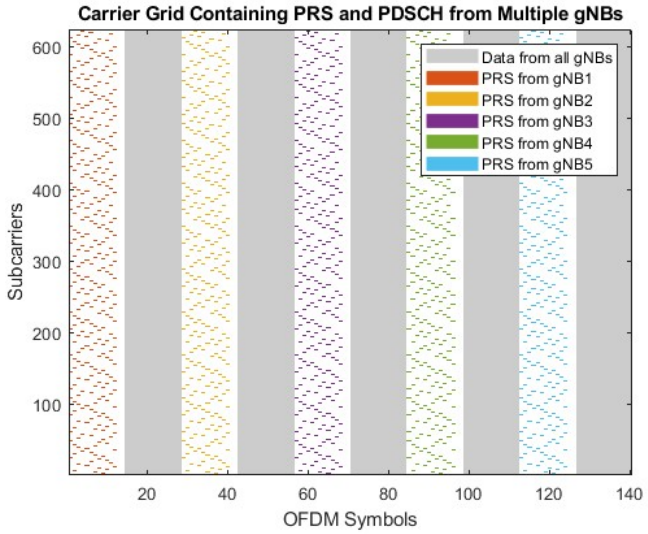

Figure 5.3: Carrier grid containing PRS and PDSCH from multiple gNBs. Code from [9]

Upon reception, the UE correlates its received waveform with each gNB's PRS sequence. As shown in Fig. 5.4, distinct peaks appear at delays corresponding to the propagation times from gNB 1-gNB 5 to the UE. By selecting gNB 1 as the reference transmitter, the difference in arrival times between gNB 1 and gNB i (for $i = 2, \ldots, 5$) produces hyperbolic information of possible UE positions.

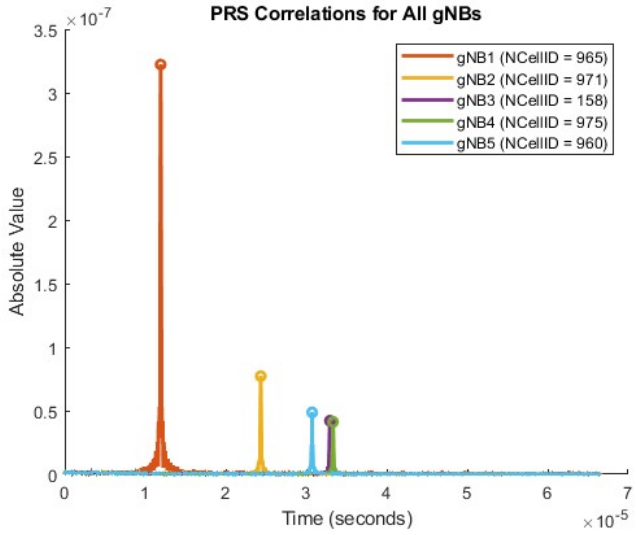

Figure 5.4: Correlation outputs for each gNB PRS: the peak locations encode the individual ToAs. Code from [9]

Geometrically, each TDOA measurement defines a branch of two hyperbola whose center are at the known gNB coordinates. The intersection of these hyperbolas localizes the UE in two dimensions. Fig. 5.5 illustrates the hyperbolic curves together with the true UE position (black circle) and the estimated UE position (red cross).

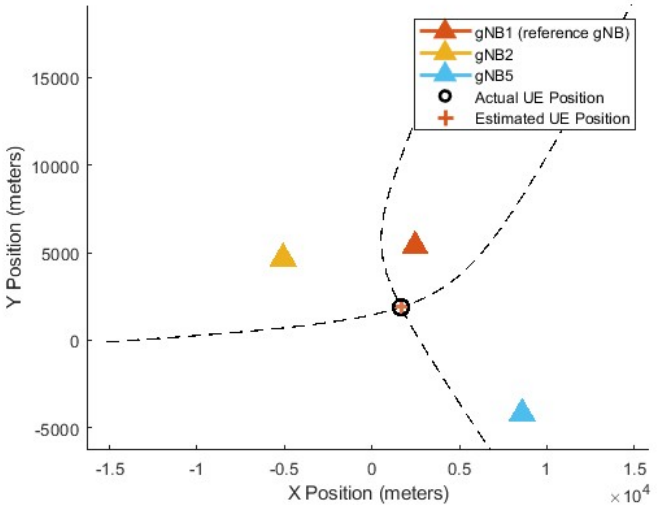

Figure 5.5: Hyperbolic TDOA curves (dashed) and resulting multilateration: true versus estimated UE position. Code from [9]

5.4.2 RIS Positioning

In Fig. 5.6 it is illustrated the RIS-assisted positioning scenario. The UE, located at $[X, Y, Z]$, receives two signal paths: a direct path from the gNB antenna at $[X_g, Y_g, Z_g]$ and a reflected path via the RIS located at $[X_r, Y_r, Z_r]$. By exploiting the time-difference-of-arrival (TDOA) between the direct and reflected signals, the UE position can be estimated using only a single gNB-RIS link, greatly reducing infrastructure cost compared to conventional multi-gNB setups.

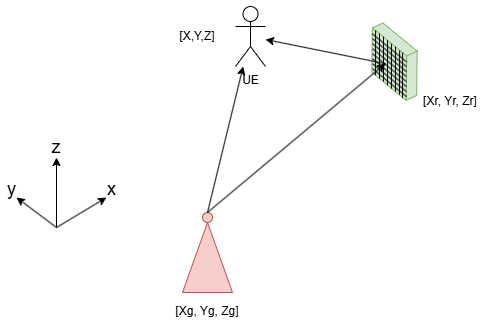

Figure 5.6: RIS-assisted positioning with one gNB and one RIS: solid line denotes the direct gNB-UE path; dashed line denotes the gNB-RIS-UE reflected path.

Angle of departure estimation

Returning to the angle-of-departure (AoD) estimation, we begin by transmitting the gNB PRS through the RIS channel, which applies its preconfigured gain matrix to steer energy into a discrete set of beam directions. The RIS sequentially re-radiates the signal in each of these angular beams, introducing a small, known time offset for each steering configuration. In order to simulate this sequence in MATLAB the Gain-coefficients will be multiplied to the RIS signal:

$$s_{\text{RIS}}[n, \phi k, \theta k] = s_{RIS}[n] G[\phi k, \theta k] \tag{5.11}$$

In the end we will obtain a signal multiplied $N_\phi \times N_\theta$ times, where N_ϕ is the number of steps in the azimuth sweep and N_θ is the number of steps in the elevation sweep.
At the UE, we compute the cross-correlation between the received signal and the known PRS sequence. The first correlation peak will correspond to the direct path, while the second peak will reveal the arrival time of the reflected RIS beam.

Firstly, we correlate the received signal $r(t)$ with the known PRS sequence $s(t)$:

$$\rho(\tau) \;=\; \int r(t)\, s^*(t-\tau)\, \mathrm{d}t \tag{5.12}$$

which produces two prominent peaks at delays τ_1 (direct gNB-UE path) and τ_2 (RIS-reflected path).

Next, we cycle through each RIS beam k defined by its azimuth-elevation pair (ϕ_k, θ_k), measure the amplitude of the second correlation peak

$$A_k = \left|\rho_k(\tau_2)\right| \tag{5.13}$$

and select the beam index

$$k^\star \;=\; \arg\max_k A_k \tag{5.14}$$

The steering angles $(\phi_{k^\star}, \theta_{k^\star})$ then provide our AoD estimates. When the RIS steers its azimuth from 270º through 180º to 90º, using the same gain-matrix configuration as in the previous example($(N_\phi, N_\theta) = (36, 30)$), if the elevation AoD is -1.85º and the azimuth AoD 180º, the $(N_{\phi max}, N_{\theta max}) = (18, 30)$ peak correlation magnitude will exhibit a single, dominant maximum at 180º. This clear peak directly identifies the correct azimuth AoD.

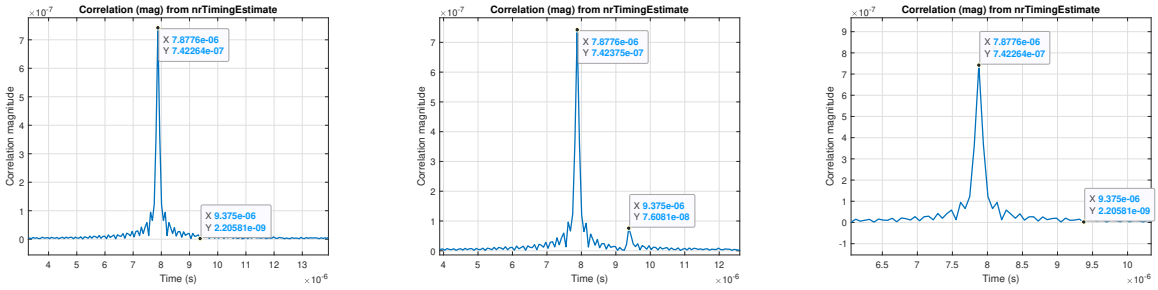

(a) Steering at ϕ =270º and $\theta = -30°$ (1,1)

(b) Steering at ϕ =180º and $\theta = -1.85°$ (18,30)

(c) Steering at ϕ =90º and $\theta = -1.85$ (36,30)

Figure 5.7: Correlation magnitude of the second PRS peak when the RIS sequentially steers at 270º, 180º, and 90º.

In MATLAB, we initially detect candidate peaks with the built-in findpeaks function. However, relying solely on peak amplitude can be misleading: if one of the expected peaks is missing, findpeaks may confuse the RIS-reflected peak for the direct gNB peak. To prevent this misidentification, we augment amplitude detection with a correlation metric. For each candidate peak, we compute its cross-correlation value; the true gNB peak will exhibit the highest correlation with our reference signal. In cases where the RIS peak is too weak or entirely absen it cannot be located, but the correlation step ensures that whenever both peaks exist, we consistently select the correct one. The MATLAB code employed was :

```
for GphiIdx = 1:numGphi
    for GthIdx = 1:numGth

     [~,RISmag] = nrTimingEstimate(RIScarrier, ...
         rxRISnoisy(:,GphiIdx,GthIdx),RISprsGrid);
     corrRIS{GphiIdx, GthIdx} = RISmag(1:(Ncorr));

```

```
8       [pks, locs] = findpeaks(corrRIS{GphiIdx, GthIdx}, ...
9           'SortStr','descend', 'NPeaks',2);
10      % Findpeaks gives the highest two peaks, sort them in time of arrival
11      if locs(2) < locs(1)
12      temp = locs(1);
13      locs(1) = locs(2);
14      locs(2) = temp;
15      pks = [pks(2),pks(1)];
16      end
17
18      peak1(GphiIdx,GthIdx)  = pks(1); % Estimated gNB peak
19      peak2(GphiIdx,GthIdx)  = pks(2); % Estimated RIS peak
20
21      delaygNB(GphiIdx,GthIdx) = locs(1)-1; % Estimated gNB sample delay
22      delayRIS(GphiIdx,GthIdx) = locs(2)-1; % Estimated RIS sample delay
23
24    end
25  end
26  % Add all the correlation, the correct phi and th should be NyxNz
27  sumCorr = cellfun(@sum, corrRIS);
28  [bestValue, linIdx]      = max(sumCorr(:));
29  [bestPhiIdx, bestThIdx]  = ind2sub(size(sumCorr), linIdx);
30
31
32  bestRISPeakValue = peak2(bestPhiIdx, bestThIdx);
33
34  % Range difference estimation:
35  difDist =  c*(delayRIS(bestPhiIdx, bestThIdx) - delaygNB(bestPhiIdx, bestThIdx))
        /ofdmInfo.SampleRate;
36
37  % Angle estimation:
38  estAz = (phi(1,bestPhiIdx));
39  estEl = th(bestThIdx);
```

Position estimation with RIS

The position can be estimated with an OTDOA (Observed Time Difference Of Arrival) method, as it is not necessary to have the UE clock synchronized with the gNB and RIS clocks. This method in plan view is illustrated in Figure 5.8:

Where $\alpha = 180° - AoD_{\phi}$ (to the UE) and $\beta = AoA_{RIS\phi} - 180°$ (From the gNB) With this scheme we are able to denote the position of X and Y. However, the elevation position of the user has still to be taken into account: Additionally, the elevation angles between the gNB, RIS, and UE are shown in the side (elevation) view in Figure 5.9:

Symbol	Parameter	Description
ϕ	RIS azimuth AoD to UE	Azimuth angle of departure from the RIS towards the user equipment
α	Cartesian AoD (180°–ϕ)	Complementary azimuth angle used in Cartesian coordinate mapping
β	RIS azimuth AoA from gNB (Cartesian)	Azimuth angle of arrival at the RIS from the gNB
γ	RIS elevation AoA from gNB (from +90° to –90°)	Elevation angle of arrival at the RIS from the gNB
θ	RIS elevation AoD to UE (from +90° to –90°)	Elevation angle of departure from the RIS towards the UE

Table 5.3: Definitions of RIS angular departure and arrival parameters

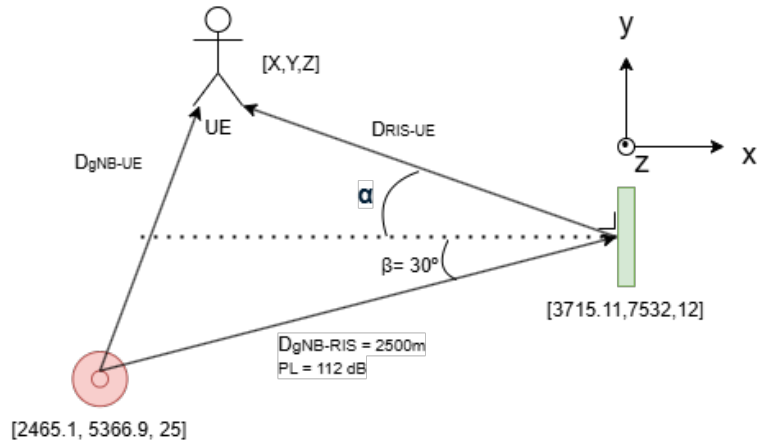

Figure 5.8: Plan view (bird's-eye view) of the OTDOA-based positioning scenario using the gNB, RIS, and UE.

Where $\gamma = AoA_{RIS\theta}$ and $\theta = AoD_{\theta}$. The elevation angles are from 90º to -90º. With these two illustrations, the position of the UE can be derived as follows:

$$D_{gNB-RIS} + D_{RIS-UE} - D_{gNB-UE} = \Delta_{distance} \tag{5.15}$$

The path-length difference Δ_{distance} can be directly extracted from the two correlation peaks. Let

$$\tau_1 = \arg\max_{\tau} \left|\rho(\tau)\right| \quad \text{(direct path lag)}, \tag{5.16}$$

$$\tau_2 = \arg\max_{\tau > \tau_1} \left|\rho(\tau)\right| \quad \text{(RIS path lag)}. \tag{5.17}$$

Then the time difference between these arrivals is

$$\Delta t = \tau_2 - \tau_1. \tag{5.18}$$

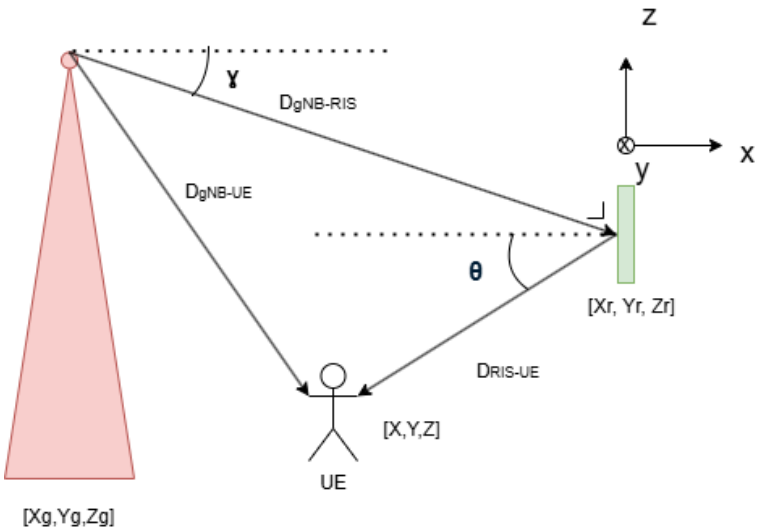

Figure 5.9: Elevation view of the OTDOA-based positioning scenario, illustrating the elevation angles θ (gNB-RIS-UE) and γ (gNB-UE).

Since propagation distance equals time multiplied by the speed of light c, the extra path length traversed by the RIS-reflected wave is

$$\Delta_{\text{distance}} = c\,\Delta t = c\,(\tau_2 - \tau_1). \tag{5.19}$$

In other words, by subtracting the two correlation-peak lags (in seconds) and scaling by c, we obtain the difference in path lengths directly from the correlation.

In MATLAB, in a discrete space, we will need to re-create this with the sample rate:

In this equation there are two unknowns yet, D_{RIS-UE} and D_{gNB-UE}, however, D_{gNB-UE} can be derived as:

$$D_{gNB-UE}^2 = X^2 + Y^2 + Z^2 \tag{5.20}$$

To simplify the algebra, we temporarily translate the coordinate system so that the gNB is at the origin:

$$\mathbf{p}_{\text{gNB}} = [0, 0, 0]. \tag{5.21}$$

In this "gNB-at-origin" frame:

$$\|\mathbf{p} - \mathbf{p}_{\text{gNB}}\| \;\longrightarrow\; \|\mathbf{p}\|, \tag{5.22}$$

and the TDoA equations become

$$\|\mathbf{p} - \mathbf{p}_i\| - \|\mathbf{p}\| = c\,\Delta t_i, \tag{5.23}$$

where $\mathbf{p} = [x, y, z]$ is the UE position in the shifted frame.

After solving for $\mathbf{p}$, we recover the true UE coordinates $\mathbf{P} = [X, Y, Z]$ by adding back the original gNB offset $\mathbf{p}_{\text{gNB}} = [X_g, Y_g, Z_g]$:

$$\hat{\mathbf{P}} = \hat{\mathbf{p}} + \mathbf{p}_{\text{gNB}} \quad \Longrightarrow \quad [x, y, z] = [\, X + X_g,\ Y + Y_g,\ Z + Z_g \,]. \tag{5.24}$$

The expression 5.20 can be separated by X, Y,Z:

$$\begin{aligned} X^2 &= \big(D_{g\text{NB–RIS}} \cos\beta \cos\gamma - D_{\text{RIS–UE}} \cos\alpha \cos\theta\big)^2 \\ &= D^2_{g\text{NB–RIS}} \cos^2\beta\ \cos^2\gamma - 2\, D_{g\text{NB–RIS}}\, D_{\text{RIS–UE}} \cos\beta\ \cos\gamma\ \cos\alpha\ \cos\theta + D^2_{\text{RIS–UE}} \cos^2\alpha\ \cos^2\theta. \end{aligned} \tag{5.25}$$

The Y position:

$$\begin{aligned} Y^2 &= \big(D_{g\text{NB–RIS}} \sin\beta \cos\gamma + D_{\text{RIS–UE}} \sin\alpha \cos\theta\big)^2 \\ &= D^2_{g\text{NB–RIS}} \sin^2\beta\ \cos^2\gamma + 2\, D_{g\text{NB–RIS}}\, D_{\text{RIS–UE}} \sin\beta\ \cos\gamma\ \sin\alpha\ \cos\theta + D^2_{\text{RIS–UE}} \sin^2\alpha\ \cos^2\theta. \end{aligned} \tag{5.26}$$

and

$$Z^2 = \big(D_{g\text{NB–RIS}} \sin\gamma + D_{\text{RIS–UE}} \sin\theta\big)^2 = D^2_{g\text{NB–RIS}} \sin^2\gamma + 2\, D_{g\text{NB–RIS}}\, D_{\text{RIS–UE}} \sin\gamma\ \sin\theta + D^2_{\text{RIS–UE}} \sin^2\theta. \tag{5.27}$$

When we sum the three equations for X^2, Y^2 and Z^2, the left-hand side becomes

$$X^2 + Y^2 + Z^2 \ = \ D^2_{\text{gNB–UE}}. \tag{5.28}$$

On the right-hand side, the coefficient multiplying $D^2_{\text{RIS–UE}}$ is

$$\sin^2\theta \ + \ \sin^2\alpha\ \cos^2\theta \ + \ \cos^2\alpha\ \cos^2\theta. \tag{5.29}$$

We recognize that $\sin^2\alpha + \cos^2\alpha = 1$, so

$$\sin^2\theta \ + \ \big(\sin^2\alpha + \cos^2\alpha\big)\cos^2\theta = \sin^2\theta + \cos^2\theta = 1. \tag{5.30}$$

Hence this entire bracket collapses to unity:

$$D^2_{\text{RIS–UE}}\big(\sin^2\theta + \sin^2\alpha\ \cos^2\theta + \cos^2\alpha\ \cos^2\theta\big) = D^2_{\text{RIS–UE}}. \tag{5.31}$$

Putting it all together, as the same occurs to $D_{\text{gNB–RIS}}$, the summed equation simplifies to

$$D^2_{\text{gNB–UE}} = D^2_{\text{gNB–RIS}} \ + \ 2\, D_{\text{gNB–RIS}}\, D_{\text{RIS–UE}}(\cdots) \ + \ D^2_{\text{RIS–UE}}, \tag{5.32}$$

where the mixed term $(\cdots)$ contains the cross-terms involving the various cosine and sine products.

Starting from the fundamental relation

$$D^2_{\text{gNB–UE}} \ = \ \big(D_{\text{gNB–RIS}} + D_{\text{RIS–UE}} - \Delta_{\text{distance}}\big)^2, \tag{5.33}$$

we observe that the only unknown is $D_{\text{RIS–UE}}$. Expanding the square gives:

$$D^2_{\text{gNB–UE}} = D^2_{\text{RIS–UE}} + 2\,D_{\text{RIS–UE}}\big(D_{\text{gNB–RIS}} - \Delta_{\text{distance}}\big) + \big(D_{\text{gNB–RIS}} - \Delta_{\text{distance}}\big)^2. \tag{5.34}$$

Inserting the equation from D_{gNB-UE}, we notice that there is only one solution to the equation, and it is:

$$\boxed{\widehat{D}_{\text{RIS–UE}} = \frac{D^2_{\text{gNB–RIS}} \;-\; \big(D_{\text{gNB–RIS}} - \widehat{\Delta}_{\text{distance}}\big)^2}{2\Big[D_{\text{gNB–RIS}}\big(1 - \cos\gamma\,\cos\widehat{\theta}\,(\sin\beta\,\sin\widehat{\alpha} - \cos\gamma\,\cos\widehat{\theta})\big) + \sin\gamma\,\sin\widehat{\theta} - \widehat{\Delta}_{\text{distance}}\Big]}}$$

And we finally obtain the estimated position:

$$\boxed{\widehat{x} = D_{g\text{NB–RIS}}\,\cos\beta\,\cos\gamma \;-\; \widehat{D}_{\text{RIS–UE}}\,\cos\widehat{\alpha}\,\cos\widehat{\theta} \;+\; X_g} \tag{5.35}$$

$$\boxed{\widehat{y} = D_{g\text{NB–RIS}}\,\sin\beta\,\cos\gamma \;+\; \widehat{D}_{\text{RIS–UE}}\,\sin\widehat{\alpha}\,\cos\widehat{\theta} \;+\; Y_g} \tag{5.36}$$

$$\boxed{\widehat{z} = D_{g\text{NB–RIS}}\,\sin\gamma \;+\; \widehat{D}_{\text{RIS–UE}}\,\sin\widehat{\theta} \;+\; Z_g} \tag{5.37}$$

This estimation is performed in MATLAB by the function solvePOS:

```
function xy_est = solvePOS(drest, dgNBRIS, betaAz, alphaAz, gNBPOS, estTH,
psi)

alpha = pi - alphaAz ;
beta = betaAz - pi;


Xg =  gNBPOS(1);
Yg =  gNBPOS(2);
Zg = gNBPOS(3);
num = (dgNBRIS)^2 - (dgNBRIS - drest)^2;
den = 2*( dgNBRIS*(1 - cos(psi)*cos(estTH)*(sin(beta)*sin(alpha) - cos(beta)*cos
    (alpha)) + sin(psi)*sin(estTH)) - drest);
if abs(den) < eps
    error('very small denominator; revise beta and alpha.');
end
dRU = num / den;


% XYZ


x = dgNBRIS*cos(beta)*cos(psi) - dRU*cos(alpha)*cos(estTH) + Xg;
```

```
y = dgNBRIS*sin(beta)*cos(psi) + dRU*sin(alpha)*cos(estTH) + Yg;
z = dgNBRIS*sin(psi) + dRU*sin(estTH) + Zg;
xy_est = [x, y, z];
end
```

Chapter 6

Results and Discussion

6.1 Simulation Parameters Constraints

6.1.1 Minimum separation and power threshold

Prior to running any simulation, we must first establish the key constraints that ensure our results are meaningful. In particular, the two correlation peaks, one from the direct gNB-UE path and one from the RIS-reflected path must remain distinguishable:
Minimum separation: If the UE is too close to the RIS, the time difference between the direct and reflected arrivals becomes vanishingly small, causing the two peaks to merge.

Sufficient reflection strength: If the RIS-reflected signal is weaker than the direct gNB path, the RIS peak will be buried beneath the larger direct-path correlation.

Only when both conditions are met can we reliably identify and measure the RIS-related correlation peak. The example below illustrates how violating either constraint prevents accurate peak differentiation.

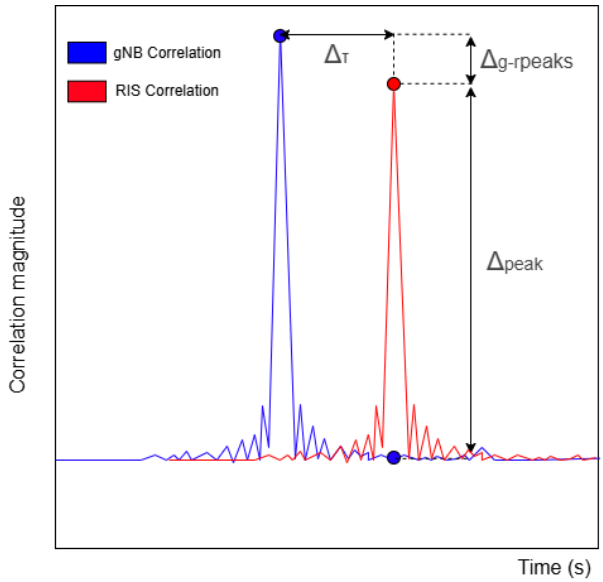

Figure 6.1: Relative timing and amplitude of the gNB (blue) and RIS (red) correlation peaks.

As illustrated in Figure 6.1, the time separation $\Delta\tau$ between the direct gNB-UE and RIS-UE correlation peaks grows linearly with the extra path-length difference Δd:

$$\Delta\tau \;=\; \frac{\Delta d}{c}. \tag{6.1}$$

At the same time, the amplitude difference Δ_{peak} between the two peaks shrinks as the RIS path becomes weaker (due to greater propagation loss), making the RIS peak harder to distinguish from noise or sidelobes.

Although one can increase the geometric separation between the direct and reflected peaks, the *intrinsic* resolution of the receiver is fixed by a single, tightly-coupled design choice: the PRS sequence is generated so that its autocorrelation falls off at the *second* sample, that fall-off is itself governed by the occupied bandwidth B, and the OFDM sampling rate F_s is then selected as the next power of two to satisfy Nyquist for that very bandwidth. In other words, bandwidth, sequence properties and sampling rate are not independent constraints but three facets of the same specification. The resulting lower bound on the resolvable delay is

$$\Delta\tau_{\min} \;\geq\; \frac{1}{B} = \frac{1}{N_{\text{RB}}\, N_{\text{SC}}\, \Delta f_{\text{SC}}}, \qquad N_{\text{RB}} = 52,\; N_{\text{SC}} = 12,\; \Delta f_{\text{SC}} = 15\ \text{kHz}, \tag{6.2}$$

which in our system gives

$$\Delta\tau_{\min} \;\approx\; 2.6 \times 10^{-7}\ \text{s} \quad\Longrightarrow\quad \Delta d_{\min} = c\,\Delta\tau_{\min} \;\approx\; 32\ \text{m}. \tag{6.3}$$

Because the PRS autocorrelation already decays by roughly 10 dB at the second sample,

choosing a faster sampling clock would only add redundant points between the same two correlation lobes and would not improve the fundamental path-difference resolution. The MATLAB example reflects this rationale by assigning $F_s = 15.36$ MHz, the smallest power-of-two rate that fully covers the stated bandwidth [9].

When the time separation between the direct and RIS-reflected arrivals $\Delta\tau$ falls below the system's minimum resolvable delay $\Delta\tau_{\min}$, the two correlation peaks merge into a single, broadened lobe. In order to unambiguously detect the RIS contribution, the correlation function must exhibit two distinct maximum peaks separated by a clear valley. Equivalently,

$$\Delta\tau > \Delta\tau_{\min} \implies \text{two resolvable peaks with an intervening minimum,} \tag{6.4}$$

whereas

$$\Delta\tau \leq \Delta\tau_{\min} \implies \text{peak overlap and loss of RIS detectability.} \tag{6.5}$$

If Δ_{peak} falls below the gNB correlation or noise floor , the RIS peak disappears entirely. Firstly we can define Δ_{peak}:

If the RIS-reflected peak amplitude drops below either the direct-path correlation or the noise floor, it becomes impossible to distinguish, and the RIS contribution is effectively lost. To quantify this, we define the relative peak strength as

$$\Delta_{\text{peak}} = \frac{max[|corr_{RIS}(n_k)|]}{|corr_{gNB}(n_k)|} \tag{6.6}$$

A RIS-Peak-to-gNB-value difference threshold Δ_{Pth} must be chosen so that

$$\Delta_{\text{peak}} > \Delta_{\text{Pth}} \quad \Longrightarrow \quad \text{RIS peak reliably detected.} \tag{6.7}$$

Because the gNB direct-path correlation amplitude varies with geometry and path loss, a fixed ratio threshold does not translate into a fixed absolute requirement:

Near RIS-UE separation: The direct-path peak is strong, so even $\Delta_{\text{peak}} \approx 1.5$ produces a RIS peak well above sidelobes and noise.
Far RIS-UE separation: The direct-path peak is weaker, so the same ratio $\Delta_{\text{peak}} = 1.5$ may lie at or below the sidelobe/noise floor, making detection ambiguous. In such regimes, we may require Δ_{peak} to be as high as 25 to guarantee a clear RIS peak. We can define the threshold as:

$$\Delta_{G\text{–}RPeaks} = \frac{\max\limits_{n}\left|\text{corr}_{\text{gNB}}(n)\right|}{\max\limits_{n}\left|\text{corr}_{\text{RIS}}(n)\right|}. \tag{6.8}$$

$$\Delta_{Pth} \;=\; \Delta_{G\text{–}RPeaks}. \tag{6.9}$$

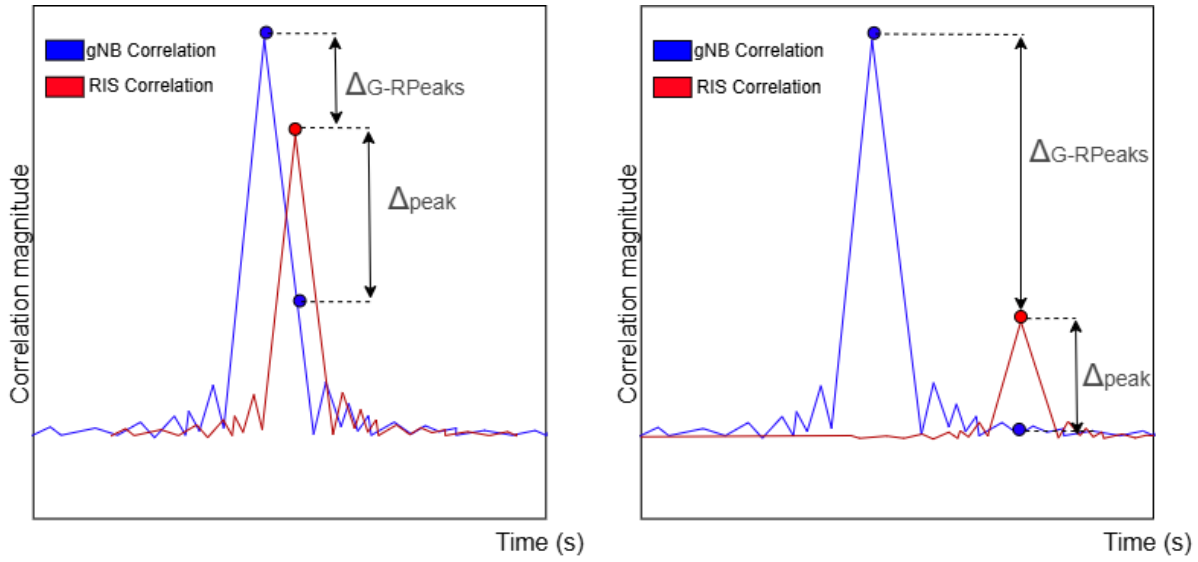

Figure 6.2: Peak–amplitude ratio between the direct gNB correlation (blue) and the RIS-assisted correlation (red) for two UE–RIS distances. **Left:** short separation, both peaks stand well above noise, so even a small ratio is reliable. **Right:** long separation, the RIS peak suffers extra path-loss; the same ratio may sink into the sidelobes, making the decision ambiguous.

When the UE is positioned very close to the RIS, the reflected signal strength becomes comparable to the direct gNB signal, so the detection threshold naturally remains low only a small margin is needed to pick out the RIS peak. As the UE moves farther away, the RIS reflection weakens much more than the direct path, so the relative gap between peaks grows and the threshold must rise accordingly. This behavior perfectly matches our earlier insight that a near RIS-UE separation allows a low detection bar, while larger distances demand a higher bar to reliably identify the RIS contribution.

6.1.2 Gain and Path Loss

Accurate modeling of gain and path loss is essential in RIS-assisted propagation, since the signal travels two separate legs, gNB to RIS, then RIS to UE before reaching the receiver. At the RIS, the incident wave is re-radiated through a planar aperture of $M \times N$ elements, which provides a substantial beamforming gain along the steered direction.

For a 50×50 element RIS (half-wavelength spacing, isotropic re-radiators), the peak array gain can be approximated by the element count:

$$D_{\mathrm{az}}(\phi_i) = \frac{2\,k\,d_y\,\left|AF_{\mathrm{az}}(\Psi_{\mathrm{real}})\right|^2}{\Delta\Psi\,\sum_{\Psi}\left|AF_{\mathrm{az}}(\Psi)\right|^2}, \quad \Psi_{\mathrm{real}} = -k\,d_y \sin\phi_{\mathrm{real}}, \tag{6.10}$$

$$D_{\mathrm{el}}(\theta_j) = \frac{2\,k\,d_z\,\left|AF_{\mathrm{el}}(\Phi_{\mathrm{real}})\right|^2}{\Delta\Phi\,\sum_{\Phi}\left|AF_{\mathrm{el}}(\Phi)\right|^2}, \quad \Phi_{\mathrm{real}} = -k\,d_z\sin\theta_{\mathrm{real}}. \tag{6.11}$$

For a uniformly excited $M \times N$ planar array with half-wavelength spacing ($d_y = d_z = \frac{\lambda}{2}$), the broadside steering angles satisfy $\cos\phi_{\mathrm{real}} = 0$, $\cos\theta_{\mathrm{real}} = 0$, so

$$AF_{\mathrm{az}}(0) = \sum_{m=0}^{M-1} 1 = M, \quad AF_{\mathrm{el}}(0) = \sum_{n=0}^{N-1} 1 = N. \tag{6.12}$$

Meanwhile, the denominator sums (approximating the continuous integral of $|AF|^2$) evaluate to

$$\Delta\Psi \sum_{\Psi}\left|AF_{\mathrm{az}}(\Psi)\right|^2 \approx 2\pi\,M, \quad \Delta\Phi \sum_{\Phi}\left|AF_{\mathrm{el}}(\Phi)\right|^2 \approx 2\pi\,N. \tag{6.13}$$

Substituting into the directivity equations gives

$$D_{\mathrm{az}}^{\max} = \frac{2\,k\,(\frac{\lambda}{2})\,M^2}{2\pi\,M} = M, \quad D_{\mathrm{el}}^{\max} = \frac{2\,k\,(\frac{\lambda}{2})\,N^2}{2\pi\,N} = N. \tag{6.14}$$

Finally, the composite gain in the boresight direction is

$$G_{\max} = \underbrace{D_{\mathrm{az}}^{\max}}_{=M} \times \underbrace{D_{\mathrm{el}}^{\max}}_{=N} \times \eta = M\,N\,\eta. \tag{6.15}$$

For our 50×50 RIS with efficiency $\eta = 0.8$, this produces

$$G_{\max} = 50 \times 50 \times 0.8 = 2000 \quad \big(\approx 33\ \mathrm{dBi}\big). \tag{6.16}$$

Each propagation leg incurs a free-space path loss, taking into account it is in a Urban Macro:

$$\alpha(d) \propto 10\log_{10}\Big(\tfrac{4\pi d}{\lambda}\Big), \tag{6.17}$$

so that the total two-hop power balance from the gNB to UE via the RIS becomes

$$\underbrace{\alpha_{\mathrm{gNB\text{–}RIS}}}_{\approx 56\ \mathrm{dB}} + \underbrace{\alpha_{\mathrm{RIS\text{–}UE}}}_{\text{(geometry-dependent)}} - \underbrace{G_{\max}}_{\approx 33\ \mathrm{dBi}} \tag{6.18}$$

6.1.3 Simulation scenario

In our chosen scenario, we place the RIS at a 2.5 km distance from the gNB, exactly halfway to the cell edge, because, per our link-budget table, a 5 km gNB-UE separation corresponds to roughly 10 dB of SNR. By positioning the RIS at 2.5 km, we ensure that the gNB-RIS link enjoys a comfortable margin above this threshold, while still sampling a realistic mid-range propagation environment. Coupled with a variable RIS-UE distance, this setup produces reaalistic received-power levels for our OTDOA-via-RIS simulations.

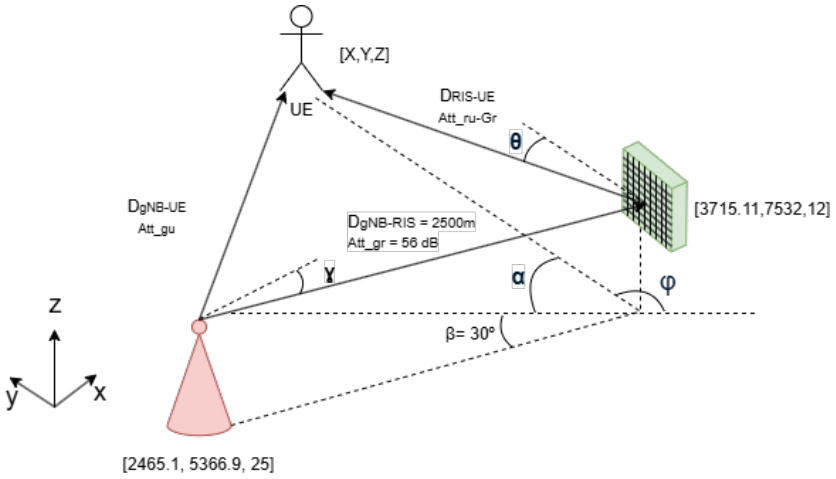

Figure 6.3: Realistic RIS-assisted positioning scenario: the gNB at the origin, the RIS at [3715.11, 7532, 12], and the UE at [2465.1, 5366.9, 25]. The known elevation angles are $\beta = 30°$, $\gamma = -0.3°$, and the UE azimuth angle α. Attenuation losses and RIS gain (33 dB) have been applied.

Taking into account all of the parameters defined above (gNB-RIS separation, RIS aperture directivity and efficiency, free-space path loss in the UMa model, and steering angles), the resulting deployment geometry is illustrated in Figure 6.3:

To reduce complexity, we will conduct a systematic angular sweep from 180° down to 90°, with a 5^{o} step, and a longitudinal sweep from 20 m (almost the minimum resolution) to 310 m, with a 10 meters step. At each steering angle, we will assess whether the RIS-reflected correlation peak remains detectable by comparing it against the detection thresholds summarized in the section 6.1.1. This procedure allows us to pinpoint exactly which angular sectors, and under which threshold conditions the OTDOA-via-RIS approach succeeds. Notice that, the RIS's angle of departure ϕ is converted into the cartesian by $\alpha = 180 - \phi$

6.2 Performance Results

Table 6.1: Definition of the UE–RIS azimuth Angle of Departure

Symbol	**Name in plots**	**Physical meaning ("UE–RIS Angle (°)")**
ϕ (AoD)	UE–RIS Angle (°)	Real Azimuthal Angle of Departure at the RIS toward the user equipment (UE). This quantity is the horizontal axis of the following plots and many of the plots afterwards.

This table is included so that reader can immediately recognize that the quantity shown on the horizontal axis of the following plots is the azimuthal AoD ϕ defined at the RIS.

6.2.1 RIS Coverage

To quantify the spatial extension provided by the RIS, we executed the full simulation chain, incorporating the angular sweep, distance steps, and distance and delay thresholds defined in Section 6.1.1. From these experiments, we extracted the following coverage metrics: Figure 6.4 shows the two key correlation-peak ratios on the same axes:

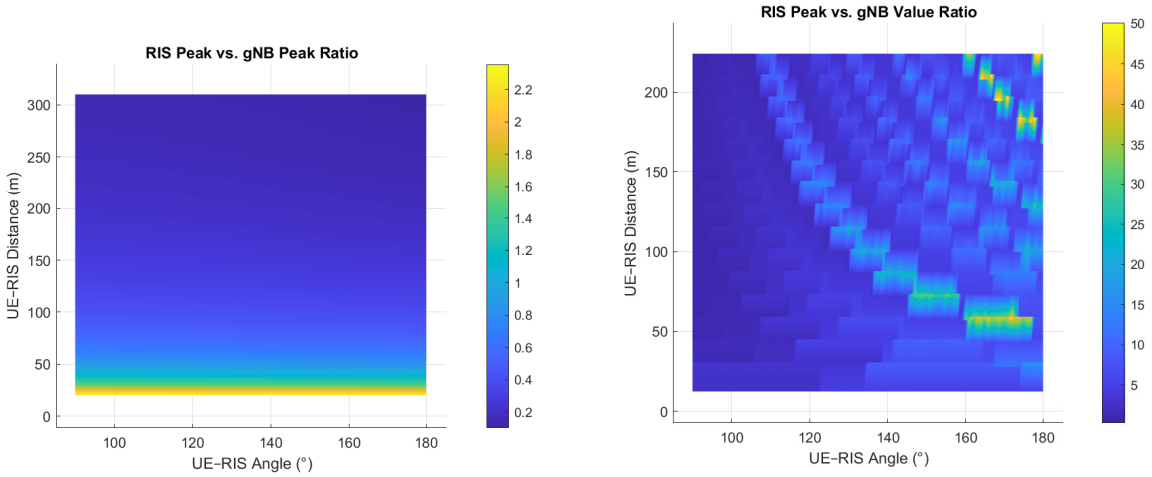

(a) RIS peak / gNB peak

(b) RIS peak / gNB value

Figure 6.4: Surface plots of the two correlation-peak ratios as functions of UE-RIS angle (RIS's Angle of Departure ϕ) and distance.

The first plot, shown in Figure 6.4a, illustrates the difference between the gNB and RIS peak amplitudes, $\Delta_{G-R\,\text{Peaks}}$. Although the overall scale masks small variations, the right-hand side of the curve (near an AoD of 180°) consistently lies below the left side. This asymmetry is produced because the gNB is closer in that place and the RIS-reflected signal power starts high for a small path distance and then decreases as the path distance increases. As a result, the lower magnitudes at larger departure angles are harder to discern at first glance. However, a closer inspection reveals that the peak on the top-right (180° and 310m) is approximately 50 percent lower than the corresponding peak on the top-left (90° and 310m), directly reflecting the increasing path difference with departure angle.
Notice in Figure 6.4b that the RIS-to-gNB correlation-value ratio steadily increases as the UE-RIS azimuth approaches 180º. Geometrically, this corresponds to the RIS steering direction aligning exactly with the true propagation path from the gNB, which maximizes the reflected signal strength. Simultaneously, Figure 6.6 shows that the path-difference Δd also peaks near

180^{o}, producing the largest time separation between direct and reflected arrivals. The second plot, shown in Figure 6.4b, illustrates the difference between RIS peak amplitude and the value of the gNB correlation in that place, $\frac{1}{\Delta_{\text{Peak}}}$.

Next, Figure 6.5 shows the detection flag indicating where neither (0), one (1), or both (2) of our peak-strength and delay-separation criteria are met if the RIS is beaming directly to the UE:

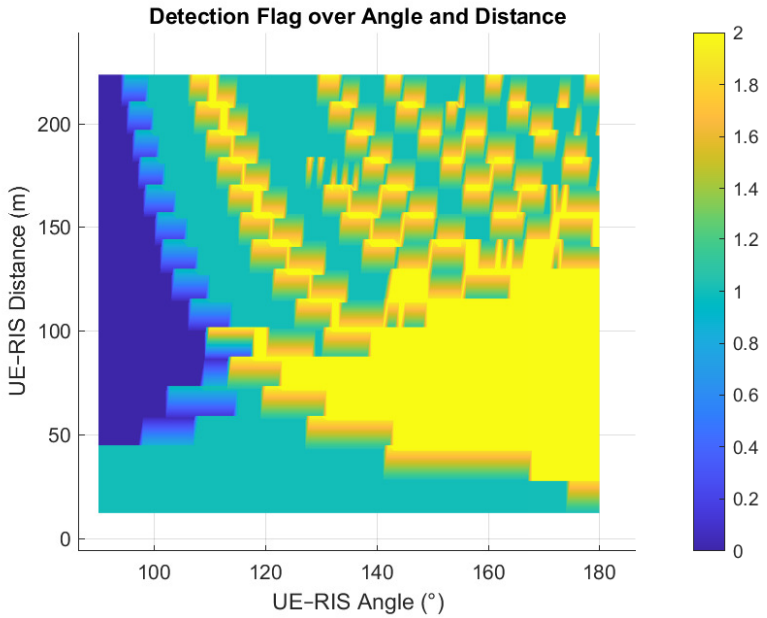

Figure 6.5: Maximum theoretical Detection flag surface over UE-RIS angle and distance.

Conversely, as the azimuth moves toward 90^{o}, Δd shrinks (the two paths converge in length) and the total RIS link angles $\alpha + \beta = 30 + 90 = 120°$ becomes more obtuse, causing the reflected and direct signals to arrive nearly simultaneously. In this regime, the RIS peak is both weaker relative to the gNB peak and unresolved in time, so fewer detection conditions hold.

This dual dependence on amplitude and timing explains why the detection flag in Figure 6.5 reaches its maximum value of 2 around 180^{o} (both criteria met) and falls toward 0-1 as the angle approaches 90^{o}.

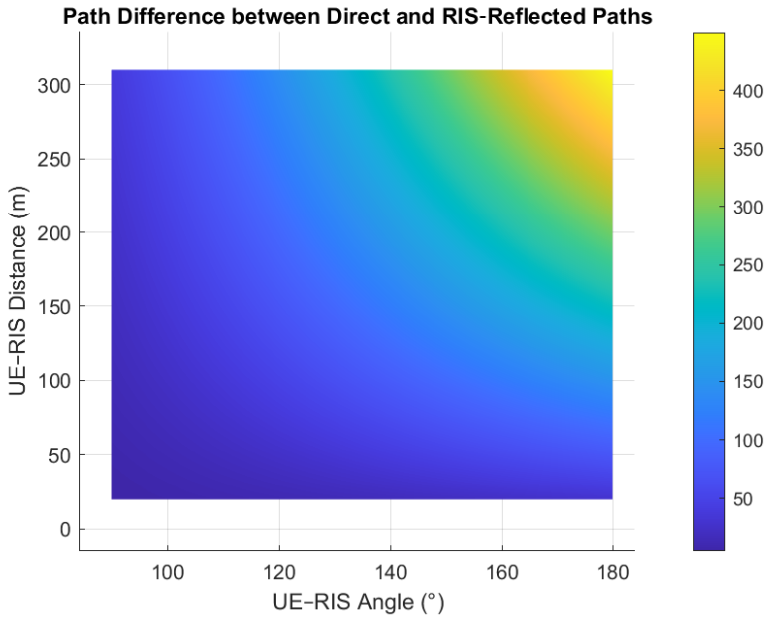

Figure 6.6: Path-difference Δd between the direct and RIS-reflected paths as a function of UE-RIS angle and distance.

6.2.2 Signal-to-Noise Ratio (SNR)

Figure 6.7 shows the received SNR surfaces for both the gNB direct path and the RIS-reflected path as functions of UE-RIS angle and distance:

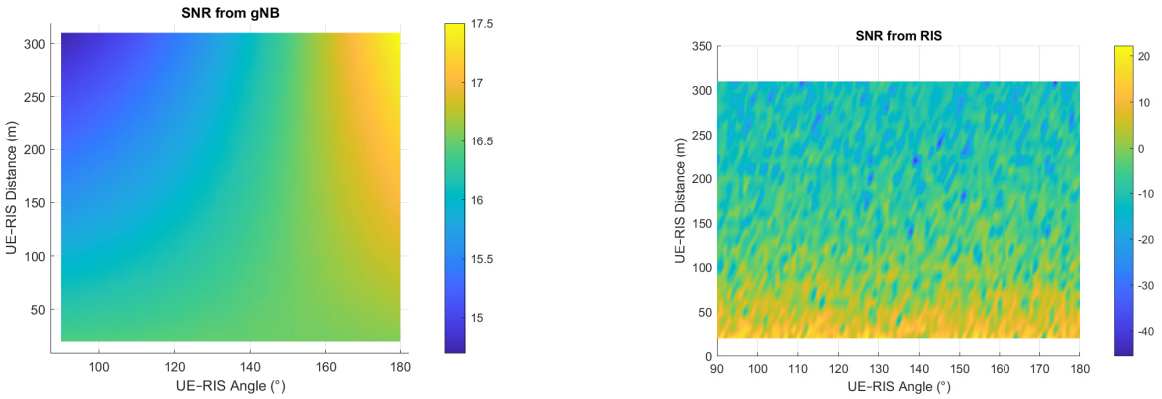

(a) SNR from gNB

(b) SNR from RIS

Figure 6.7: Spatial distribution of received SNR: (a) direct gNB signal and (b) RIS-reflected signal.

A close inspection reveals that the gNB's direct-path SNR peaks in the top-right region of the plane (Were the gNB is closer to the UE). By contrast, the RIS-reflected SNR is maximized

in the lower portion of the plot, where the UE-RIS distance is smallest and path loss is minimal.

The overlap of these two high SNR regions, specifically the bottom-right quadrant poses as the optimal coverage zone for our estimation. In this region, both the direct and reflected signals arrive with sufficient strength to satisfy our amplitude and timing detection thresholds simultaneously, produceing the most reliable positioning performance.

6.2.3 Positioning Accuracy

To quantify the error in our RIS-UE distance estimate, we revisit the analytic solution in Eq. 5.4.2:

$$D_{\text{RIS–UE}} + \epsilon_{\text{RIS–UE}} = \frac{D_{\text{gNB–RIS}}^2 \; - \; \big(D_{\text{gNB–RIS}} - (\Delta_{\text{d}} + \epsilon_{\text{d}})\big)^2}{2\Big[D_{\text{gNB–RIS}}\big(1 - \cos\gamma\,\cos(\theta+\epsilon_\theta)\big(\sin\beta\,\sin(\alpha+\epsilon_\alpha) - \cos\gamma\,\cos(\theta+\epsilon_\theta)\big)\big) + \sin\gamma\,\sin(\theta+\epsilon_\theta) - (\Delta_{\text{d}} + \epsilon_{\text{d}})\Big]}$$

The total system error $\epsilon_{\text{RIS–UE}}$ results from three error quantification:

Path–difference error ϵ_d. The minimum delay that the receiver can resolve is

$$\Delta_{\text{res}} = \frac{c}{F_s}. \tag{6.19}$$

In the worst case, the gNB path arrives $\frac{1}{2}\Delta_{\text{res}}$ early while the RIS path arrives $\frac{1}{2}\Delta_{\text{res}}$ late and vice-versa, so the path-difference error is bounded by

$$\epsilon_d < \Delta_{\text{res}}. \tag{6.20}$$

Azimuth error ϵ_ϕ: Using a Δ_ϕ step in azimuth, the worst-case steering offset is $\epsilon_\phi = \Delta_\phi/2$

Elevation error ϵ_θ: Likewise, the elevation sweep step Δ_θ imposes $\epsilon_\theta = \Delta_\theta/2$.

Furthermore, the RIS's inherently high directivity imposes its own angular step limit. In the boresight direction, the array's maximum directivity is

$$D_{\max} \approx \frac{4\pi}{\Delta_{-3\text{dB}\,\phi}\,\Delta_{-3\text{dB}\,\theta}} = \frac{4\pi}{\Delta_{-3\text{dB}}^2} = 2500, \tag{6.21}$$

which implies a half-power beamwidth of

$$\Delta_{-3\text{dB}} = \sqrt{\frac{4\pi}{2500}} \approx 0.0709 \text{ rad} \approx 4.06^\circ. \tag{6.22}$$

This means that, even if our steering is off by up to $\pm 2^\circ$ in both azimuth and elevation, the RIS still delivers at least one quarter of its peak gain (-6 dB).

In practice, when programming the RIS phase shifts, we must therefore choose an angular step no larger than this beamwidth (4°) to lock onto the true AoD with sub-2-degree precision.

This balance between maximum directivity and grid spacing is critical: coarse enough to limit beam-steering commands, yet fine enough to maintain near-maximal gain on the UE.
For the error estimation simulation, we configure the following parameter grid:

Azimuth sweep: RIS phase shifts steer the beam from 180° down to 90° in uniform 5° increments.

Elevation sweep: RIS phase shifts are preloaded in 30 logarithmically spaced settings between 30° and -1.8486°.

UE geometry: The UE's azimuth mirrors the RIS sweep (180° to 90° in 5° steps), and its distance varies from 20m to 310m.
RIS elevation diversity: IF both the RIS and gNB are in the same elevation position, the Z error will increment, due to the fact that the Z estimation will solely be composed by the estimation of D_{RIS-UE} and θ.

6.3 Experimental Results

Building on the framework outlined previously, this section presents our empirical evaluation of RIS-assisted OTDOA positioning in an urban macro environment. Our goal is to evaluate how a strategically deployed RIS can improve 3D localization accuracy in dense cityscapes, where direct gNB signals alone often fail to meet stringent SNR and timing requirements. In this section, we compare the positioning errors from the MATLAB gNB scenario with those from our initial RIS-assisted setup, evaluating the RIS's impact on coverage and accuracy.

6.3.1 Baseline Results

In the baseline scenario , we apply the standard PRS-TDoA algorithm without any RIS assistance. Importantly, the UE is placed in the middle of the 1st gNB coverage zone (2500m) and the limit of the two gNB coverage zones (5000m with SNR=10dB) .

Before analyzing axis-by-axis performance, we first examine the overall three-dimensional error surface produced by the gNB OTDOA algorithm.

$$\mathrm{Err}_{3\mathrm{D}} = \sqrt{(x_{\mathrm{est}} - x_{\mathrm{true}})^2 + (y_{\mathrm{est}} - y_{\mathrm{true}})^2 + (z_{\mathrm{est}} - z_{\mathrm{true}})^2}, \tag{6.23}$$

Figure 6.9 presents the resulting positioning error surfaces, total 3-D error and its X, Y, and Z components, over the 180°-90° azimuth (α from 0^{o} to 90^{o})and 20-310 m range grid used for the gNB case.

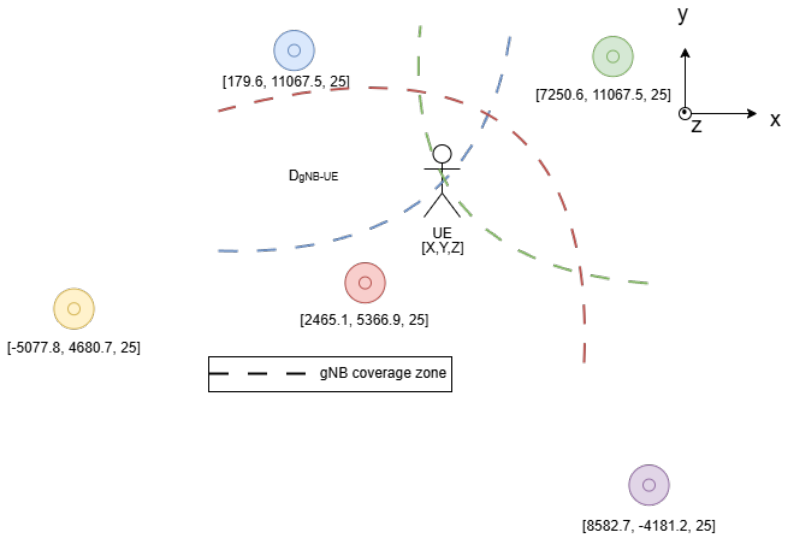

Figure 6.8: gNB baseline scenario, UE inside the coverage zone of the gNB 1 and in the limit of the 2 other gNB coverage zones

To pinpoint which coordinate limits accuracy, we separate the total error into its X, Y, and Z components:

$$\begin{aligned} e_x &= |x_{\text{est}} - x_{\text{true}}|, \\ e_y &= |y_{\text{est}} - y_{\text{true}}|, \\ e_z &= |z_{\text{est}} - z_{\text{true}}|. \end{aligned} \tag{6.24}$$

In this scenario, unlike the toolbox, the estimation of the elevation component Z was added.

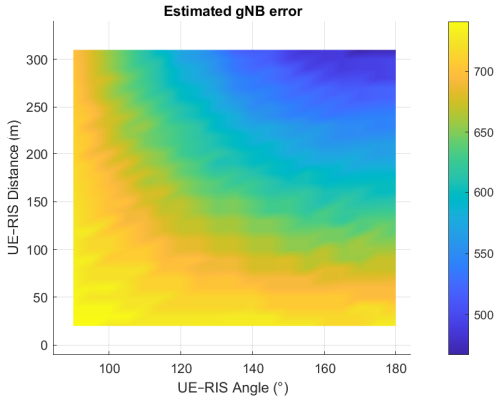

(a) Total 3D error

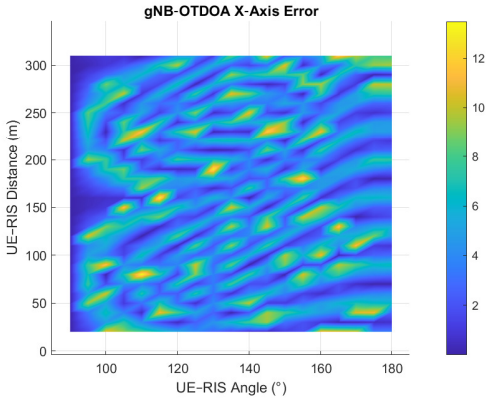

(b) X-axis error

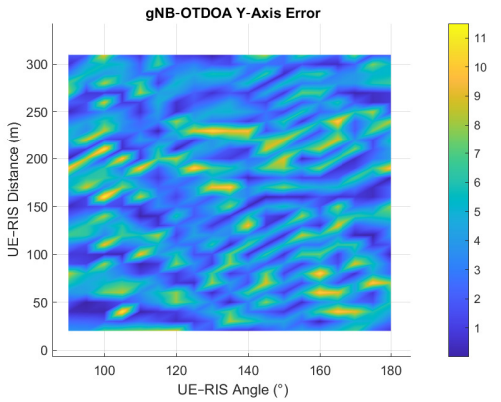

(c) Y-axis error

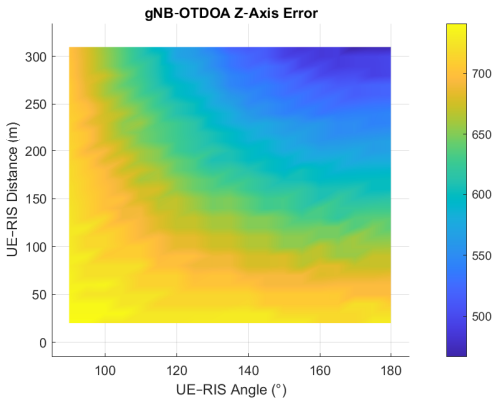

(d) Z-axis error

Figure 6.9: Positioning error surfaces for the three-gNB OTDOA scenario: (a) total 3D error, (b) X-component, (c) Y-component, (d) Z-component.

Although the horizontal positioning errors along the X and Y-axes remain low, never exceeding $\approx 12\,\mathrm{m}$, the vertical error Z grows to several hundred metres. This imbalance arises from the previously discussed elevation-diversity deficit: because all received signals arrive from nearly identical elevation angles, the estimator obtains virtually no height information and therefore converges to an arbitrary altitude.

Figure 6.10 visualises this phenomenon through histograms of the overall three-dimensional error and of each Cartesian component. The mean horizontal errors are modest, at $\bar{e}_X = 4.23\,\mathrm{m}$ and $\bar{e}_Y = 3.92\,\mathrm{m}$, whereas the mean vertical error rises to $\bar{e}_Z \approx 750\,\mathrm{m}$.

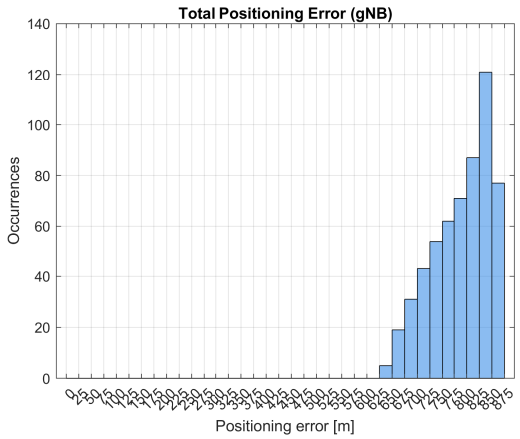

(a) Total 3D error categories

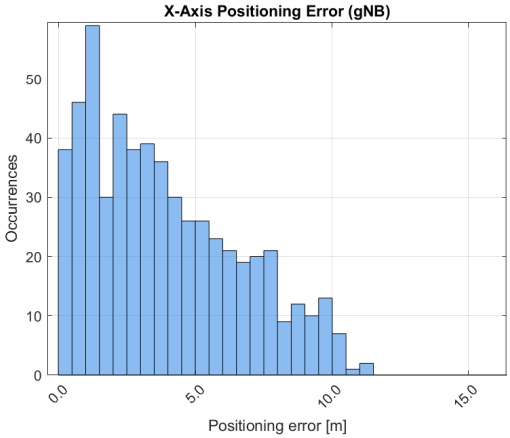

(b) X-axis error categories

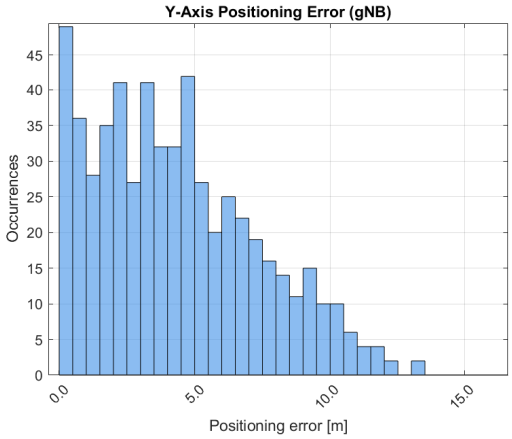

(c) Y-axis error categories

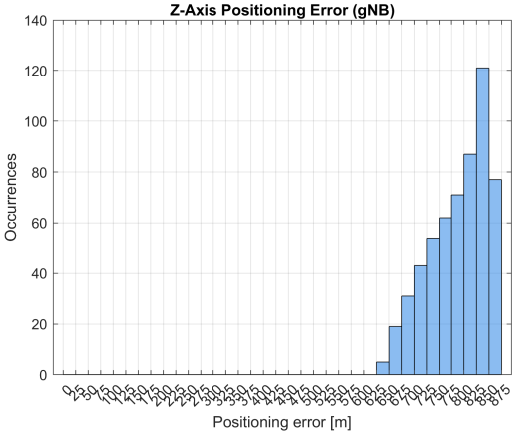

(d) Z-axis error categories

Figure 6.10: Distribution of positioning estimates across error bands for the baseline gNB OTDOA case.

Because the Z component dominates the Euclidean error, essentially the entire three-dimensional error is driven by the vertical dimension, completely masking the otherwise precise azimuth plane estimates.

This outcome highlights a crucial design insight: without sufficient elevation diversity, even a well-conditioned horizontal geometry cannot guarantee reliable three-dimensional positioning.

6.3.2 RIS Results

Before analyzing axis-by-axis performance, we first examine the overall three-dimensional error surface produced by the RIS-assisted OTDOA algorithm. Figure 6.11 plots the total Euclidean error across the full $180° \rightarrow 90°$ azimuth sweep ($\alpha = 0° \rightarrow 90°$)and 20-310 m UE-RIS distance

grid. In these section we will analyze the error and where it comes that error

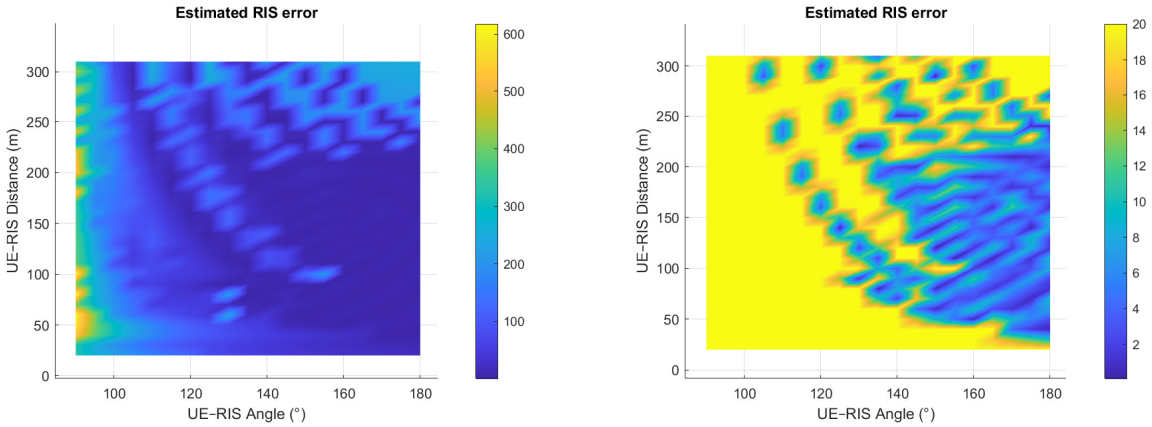

(a) Full–scale view

(b) Zoomed to 20 m limit

Figure 6.11: Total 3-D positioning error obtained from the RIS-reflected path. Panel (a) shows the full error range, while panel (b) zooms into the 0–20 m region where sub-10 m accuracy (blue) coincides with the "flag = 2" area of Fig. 6.5.

Consistency with power and delay thresholds. A point-by-point comparison with the detection flag map in Fig. 6.5 reveals that whenever the flag takes its maximum value (2), meaning both SNR and timing criteria are met, the positioning error drops below 10 m. In contrast, in cells where the flag is 0 or 1, the error quickly exceeds 50 m. This strong correspondence confirms that our threshold logic not only signals "RIS peak found" but also accurately predicts the resulting localization quality. Accurate positioning is achieved only when both conditions the distance-difference constraint and the received-power threshold are satisfied. When this happens, the user's location can be determined reliably. If only one condition holds (usually the power threshold), we can still recover the angles of departure and produce a rough position estimate.

Beam-mispointing ripples. Because this passive RIS steers only in discrete 5° steps, the UE will not always be centered on the boresight. As it drifts within each 5° sector, the angular misalignment grows from 0° (centre) to ±2.5° (edge), halving the RIS gain at the sector boundary. These periodic gain dips produce oscillations which are not observable in Fig. 6.11. Finer steering would flatten these ripples and produce uniformly low error.

Error Decomposition Along Each Axis

Figure 6.12 juxtaposes the three surfaces.

***X*-axis (azimuth and elevation-dominated).** The second largest contributor to total error.

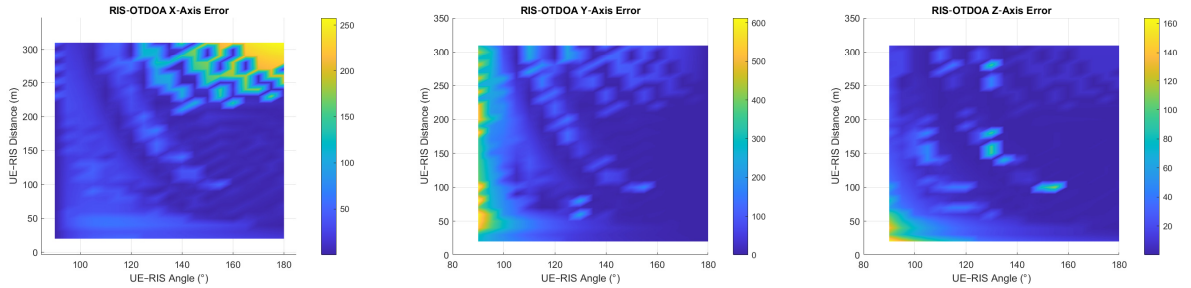

(a) X-axis error (b) Y-axis error (c) Z-axis error

Figure 6.12: Axis-wise positioning errors for the RIS scheme.

The error comes mainly by the gNB masking the RIS signal and thus not making viable the correct delay estimation.

Y-axis. Follows a similar ripple pattern but with amplitudes higher than in X and the worst error can be seen close to the 90^{o}, that is because in that place the Distance difference is the most difficult point to estimate.

Z-axis. Stays the lowest across the entire grid, thanks to the fine (log-spaced) elevation sweep and parabolic.

Histogram of positioning error

To translate the raw error maps into an intuitive quality metric, each estimate is binned into two histograms.

Figure 6.13 displays the number of occurrences for each error bracket, for the total 3-D error and for the individual X, Y, and Z components, the greater histogram will have a 25 meter step .

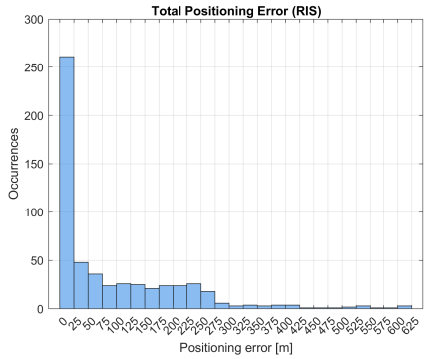

(a) Total 3-D error

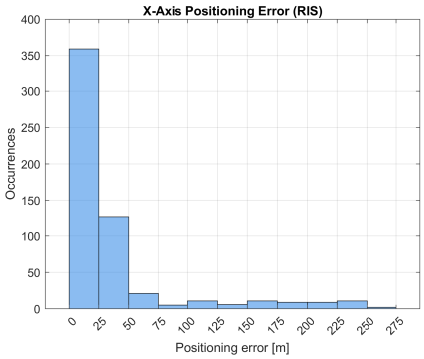

(b) X-axis error

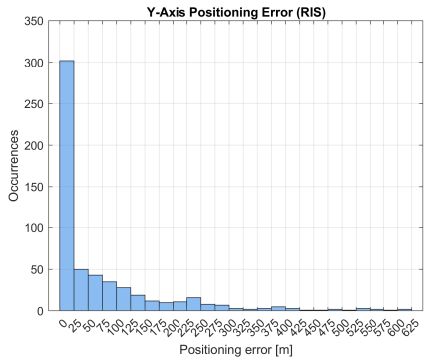

(c) Y-axis error

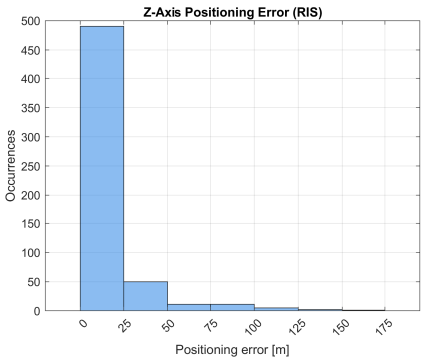

(d) Z-axis error

Figure 6.13: Number of estimates in each error bracket for total 3-D error and for the individual Cartesian axes.

As shown in Figure 6.14, focusing on the low-error estimates (under 50 m):

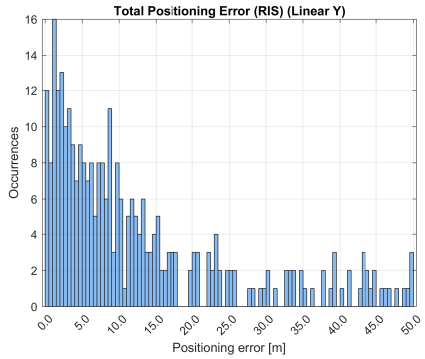

(a) Total 3-D error

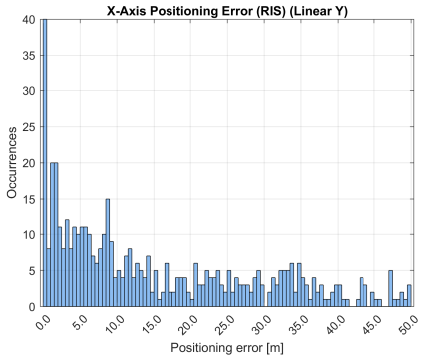

(b) X-axis error

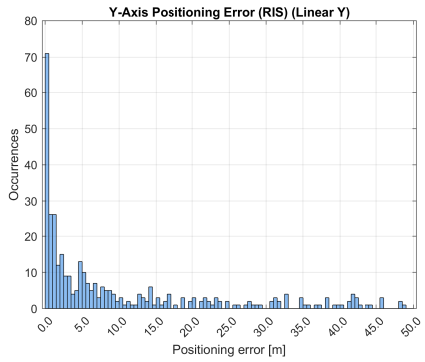

(c) Y-axis error

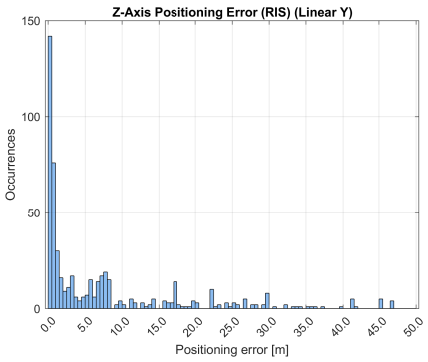

(d) Z-axis error

Figure 6.14: Number of estimates in each 0–50 m error bracket for total 3-D error and the individual Cartesian axes, focusing on the low-error (under 50 m) estimates.

Overall accuracy (Fig. 6.13a). Less than **35 %** of all estimates fall below 10 m, an order-of-magnitude improvement over the baseline gNB-only case.

X- and Y-axes (Figs. 6.13b, 6.13c). Roughly **40 %** of horizontal estimates are bellow 10 meter accuracy; the remainder are almost over 50 meters.

Z-axis (Fig. 6.13d). Vertical localization is even tighter: almost **75 %** of samples are within 10 m and practically 20 percent exceed 40 m, confirming the effectiveness of the elevation accuracy. These error results can be understood using the previously developed theory . The largest errors appear along the Y axis. This occurs because, whenever the RIS-reflected signal falls below the direct gNB signal, the algorithm arbitrarily selects a departure angle, which can be $\phi = 180°$ ($\alpha = 0°$). Such a choice can introduce an angular estimation error of up to

$$\Delta\hat{\phi} \approx 90°. \tag{6.25}$$

By contrast, the errors in the X and Z axes are governed mainly by the elevation angle, θ, which is sampled more densely from $-30°$ to approximately $-1.85°$ over 30 discrete steps. Because these elevation angles are within a narrower range, the worst-case estimation error in θ

approaches

$$\Delta\hat{\theta} \approx 28.15^{\circ}, \tag{6.26}$$

Consequently, the Y–axis suffers the greatest average error, while the X axis remain relatively more accurate and Z remains the most accurate.

6.3.3 Performance Comparison and Practical Considerations

In the gNB setup, azimuth estimates remain accurate but elevation errors are elevated, driving total position errors into the hundreds of meters (see Fig. 6.9). By contrast, our RIS-assisted 3D positioning achieves sub-10 m accuracy, although over a more confined angular section. The coverage gain is limited by the current surface directivity and signal strength, the RIS clearly overcomes the elevation ambiguity that hinders the baseline case. This setup cuts the overall error by a factor of seven, decreasing the mean 3-D positioning error from roughly 750 m to about 110 m.

6.4 RIS Strategic Placement

In this section, we will evaluate a different RIS deployment strategy, targeting spots where the direct gNB signal suffers heavy blockage or attenuation. By placing the RIS in these affected areas, we will evaluate how much the reflected path can benefit in coverage and positioning accuracy under these tougher conditions.

6.4.1 Sensitivity to Obstructions and Strategic Placement

Our previous simulations assume free-space propagation between gNB, RIS, and UE. In a real urban environment, however, obstacles such as trees or buildings can introduce an additional 10 dB (or more) of attenuation on the direct gNB-UE path. If a RIS is installed in such a shadowed zone, two competing effects arise:

The direct-path SNR from the gNB to UE would drop by 10 dB, raising the RIS detection threshold and potentially shrinking the low-error region. Not only would be this almost a perfect scenario to use it, but for example in our previous case, it would fit perfectly, because the longer the signal travels, the higher the gNB's signal amplitude becomes, and the lower the RIS's becomes.
Simultaneously, the gNB-RIS link may remain unobstructed, preserving the reflected SNR gain and compensating for the UE's poor direct coverage.

To understand how urban clutter affects our RIS-assisted OTDOA performance, we introduce a 10 dB amplitude attenuation on the direct gNB-UE link in the simulation. Imagine deploying the RIS in Barcelona's Eixample district say, along Passeig de Gràcia where tall residential and office buildings line the avenue. By mounting both the RIS and gNB high above the rooftops, we ensure their line-of-sight remains clear, but the UE operating at street level suffers an extra 10 dB of building penetration loss on the direct path.

Figure 6.15 depicts this scenario: although the gNB-RIS leg stays virtually unchanged, the gNB-UE signal is weakened by foliage and walls. In our simulation, this selective degradation causes the RIS-reflected path to dominate in regions where direct coverage would otherwise fall below the detection threshold. As a result, the RIS not only extends the usable OTDOA coverage into deep urban canyons but also recovers localization accuracy that would be lost under pure line-of-sight assumptions.

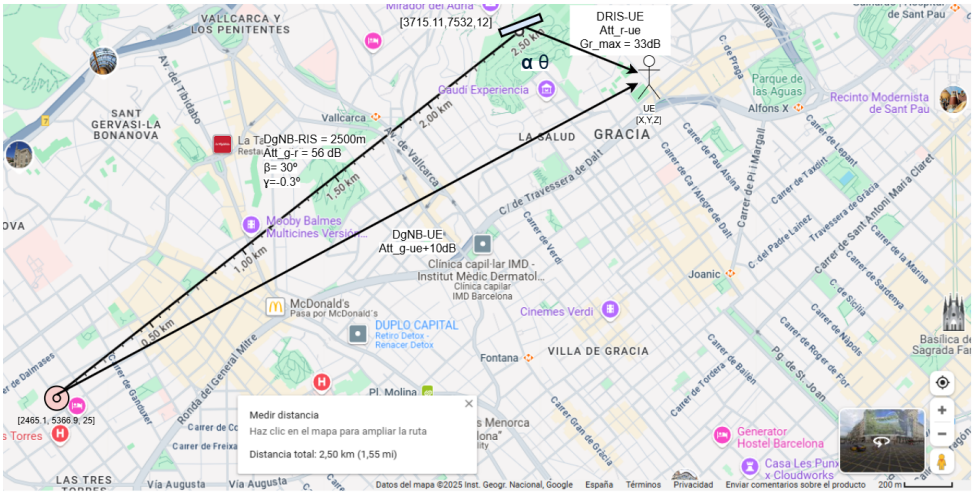

Figure 6.15: Urban deployment scenario. Adapted from [10]

Let the geometrical simulation parameters be the same as the previous simulation.

6.4.2 RIS Results from a Strategic Placement

To fully characterize the positioning performance, we will evaluate the total three-dimensional error and its X, Y, and Z components. Figure 6.16 visualizes these four surfaces over the 180°-90° azimuth sweep and 20-310 m range:

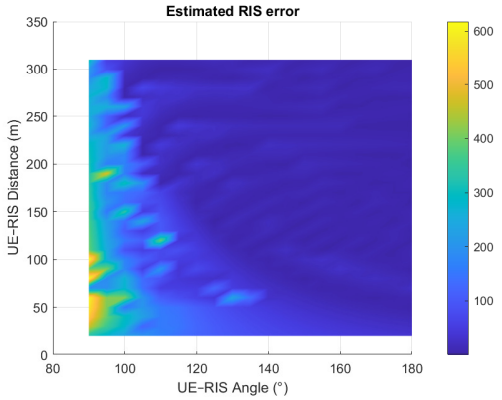

(a) Total 3-D error

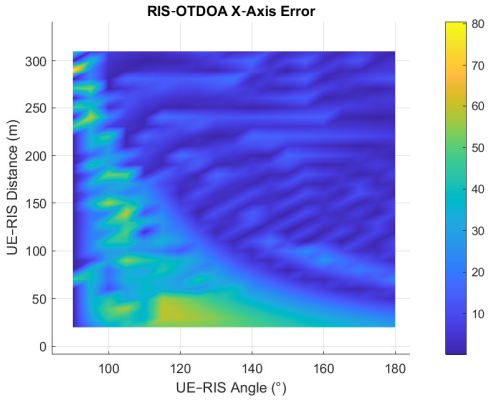

(b) X-axis error

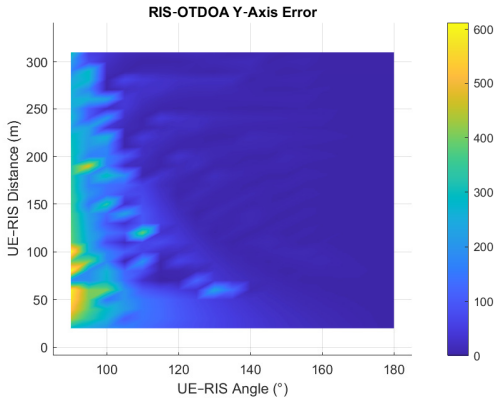

(c) Y-axis error

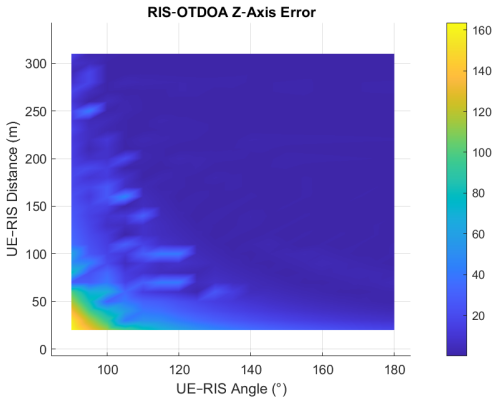

(d) Z-axis error

Figure 6.16: Fraction of estimates in each error bracket for total 3-D error and for the individual Cartesian axes.

As seen in Fig. 6.16a, the total error remains below 10 m across an expanded sector compared to the free-space case, illustrating that a strategically placed RIS can maintain 10-meter level accuracy even in a shadowed urban canyon. Breaking this down:

X-axis error (Fig. 6.16b): Dominated by residual delay difference error, this error peaks at the threshold boundaries we previously defined before.

Y-axis error (Fig. 6.16c): Follows a similar pattern as previously but with lower magnitude, since horizontal geometry along this axis is still contributing to total range error.

Z-axis error (Fig. 6.16d): Consistently under 1 m, reflecting the tight control afforded by our elevation sweep.

This component-level breakdown confirms that horizontal steering resolution is the primary limiter of accuracy, while vertical errors remain well bounded by design.

Histogram of positioning error

Figure 6.17 displays the number of occurrences for each error value, for the total 3-D error and for the individual X, Y, and Z components.

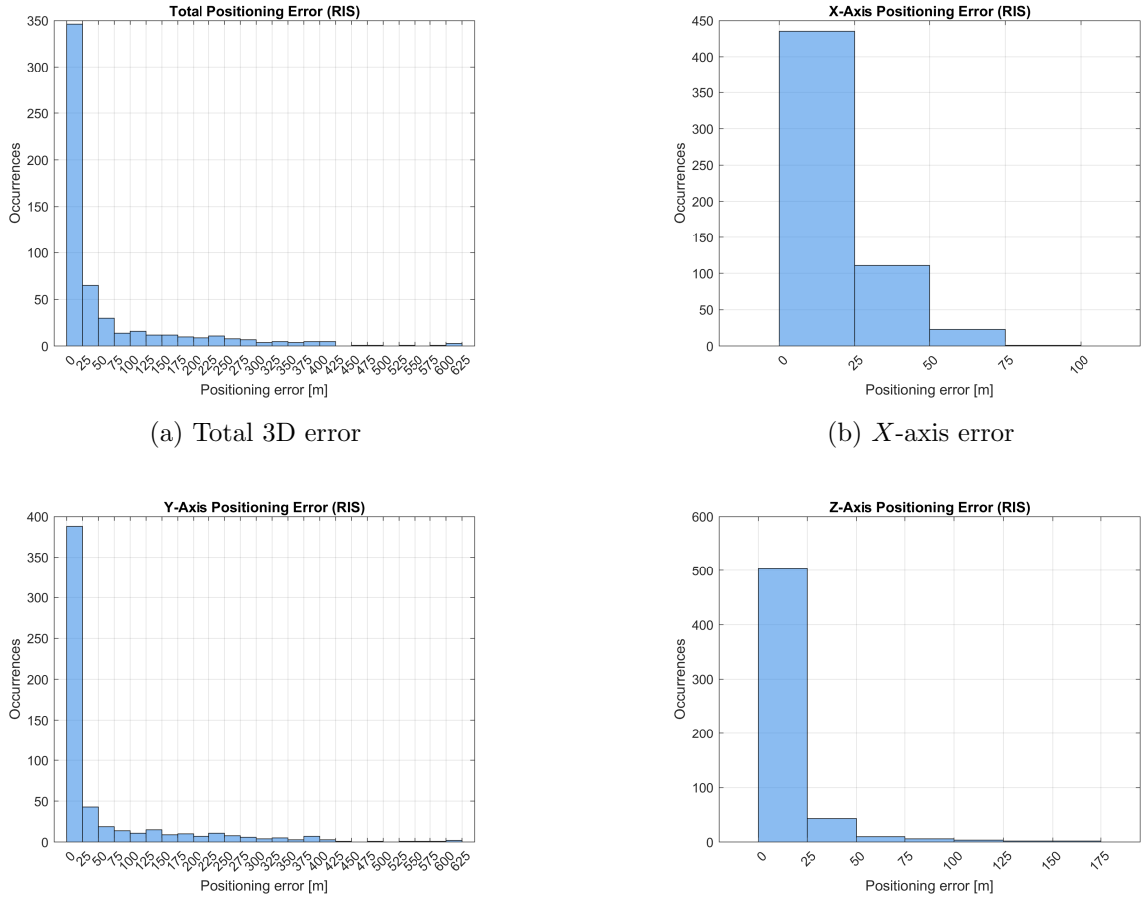

(a) Total 3D error

(b) X-axis error

(c) Y-axis error

(d) Z-axis error

Figure 6.17: Number of positioning estimates in each error category for (a) total 3D error, (b) X-error, (c) Y-error, and (d) Z-error.

As shown in Figure 6.18, focusing on the low-error estimates (under 50 m):

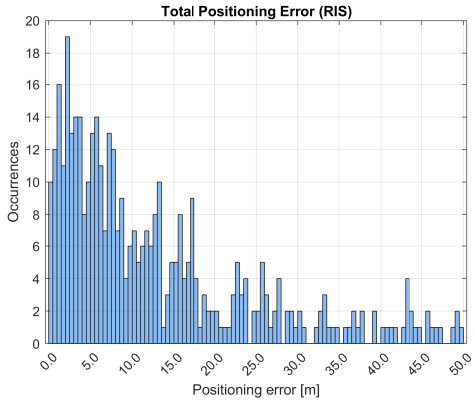

(a) Total 3D error

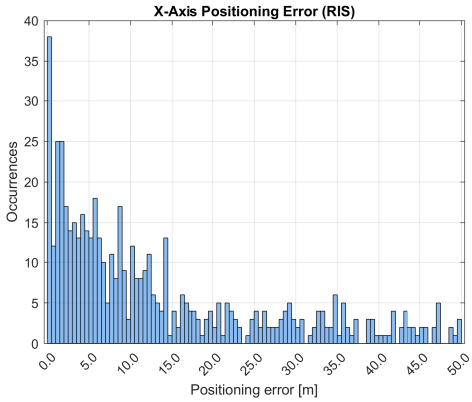

(b) X-axis error

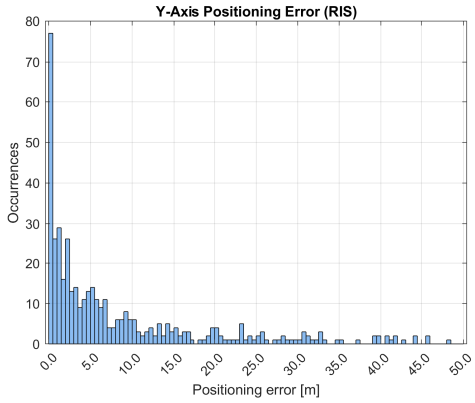

(c) Y-axis error

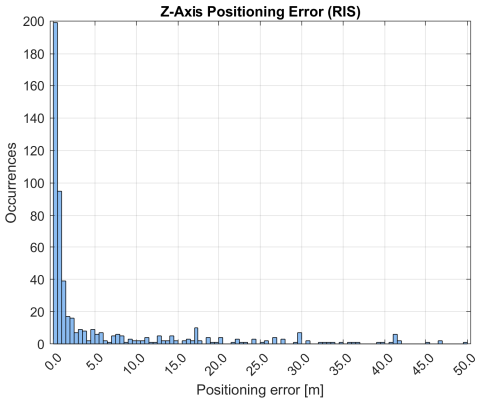

(d) Z-axis error

Figure 6.18: Distribution of positioning estimates in each error category for samples with error under 50 m (a) total 3D error, (b) X-error, (c) Y-error, and (d) Z-error.

From Figure 6.17a, we see that almost forty percent of all samples now are under the 10 m error, with fewer than 30 percent exceeding 40 m. The component plots tell a similar story:

X-axis (Fig. 6.17b): Nearly 55 percent of estimates have error below 10 m, and there is no longer error higher than 100 m .

Y-axis (Fig. 6.17c): Over 50 percent of samples achieve sub-10 m accuracy, and less than 30 percent fall above 40 m.

Z-axis (Fig. 6.17d): Almost 80 percent of estimates are within 10 m, reflecting the strong elevation resolution of our RIS-assisted scheme.

With the direct gNB path attenuated, many locations that previously did lay beyond the power budget can now be served purely through the RIS reflection, no extra elements neither additional beam sweeps were needed. The new placement and relaxed power threshold push more samples into the sub-10 meter error range, a clear step forward over our earlier RIS configuration.

That said, the metric paints an optimistic picture: if the user drifts outside the RIS's main beam lobe, the reflected signal may fall below the power threshold and the true positioning error could rise, an effect our current evaluation does not capture. This configuration nearly halves the overall error (From a mean 3D error of 110m to 60m), underscoring the substantial performance gain it delivers without the need of additional hardware.

6.4.3 RIS Size Optimization and strategic sweep

This section will focus on the overall worst-case positioning error. We will evaluate multiple RIS sizes while reducing the scenario azimuth scan to the half RIS sweep step, where the UE sits furthest from the main beam. This targeted approach will reveal the element number that minimizes peak error. Furthermore, angular sectors already known to produce large errors will be omitted (90°–125°) due to geometric constraints and in order to reduce the azimuth sweep number.

Up to this point we have used a 50×50-element surface ($2.5\text{ m} \times 2.5\text{ m}$ at $\lambda/2 = 0.05\text{ m}$ spacing), which balances array gain and beamwidth. But what happens if we quadruple the aperture to 100×100 elements? At first glance a stronger RIS signal seems unambiguously helpful, yet two practical issues emerge:

gNB masking. A four times larger array boosts the reflected path by 6 dB. If that boost drives the RIS peak far above the gNB peak, the direct-path information can be "buried," reversing the masking problem we solved earlier.
Beam-scanning overhead. Doubling each linear dimension halves the beam-width, so the azimuth sweep now requires roughly twice as many steering angles to cover the same sector. More steps mean longer scan times and higher control overhead, not to mention increased hardware cost.

Larger is not always better, beyond a certain aperture, the RIS begins to dominate the link power and reduces the geometric diversity needed for OTDOA. An intermediate size large enough for strong reflections but small enough to maintain a $3-5^\circ$ beamwidth should strike the best balance between gain, coverage, and cost.
Thus, the error figures derived in the previous section are correct only when the UE happens to lie exactly on one of the azimuth steering directions. In reality, however, the terminal can sit anywhere inside the sweep interval

$$\phi \in \left[\phi_0 - \tfrac{\Delta_\phi}{2},\ \phi_0 + \tfrac{\Delta_\phi}{2}\right], \qquad \Delta_\phi = 5^\circ\ (\pm 2.5^\circ). \tag{6.27}$$

If the RIS main beam is not perfectly aligned with the UE, the effective gain drops and the

localization error grows.

To quantify this effect we tightened the sweep to the sector 180° → 130° and kept the radial range of 20–310 m. The next figure 6.19represents the scenario: Yellow circles mark the UE test points placed at the step and half-step borders, while the dashed outlines indicate how consecutive steer directions overlap to guarantee continuous coverage.

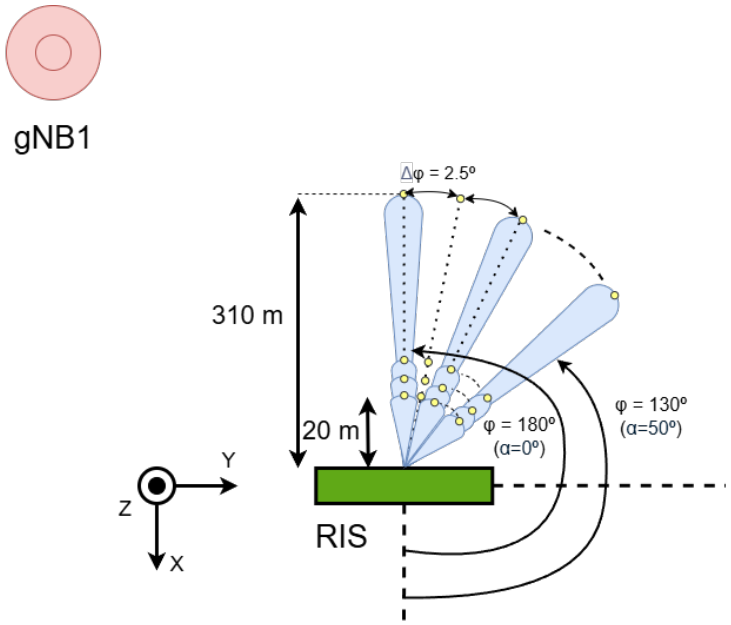

Figure 6.19: Schematic of the azimuth sweep with a half-step resolution ($\Delta_\phi = 2.5°$). Each shaded sector represents one RIS beam; yellow dots denote UE locations used to evaluate the localization error at the borders of neighbouring beams.

The results are shown in Figure 6.20 (3-D error map) and Figure 6.21 (error histogram):

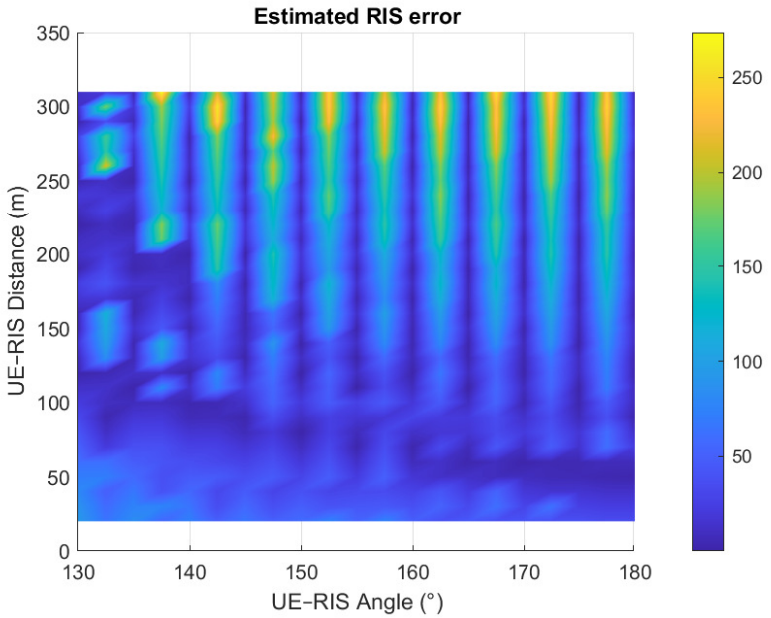

Figure 6.20: 3-D localization error when the UE is allowed to fall anywhere within the ±2.5° azimuth half-step. The error rise at mid-sweep angles is clearly visible.

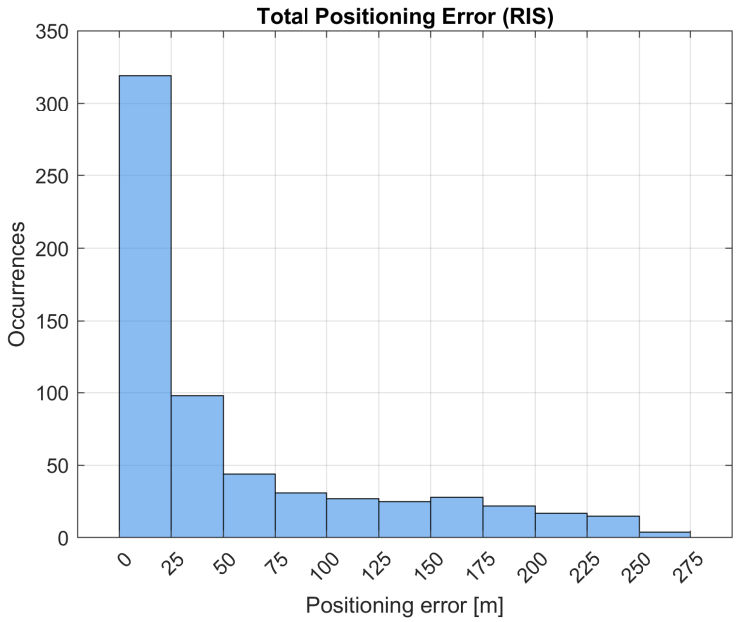

Figure 6.21: Histogram of 3-D error when the UE is allowed to fall within the ±2.5° azimuth half-step.

Central region: Mid-sweep points, which are displaced by up to 2.5° from the nearest steering direction, exhibit a noticeable error ridge in the 3-D map.

Histogram tail: The fraction of samples with errors from 50 m to 275 m grows dramatically. This tail corresponds to locations where the RIS azimuth array factor hits a null, an unavoidable consequence of the present element count.
Mean error at the border: Even in zones where the theoretical model predicted low error, the average error is 56 m because the UE falls in between two beams rather than on the beam center, still lower than the previous 60 meters, but in a zone where the error should be lower.

These observations highlight an important trade-off:

Unless we narrow the azimuth scanning step or modify the array to smooth out its nulls, by adding more elements or tweaking their spacing, users near the sweep's edges can see positioning errors up to ten times larger than the ideal aligned-beam predictions. As discussed in Section 6.2.3, this degradation is a product from the azimuth array's element number and the resulting nulls angular distance. In the next section, we will dive into how these array-induced effects arise and explore strategies to mitigate them.

6.4.4 Optimal Trade-Off Between RIS Size and Positioning Error

Intuitively, enlarging the RIS aperture should always lower the positioning error: a larger surface provides more array gain, so the RIS peak rises toward the level of the gNB peak and the OTDOA geometry improves.
In practice, however, incrementing the number of elements reduces the beam width, so is more difficult to locate Users that are not exactly in the beam direction. To identify the sweet spot for our beam step ($\Delta_\phi = 5°$), we sweep the aperture from 27×27 elements up to 85×85 elements in steps of two elements per side ($N_{\text{iter}} = 30$) and record the 3-D error for each case.

Rather than exhaustively sweeping every position of the scenario, which can be computationally expensive we will point to 3×3 positions around the RIS beam direction. To identify the optimal RIS aperture in a realistic setting, we place the UE at the boundary points of the ±2.5° sweep (shaded ocean blue in Figure 6.22) and evaluate which aperture orientation proportions the best performance. Specifically:

Azimuth angles: we test three steering directions within the coverage window157.5°, 160°, and 162.5° so that the two edge cases (157.5° and 162.5°) lie exactly on the sweep borders and the center angle (160°) samples the midpoint.
Radial distances: we place the UE at three radial 165 m, 170 m, and 175 meters from the RIS center, which correspond to the inner, central, and outer rings of the coverage area.

By measuring the 3-D error at each combination of azimuth and distance, we can determine which RIS beam orientation and range maximizes performance. In other words, the true "best" aperture is the one whose steering angle and path length produce the highest gain across these boundary test points.

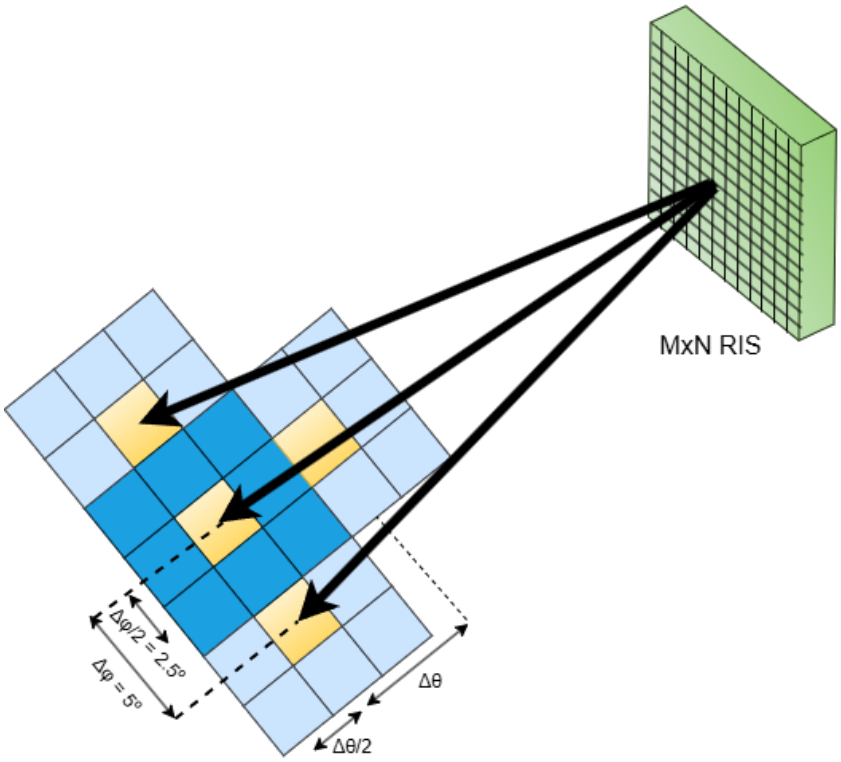

Figure 6.22: RIS sweep optimization scenario: UE positions (ocean blue) at the edges of a ±2.5° azimuth sweep, and three radial distances (165 m, 170 m, 172.5 m).

The plot idea is similar to the previous scenario, the yellow squares represent where the RIS it is actually sweeping. The result for each point is plotted in Fig. 6.23 and the total result is proportioned in Fig. 6.24.

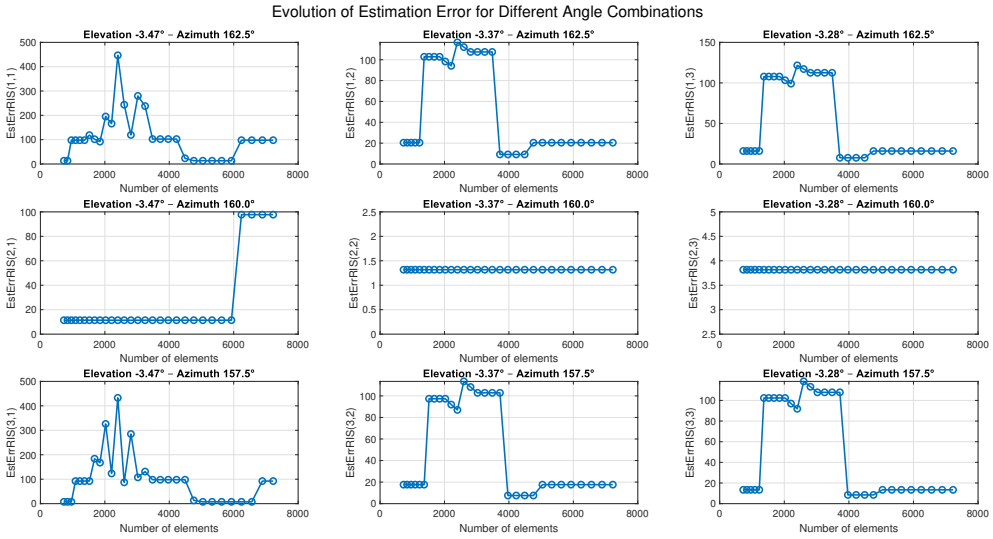

Figure 6.23: Evolution of Estimation Error for Different Angle Combinations and RIS sizes

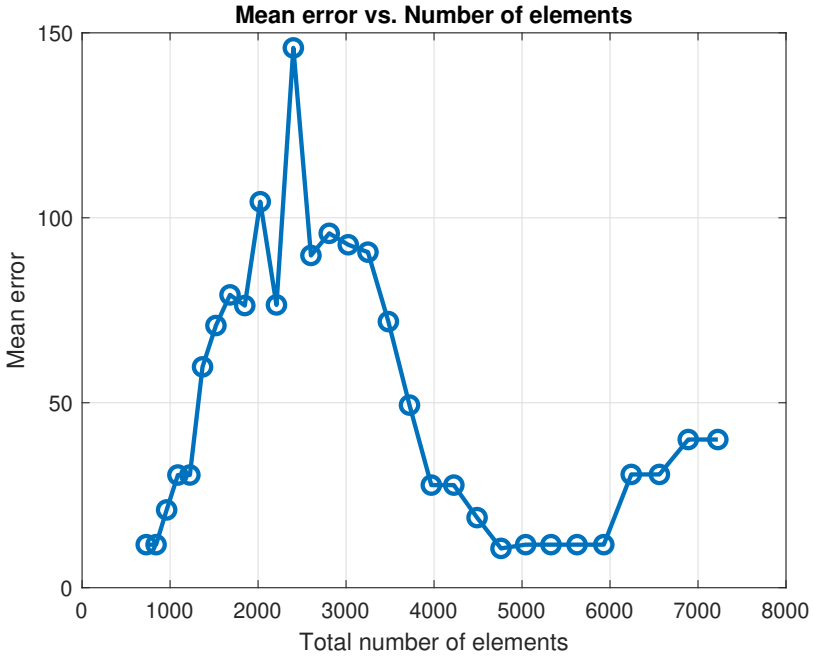

Figure 6.24: Mean 3-D positioning error in our cell versus total number of RIS elements.

Both Figure 6.24 (mean error vs. number of elements) and the detailed subplots in Figure 6.23 exhibit a clear, multi-stage dependence of the estimation error on the total RIS size:

Initial valley (27x27 to 29×29 elements). At first the Error is quite Low, the reason is because the RIS array factor is very wide and the angle falls near the main lobe max.

Rapid increase (31×31 to 49×49 elements). Doubling the array in both azimuth and elevation narrows the main lobe and increases its peak gain. Around a 50×50 configuration, the first null of the array factor moves toward boresight, "pinching" the beam and causing the error to spike sharply.

Peak and early decline (49×49 to 69×69). Once that null crosses the target direction, further element additions shift the sidelobes outward. The main lobe realigns with the coverage zone and the error rapidly falls.

Stable low-error plateau (69×69 to 77×77). In this range, the main beam consistently covers the intended angles. Both azimuth and elevation patterns settle into a well-behaved shape, driving the mean error to its minimum.

Secondary rise at very large sizes (> 77×77). Beyond a certain array size the azimuthal pattern develops new sidelobe structure near the scan edges, which elevates the error again. The elevation pattern remains close to its main lobe, almost always overlaps the target window, but the late-stage degradation is driven almost entirely by elevation side lobes, it can be seen in the $(\theta = -3.47, \phi = 160)$ case, the azimuth beam is steering directly to the UE but the elevation is not, so that increase in error reveals the elevation zero.

The RIS beam's array factor behaviour when increasing the number of elements is depicted in Fig. 6.25. As the number of elements increases, the main lobe becomes progressively narrower and the side-lobes shift outward, demonstrating the higher directivity achieved with larger arrays.

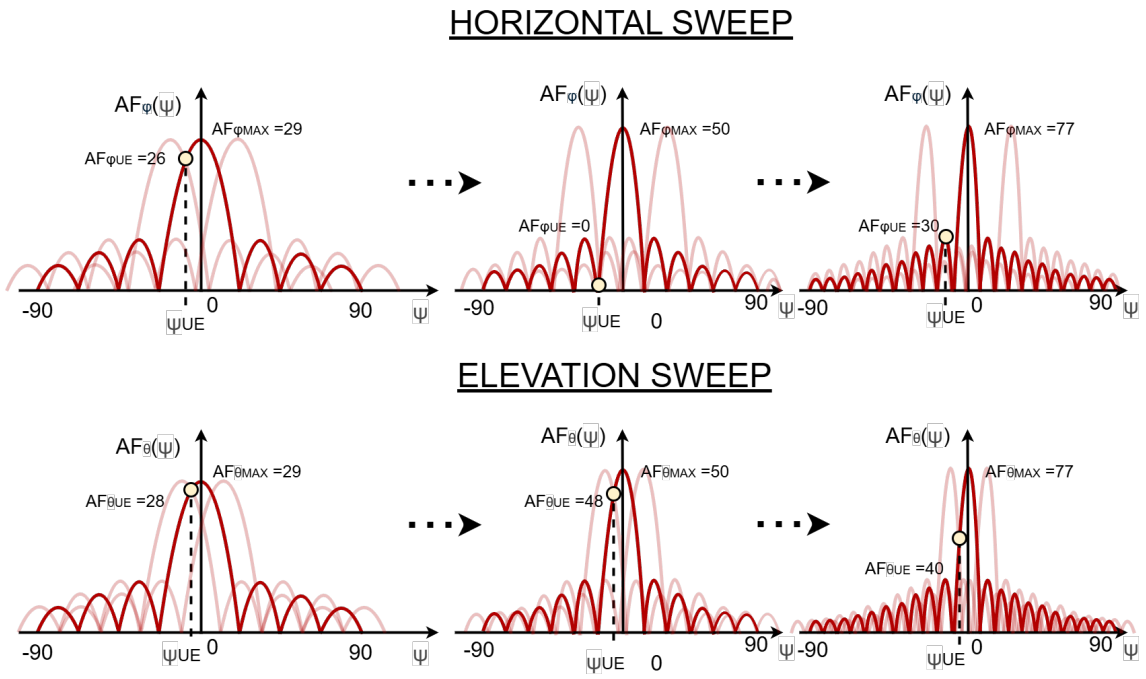

Figure 6.25: RIS array-factor example evolution: additional elements sharpen the main lobe and push the side-lobes toward the diagram edges. The more opaque Array Factors represent the beam steered in the adjacent sweep step.

Corner positions ($\phi = 162.5°$, $\theta \approx -3.3°$ and $\phi = 157.5°$): At these edge-of-beam angles, the received RIS gain is lowest, so the estimation error reaches its maximum. In particular, for $\phi = 162.5°$ the error curve shoots up sharply around 2 500–3 000 elements, precisely where the array's first null encroaches on the target direction, before falling into a stable, low-error plateau once it arrives to a secondary lobe. The $\phi = 157.5°$ trace follows the same trend, but with its inflection points shifted slightly in the element count due to the minor change in steering angle.

Central position ($\phi = 160°$): When the RIS steers its beam in azimuth directly toward $\phi = 160°$, the main lobe always centers on the UE. As a result, the estimation remains accurate (near–zero error) for almost every array size. The only notable exception occurs at around 6 000 elements, where a brief spike appears. This spike is solely due to the elevation array factor momentarily dropping into a side-lobe (or passing through a null), reducing the elevation gain below its peak.

Elevation "safety net": Even at the corner azimuths, the RIS elevation pattern is sampled so finely (30 logarithmic steps over $-30°$ to $-1.85°$) that its gain remains almost at 80 % of the maximum. This high elevation gain "rescues" the estimation whenever the azimuthal array factor momentarily degrades, hence why after the initial spike the error still falls into a low plateau for all three curves.

The sweep analysis reveals two competing "sweet spots" for localisation. A 77×77 aperture delivers the narrowest, best-aligned main lobe, its first side-lobe conveniently fills the angular gap left by the tight beam so that coverage remains continuous. A leaner 29×29 array, on the other hand, keeps the main lobe wide enough to overlap adjacent steer directions without relying on side-lobes, achieving almost the same accuracy in that scenario with far fewer elements.

To highlight the trade-off we plot both configurations side by side. The larger surface (77×77) is summarised in Figs. 6.26a–6.26b, whereas Figs. 6.26c–6.26d show the corresponding results for the 29×29 case.

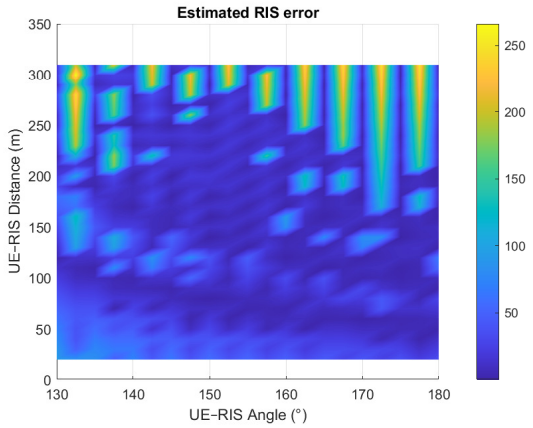

(a) 3-D error map, 77×77 elements

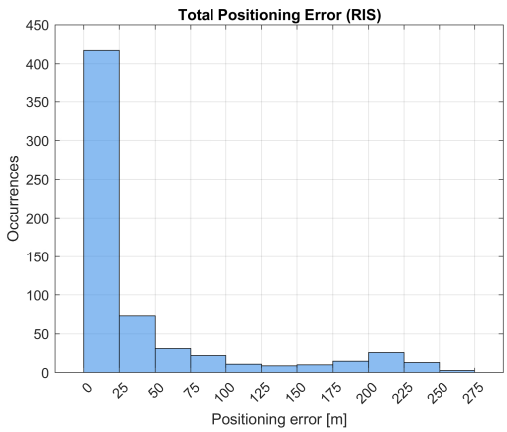

(b) Error histogram, 77×77 elements

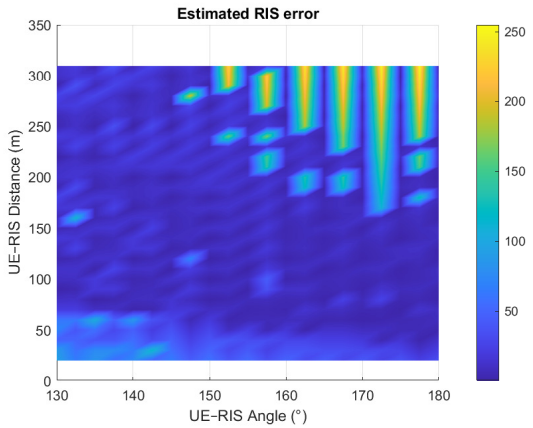

(c) 3-D error map, 29×29 elements

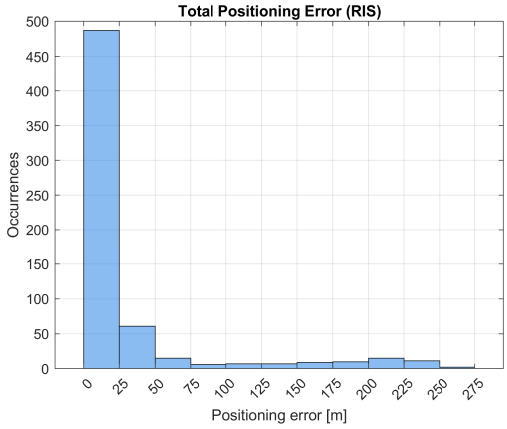

(d) Error histogram, 29×29 elements

Figure 6.26: Comparison of localisation performance for the two candidate RIS apertures. The larger 77×77 surface achieves the highest worst-case error by exploiting its first side-lobe, whereas the leaner 29×29 array achieves the lower error using a broader main lobe to maintain coverage with far fewer elements.

With 29×29 elements the main lobe stays wide enough to overlap neighbouring steer direc-

tions, so the entire left-hand sector remains within high-gain coverage. In contrast, the 77×77 surface would have to rely on its first side-lobe to illuminate the same region, an approach neither power-efficient nor robust against small steering errors. Hence the 29×29 array, which satisfies the 5° step while keeping the UE inside its primary beam, stands out as the more practical choice. The positioning error difference is from 46 m with the 77×77 element array to 30 m when using a 29×29 array, a 33 percent difference.

6.4.5 Updated sweep strategy with the 29×29 RIS

After settling on the 29×29 aperture, we re-optimized the search grid to minimize the total error while keeping the update cycle and preserving angular resolution. In this section we will evaluate what happens when the sweep step is closed a bit.

Range window. The sweep now starts at $R_{\min} = 80$ m and extends to $R_{\max} = 310$ m; points closer than 80 m are covered almost isotropically by the broad main lobe and therefore need no fine scan.

Azimuth step. The steering increment is relaxed slightly from $\Delta_\phi = 5°$ to $\Delta_\phi = 4°$. Because the main lobe of the 29×29 array is wider than that of the 77×77 panel, the 4° grid still guarantees overlap between adjacent beams throughout the new range window.

Sweep count. With 24 elevation directions in range (80 : 20 : 310 m) and 13 azimuth directions (180° : − 4° : 130°) the total number of beam positions becomes

$$N_{\text{sweeps}} \;=\; 13 \times 24 \;=\; 312, \tag{6.28}$$

practically identical to the original $10 \times 30 = 300$ combinations. Thus we retain the numeric value of the larger grid while benefiting from a shorter radial span and a beam width that is naturally matched to the 29×29 aperture.

Figures 6.27a and 6.27b display the localisation performance of the re-tuned 29×29 RIS. The impact of the new grid is immediate: the 3-D error surface has lost the high-error ridges visible in the previous configuration, and the histogram shows that nearly every estimate now falls within the first two bins. The improvement is not accidental. By restricting the radial sweep to 80–310 m and steering only every 4°, we point exactly those directions in which the error was already known to be low; the algorithm no longer wastes time on points that are geometrically unfavorable. In effect, the search starts closer to the "sweet spot" for every UE.

A marginal gain could still be obtained by tightening the azimuth step to 3.5° (adding 24 beams), which would shave a few metres off the long-tail of the histogram. Yet the present layout offers the best overall trade-off: it keeps hardware cost low, limits computation to 312

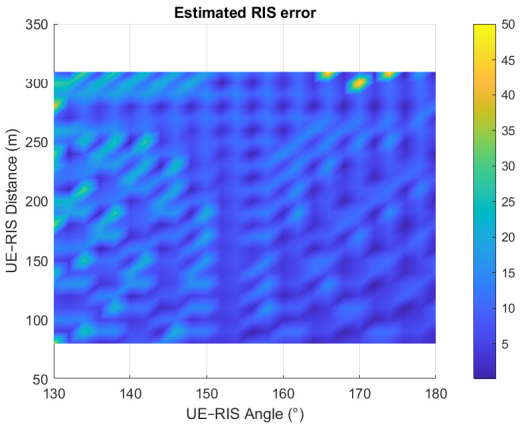

(a) 3-D error map, optimised grid (with a 50m cap)

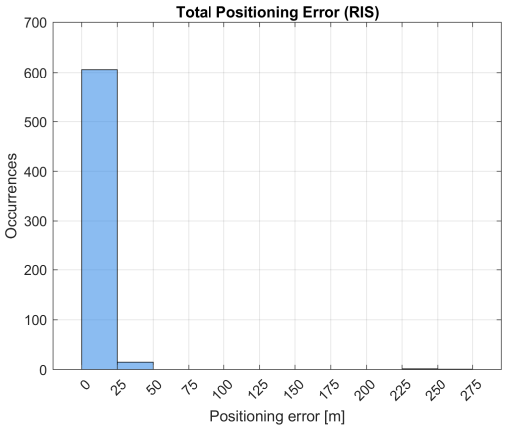

(b) Error histogram, optimised grid

Figure 6.27: Localisation results for the optimised 29×29 RIS. The focused sweep eliminates the high-error regions present in earlier trials and concentrates almost all estimates below the 20 m mark.

beam positions, and already drives the worst-case error well below the original targets, the price to pay is a lower area coverage.

Not only does our method achieve minimal estimation error, but it also aligns closely with real-world conditions. From [21], the far-field or Fraunhofer region begins once the radiation pattern does not vary with distance. For our 29×29 RIS with element spacing $d = \lambda/2$, the array aperture is

$$D = (N_y - 1)\, d = (29 - 1) \times \frac{\lambda}{2} = 1.40 \text{ m}. \tag{6.29}$$

Therefore, the Fraunhofer distance is

$$R_{\text{FF}} \; > \; \frac{2D^2}{\lambda} = \frac{2\,(1.40)^2}{\lambda} \approx 39.2 \text{ m}. \tag{6.30}$$

In the far-field region, all array elements lie at essentially the same range R from the observation point, so their individual phase and amplitude variations collapse into a common term $\frac{e^{-jkR}}{R}$. Under these conditions, the Array Factor alone, considering an isotropic element, defines the angular shape of the radiation pattern. In this scenario, the Fraunhofer criteria is met, so that our model operates entirely within the far-field regime, making it valid to use the array factor directly as the radiation pattern. This guarantees that our simulated beamforming and positioning results accurately reflect the performance of a real RIS deployment. A 50×50 RIS would have a Fraunhofer distance of $\approx 120m$, causing half of the scenario estimation to fall into the Fresnel zone [21], which would need another type of estimation.

6.4.6 RIS Deployment vs gNB deployment

In this subsection it is evaluated the real computational and monetary cost of deploying each scenario. From [33], we can estimate the cost of deploying a 5G ground base station, in a big city with our scenario characteristics, will be around $100k$\$ or approximately 91k€ (euros). Unfortunately, there is not so much information about RIS deployment cost, but as a matter of fact it is widely stated that it is cost-effective[5].
Table 6.2 condenses the outcome of all localization runs under every deployment strategy considered.

The headline figure of ~ 750 m for the mean 3-D error is dominated by the vertical axis, where the three terrestrial gNBs provide almost no elevation diversity. In azimuth, however, the same geometry delivers an accuracy on the order of four metres. In other words, the gNB-only network is highly precise in the horizontal plane but suffers from a height ambiguity that inflates the 3-D RMS statistic.

The three-gNB constellation blankets a service area far larger than that of a single RIS. Comparing absolute 3-D errors therefore understates the gNB's "error-per-square-metre" advantage: the RIS achieves lower numerical errors, but only within a limited sector and range, whereas the gNB infrastructure maintains service, and acceptable azimuth precision, over a substantially wider region.

Consequently, while the RIS-enhanced scenarios are better at point accuracy inside their intended coverage wedge, the 3-gNB baseline (in reality 5) offers broader availability and superior horizontal precision.
In Table 6.2 the label "(WCP)" indicates that the UE was evaluated at the midpoint between two successive azimuth steer directions, that is, at $\pm\frac{\Delta_\phi}{2}$ from the main beam direction. Placing the user at this half-step offset represents the worst-case position (WCP) within the sweep and, therefore, provides an upper bound on the localization error.

Table 6.2: CAPEX, accuracy and run-time for the main deployment options

Scenario	**CAPEX (EUR)**	**Mean 3-D Error (m)**	**Run-time**[†]
3-gNB (baseline)	$\sim$ 273 k	$\sim$ 750	1×
RIS, normal placement (50×50)	\$	$\sim$ 110	120×
RIS, strategic placement (50×50)	\$	$\sim$ 60	120×
RIS, strat. placement + strat. sweep (WCP) (50×50)	\$	$\sim$ 56	60×
RIS, strat. placement + strat. sweep + optim. elems (WCP) (29×29)	\$	$\sim$ 30	60×
RIS, strat. placement + fully optimized(elements, sweeps)(WCP) (29×29)	\$	$\sim$ 10	62.4×

[†]Run-time normalised to the gNB-only post-processing time (How many correlations are needed, being 5 for the 3-gNB case). The increase is driven mainly by finer azimuth/elevation sweeps as the RIS beam narrows.

6.4.7 Limitations and Challenges

After properly analyzing the results, there are some key aspects that arise that mainly hinder the proper localization estimation:

Azimuth step: The steering step Δ_ϕ is the most limiting factor when the goal is to cover a wide service area with a single RIS. A coarse step (e.g. 5°) keeps the sweep short and the run-time modest, yet leaves sizable gaps between adjacent beams once the range is high. Conversely, shrinking the step to 2.5° or below closes those gaps and decreases the worst-case error, but doubles the number of steer directions and therefore the computational burden. In practice, a balance must be made between coverage continuity against sweep duration: pushing Δ_ϕ too low yields excellent accuracy but risks an impractically long update cycle.

PRS and estimation time: The problem is compounded by the nature of the positioning reference signal itself. The NR-PRS can be a periodic but is not always-on symbol, it is scheduled sparsely so that regular traffic can occupy the remaining resource elements. If the RIS needs dozens of azimuth–elevation combinations to complete a fine sweep, many PRS occasions must be reserved, lengthening the estimation window and encroaching on data throughput. In short, higher element counts and finer angular grids improve spatial resolution but stretch the PRS schedule to the point where either data capacity suffers or timely positioning updates become impossible.

Total area coverage. With the optimized 29 × 29 surface the high-accuracy zone is the wedge shown in Fig. 6.28: about 50 degrees in azimuth and from 80 m out to roughly 310 m in range. This footprint is set by three simultaneous limits: the single-panel geometry, the beam-width dictated by the element count, and the number of PRS slots that can be allocated to the sweep. Widening the region would require either multiple RIS panels or an adaptive scan that sacrifices update rate for instantaneous span.

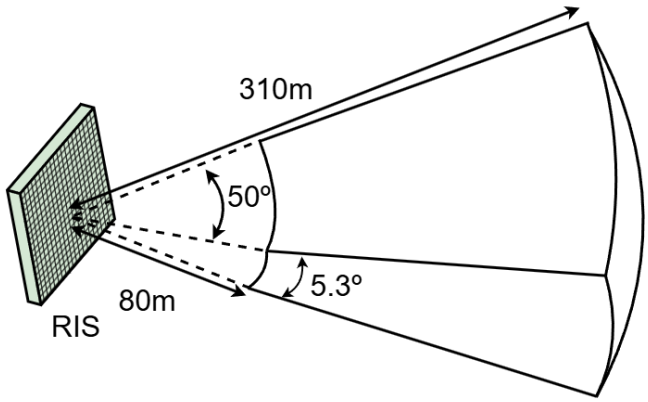

Figure 6.28: Effective localisation footprint of the single 29 × 29 RIS: a wedge spanning 50 degrees in azimuth and 80–310 m in range.

6G positioning: All of the limitations discussed above grow severely as we push the carrier into the upper–mmWave and sub-THz ranges targeted for 6G. Free–space path-loss rises with $20\log_{10}(f)$, so every tenfold increase in frequency costs 20dB of power budget. The usual counter-measure is to raise the array gain, but a higher gain is obtained by enlarging the aperture and, inevitably, narrowing the main lobe. A narrower beam means more pointing directions to cover the same field of view, hence more RIS sweeps, more PRS occasions (burst of PRS symbols), and longer update times. If the carrier-frequency plan and the RIS architecture are not co-optimized (Sub-carrier spacing, PRS period, etc), the panel will end up confined to near-field or very short-range use cases where the extra gain is not the limiting factor.

6.4.8 Mitigating the PRS scheduling constraint

With the default settings from [9] `PRSResourceSetPeriod = [10, 0]` the gNB transmits one PRS occasion every 10 slots [34]. Each occasion consists of eight OFDM symbols at 15 kHz spacing, a block that spans 1 ms. During that single millisecond the RIS must keep a fixed phase map so the UE can correlate all symbols coherently, the beam is therefore locked for the remaining 9 ms until the next PRS arrives.

Timing impact of a full sweep:
One PRS equals one effective beam every 10 ms.
Our coverage grid from the 29x29 elements case with $N_\phi \times N_\theta$ angular sweeps (13 azimuth $\times$24 elevation) means $13 \times 24 = 312$ distinct beams.
If the UE sits in the very last beam of the cycle (Worst case scenario), the total time before that User is pointed is: $312 \times 10ms \approx$ **3.12 s**.

Why three seconds matter: A 3 second update interval is acceptable for slow-moving terminals but far too sluggish for vehicular or drone applications, and it consumes PRS resources that could otherwise carry user data.

Possible solutions to the PRS problem

Given the bottleneck created by using one PRS occasion per beam, we face a big trade-off:

Shrink the sweep: reduce the azimuth range (and therefore the total area covered) so that the RIS finishes a cycle sooner.
Increase the number of RIS panels: rather than enlarging a single surface, deploy several small-footprint RIS units whose individual coverage cones overlap and jointly extend the service area.

Accept a longer update interval: keep the full sweep but tolerate several-second latency for worst-case users.
Sweep with other NR reference signals in addition to PRS.

The fourth option is the most flexible. Two candidates stand out:

SSB sweep: The Synchronization-Signal Block combines PSS (Primary Sync Signal) and SSS(Secondary Sync Signal) and is already broadcast with a beam sweep [35]. In the $\mu = 0$ numerology (15 kHz SCS, $f_c = 3$ GHz) normally four SSBs can sent in a 20 ms period, giving one beam every 5 ms, twice as fast as a 10 ms PRS cycle. Using these SSB bursts, the RIS can illuminate four azimuth directions before the next PRS appears.

CSI-RS sweep: CSI-RS is a downlink reference designed for channel-quality estimation [36]. It cannot be transmitted while using SSB [36], so if the SSB transmits the first sub-frame, this can be sent in the second sub-frame. Its periodicity is programmable to 20 ms, and each occasion can carry 2–4 symbols enough for a reliable correlation. By coupling the RIS steering to consecutive CSI-RS occasions, we can step through beams several times faster than with PRS alone.

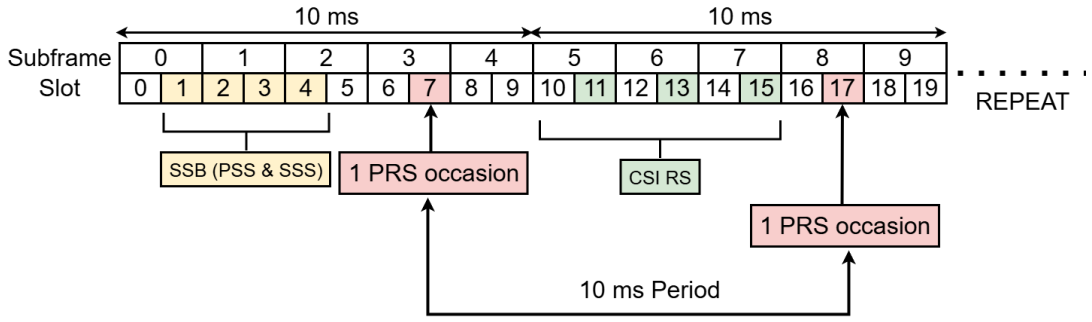

Figure 6.29: Example slot timeline (20 ms window at 15 kHz SCS).

The example of slot timeline in Fig. 6.29 is organized as follows:
SSB burst (PSS + SSS): occupies four slots (1–4), with up to four SS/PBCH blocks sent within those 5 ms each block lasting four OFDM symbols and only using part of its slot.
PRS occasions: occur every 10 ms, shown at slots 7 and 17, and in this setup each PRS fills an entire slot (12 symbols).
CSI-RS bursts: are interleaved every 5 ms at slots 11, 13 and 15 and can consist of four OFDM symbols within each slot to enable faster beam updates without occupying the full slot.

A practical strategy is therefore to keep PRS for the highest-precision time-of-arrival measurement (possibly sweeping at the longer distances where is needed more power) , while running a parallel sweep with SSB and/or CSI-RS.

The UE now listens to three reference signals each sweep cycle: up to 4 SSB bursts, three CSI-RS bursts, and one PRS occasion, for a total of 9 beam measurements every 20 ms. Thus, the effective beam-steering rate becomes

$$\frac{9 \text{ beams}}{20 \text{ ms}} = 450 \text{ beams/s}. \tag{6.31}$$

In the worst case, when the UE lies in the very last of the 312 beams, the latency before that beam is illuminated is

$$\frac{312}{450} \approx 0.69 \text{ s}. \tag{6.32}$$

This hybrid scheme cuts the worst-case finding delay by a factor of around 9 compared to PRS-only scanning. However, each CSI-RS or SSB measurement uses fewer OFDM symbols than a full PRS burst, so the correlation signal-to-noise ratio drops and distinguishing adjacent beams becomes more challenging. By simply increasing the number of azimuth sweep steps, we could boost the SNR in those critical sectors without pushing the worst-case latency above the previous 3.12 s. In other words, a finer angular grid sharpens each beam's gain and yet, even with a few more beams, the maximum wait time remains well below the original full-PRS scan.

Chapter 7

Conclusions and Future Work

7.1 Conclusions

A wireless landscape that is relentlessly moving toward higher carrier frequencies and centimeter-level localization accuracy makes RIS an indispensable enabler for 6G. This thesis has demonstrated, through theory, simulation and extensive error analysis, that a single passive RIS strategically placed halfway between a gNB and the user equipment can proportion a robust positioning system that attains almost a sub-10 m 3-D error over a medium sized area.

The main achievements of this work are summarized below:

1. **End-to-end MATLAB toolbox**. A modular framework was built that links the 5G NR PRS generator, a full-wave RIS channel, and the multi-static multilateration solver, enabling rapid what-if analyses of any RIS aperture, sweep grid and deployment geometry.

2. **Quantification of resolvability limits**. The study derived closed-form bounds for the minimum path-length difference $\Delta d_{\min} \approx 32$ m imposed by the chosen 52-RB, 15 kHz PRS waveform and the sample frequency, verified them with the simulation results. These limits dictate how close the UE can approach the RIS without losing the dual-peak signature that the algorithm exploits.

3. **Coverage extension and accuracy boost**. When the RIS steers its main lobe toward the UE, the reflected echo raises the detection flag to its maximum value, and the 3-D error surface collapses from hundreds of meters (baseline) to $<$10 m across a $50^\circ \times 290$ m.

4. **Hardware "sweet spot"**. A systematic sweep revealed that a 29×29 $\lambda/2$ array balances array gain and beam-width; smaller panels perform correctly, whereas larger and medium size ones introduce scanning overheads that again raise the mean error.

5. **Latency-aware signaling scheme**. By interleaving a coarse SSB/CSI-RS scan with high-precision PRS snapshots, the proposed timeline sustains sub-second updates without monopolizing downlink resources.

Collectively, these results prove that a passive surface costing orders of magnitude less than an additional gNB and without the need of clock synchronization can unlock meter-level 3-D localization in the very scenarios like urban canyons .

7.2 Potential applications for this RIS–assisted link

mmWave / sub-THz coverage extension Passive RIS tiles installed on façades, lamp posts or tunnel walls can steer high-frequency energy around corners and into shadowed zones where a conventional gNB signal would be blocked. A single panel, once configured, operates without an RF chain, so the incremental cost is chiefly in the surface itself and the control cable, far lower than adding an extra active base station.

Short–medium-range positioning (80–310 m): When the array geometry and the sweep step are tuned to match the desired footprint, the same passive panel can provide decimeter-level localization to users located tens or even hundreds of meters away. In this mid-range regime the beam is still wide enough to cover the target area with a modest number of beams, keeping both computation and PRS overhead within practical limits.

Multi-UE localization: Because a RIS reflects instead of retransmitting, it can serve any number of terminals within its field of view simultaneously. Once the number of beam directions is set, the RIS can yield a correct estimation in the directions it is pointing, making it possible if there is more than one UE to be located at a time.

Improving gNB height estimation: A practical hybrid workflow is to let the three terrestrial gNBs perform the first pass: their geometry already brings a horizontal fix with an error of only a few meters. Once that azimuth is known, the RIS freezes its azimuth direction on the estimated bearing and carries out a rapid elevation sweep centered on that line of sight. The sweep can introduce at least one strong RIS echo whose extra time-of-flight provides a new vertical constraint, collapsing the tall error ellipsoid that otherwise plagues terrestrial layouts. Even a single elevation sweep at the correct azimuth typically cuts the vertical RMS error by an order of magnitude while adding only a marginal computational burden.

7.3 Potential Improvements

The RIS positioning can be further improved if instead of employing a passive RIS we used a hybrid RIS approach. A hybrid RIS (HRIS) fitted with a few receive elements can first listen to the UE's uplink SRS signal [37].
Upon reception, the HRIS can apply a spectral estimate (e.g. MUSIC spectral estimate), which gives the azimuth and elevation of the UE almost instantly. Armed with this coarse direction, the HRIS no longer has to sweep the entire 20×30 beam grid, it re-uses only a small subset of high-gain beam sweeps before the PRS is processed. Replacing the exhaustive scan with this two-step detect and refine procedure could cut down the computational effort and on-air reference overhead while introducing extra hardware. By implementing a HRIS and UE conectivity, there would exist a clock bias As antenna technology continues to miniaturize, future UEs will be able to host larger multi-element arrays. With more onboard antennas and the necessary RF chains, the UE itself could run spectral estimation algorithms, complementing the HRIS and further tightening the overall positioning accuracy.

7.3.1 Sub-step angular refinement via parabolic interpolation

After computing the correlation amplitude at each discrete steering angle ϕ_k (with uniform step) , we can identify the index k at which the correlation reaches its maximum. Provided $1 < k < N$ (the peak is not on the boundary), we extract the three neighbouring amplitudes:

$$v_- = v(\phi_{k^*-1}), \quad v_0 = v(\phi_{k^*}), \quad v_+ = v(\phi_{k^*+1}). \tag{7.1}$$

We then approximate these three points by a quadratic function (a parabola) whose vertex corresponds to the true peak location. For equally spaced angles, the parabola's maximum lies at

$$\phi_{\text{est}} \;=\; \phi_{k^*} \;+\; \frac{\Delta\phi}{2}\,\frac{v_- - v_+}{v_- - 2\,v_0 + v_+}. \tag{7.2}$$

This closed-form interpolation "half-steps" between the coarse 2° grid points, driving the maximum angular error from ±1° down to well below 0.5°. By combining a modest beam grid with sub-degree refinement, we can significantly boost RIS performance without exploding complexity. This could be done in a scenario in to improve the worst-case positioning error, were the UE lays in the middle of the beam sweep.

7.4 Future Work

Several avenues for improvement and further research have become apparent:

- **Cramér–Rao Lower Bound**. Although this thesis does not dive into a CRLB derivation, a full analysis would establish the fundamental lower bound on positioning error and clarify the main contributors to variance in both gNB-only and RIS-assisted cases.
- **Hybrid or active RIS**. Equipping a handful of tiles with low-noise receivers would let the panel run MUSIC-style angle estimation and skip the exhaustive 20×30 beam sweep, cutting both control traffic and update time. Furthermore, an active RIS could be used to enhance the beam gain without tightening the beam. However, it would require an advanced hardware complexity.
- **Sub-step beam refinement**. Implementing the parabolic interpolation described in Eq. (7.2) would halve the angular grid error from $\pm 1^\circ$ to below 1° without densifying the sweep, provided that the signal strength is sufficient.
- **Experimental validation**. Field measurements in an urban macro cell would validate the link-budget assumptions (foliage loss, façade reflections) and refine the power and delay thresholds derived analytically.

By closing the gap between theoretical promise and practical deployment, this work lays the foundation for cost-effective, meter positioning in the 6G era and beyond.

Appendix: Source Code

In case the GitHub link is not accessible, the complete MATLAB code used in this work is provided below:

```
%% OTDOA simulation using PRS and RIS
% 1. SCENARIO CONFIGURATION
nFrames = 1;
fc = 3e9;
numgNBs = 5;
rng('default');

% Wavelength
c = physconst("lightspeed");
lambda = c/fc;

% RIS parameters
ris.Enable = true;
ris.Size = [29 29 1]; %Ny x Nz x Npol

% RIS element size
ris.dx = lambda/2;
ris.dy = lambda/2;
% Amplitude of reflection coefficients of each RIS element
ris.A = 0.8;

% Positions
ris.Pos=[3715.11,7532.00,12]; % 2500m and 30   in azimut from gNB{1}
gNBPos= getgNBPositions(5);
gNBPos{1} = [2465.11, 5366.94, 25]; % Added myself for the simulation
gNBPos{3} = gNBPos{1}+[5000,5000,0]; % Added for the baseline
gNBPos{4} = gNBPos{1}+[-5000,5000,0]; % Added for the baseline
angleUE=deg2rad(180);
step = 10;
iter=20;

initial = 80;
distance2UE= [sqrt((initial+(iter-1)*step)^2 - 10^2)*cos(angleUE), sqrt((initial
```

```
    +(iter-1)*step)^2 - 10^2)*sin(angleUE), -10]; %
UEPos = ris.Pos + distance2UE;


idxMin = choosegNB(gNBPos, ris.Pos, UEPos);
% idxMin = 1;  If we allways want to use the first gNB

% 2. CARRIER OBJECT CONFIGURATION
cellIds = randperm(1008,numgNBs) - 1;

% Configure carrier properties
carrier = repmat(nrCarrierConfig,1,numgNBs);
for gNBIdx = 1:numgNBs
    carrier(gNBIdx).NCellID = cellIds(gNBIdx);

end

RIScarrier=pre6GCarrierConfig("NSizeGrid", carrier(idxMin).NSizeGrid, "
    SubcarrierSpacing", carrier(idxMin).SubcarrierSpacing);
RIScarrier.NCellID=carrier(idxMin).NCellID;
validateCarriers(carrier);

% 3. PRS CONFIGURATION
% Slot offsets of different PRS signals
prsSlotOffsets = 0:2:(2*numgNBs - 1);
prsIDs = randperm(4096,numgNBs) - 1;

% Configure PRS properties
prs = nrPRSConfig;
prs.PRSResourceSetPeriod = [10 0];
prs.PRSResourceOffset = 0;
prs.PRSResourceRepetition = 1;
prs.PRSResourceTimeGap = 1;
prs.MutingPattern1 = [];
prs.MutingPattern2 = [];
prs.NumRB = 52;
prs.RBOffset = 0;
prs.CombSize = 12;
prs.NumPRSSymbols = 12;
prs.SymbolStart = 0;
prs = repmat(prs,1,numgNBs);
for gNBIdx = 1:numgNBs
    prs(gNBIdx).PRSResourceOffset = prsSlotOffsets(gNBIdx);
    prs(gNBIdx).NPRSID = prsIDs(gNBIdx);

end
RISprs=prs(gNBIdx);
```

```
79
80
81 % 4. PDSCH CONFIGURATION
82 pdsch = nrPDSCHConfig;
83 pdsch.PRBSet = 0:51;
84 pdsch.SymbolAllocation = [0 14];
85 pdsch.DMRS.NumCDMGroupsWithoutData = 1;
86 pdsch = repmat(pdsch,1,numgNBs);
87 RISpdsch = pdsch(idxMin);
88 validateNumLayers(pdsch);
89
90 % 5. PATH LOSS CONFIGURATION
91
92 plCfg = nrPathLossConfig;
93 plCfg.Scenario = 'Uma';
94
95 % 6. RESOURCES GENERATION (PRS y PDSCH)
96 totSlots = nFrames*carrier(1).SlotsPerFrame;
97 prsGrid = cell(1,numgNBs);
98 dataGrid = cell(1,numgNBs);
99 for slotIdx = 0:totSlots-1
100     [carrier(:).NSlot] = deal(slotIdx);
101     [prsSym,prsInd] = deal(cell(1,numgNBs));
102     for gNBIdx = 1:numgNBs
103         % Create an empty resource grid spanning one slot in time domain
104         slotGrid = nrResourceGrid(carrier(gNBIdx),1);
105
106         % Generate PRS symbols and indices
107         prsSym{gNBIdx} = nrPRS(carrier(gNBIdx),prs(gNBIdx));
108         prsInd{gNBIdx} = nrPRSIndices(carrier(gNBIdx),prs(gNBIdx));
109
110         % Map PRS resources to slot grid
111         slotGrid(prsInd{gNBIdx}) = prsSym{gNBIdx};
112         prsGrid{gNBIdx} = [prsGrid{gNBIdx} slotGrid];
113     end
114     % Transmit data in slots in which the PRS is not transmitted by any of
115     % the gNBs (to control the hearability problem)
116     for gNBIdx = 1:numgNBs
117         dataSlotGrid = nrResourceGrid(carrier(gNBIdx),1);
118         if all(cellfun(@isempty,prsInd))
119             % Generate PDSCH indices
120             [pdschInd,pdschInfo] = nrPDSCHIndices(carrier(gNBIdx),pdsch(gNBIdx))
    ;
121
122             % Generate random data bits for transmission
123             data = randi([0 1],pdschInfo.G,1);
124             % Generate PDSCH symbols
```

```
125             pdschSym = nrPDSCH(carrier(gNBIdx),pdsch(gNBIdx),data);
126
127             % Generate demodulation reference signal (DM-RS) indices and symbols
128             dmrsInd = nrPDSCHDMRSIndices(carrier(gNBIdx),pdsch(gNBIdx));
129             dmrsSym = nrPDSCHDMRS(carrier(gNBIdx),pdsch(gNBIdx));
130
131             % Map PDSCH and its associated DM-RS to slot grid
132             dataSlotGrid(pdschInd) = pdschSym;
133             dataSlotGrid(dmrsInd) = dmrsSym;
134         end
135         dataGrid{gNBIdx} = [dataGrid{gNBIdx} dataSlotGrid];
136     end
137 end
138 RISprsGrid = prsGrid{idxMin};
139
140
141 % 7. OFDM MODULATION OF PRS AND DATA SIGNAL AT EACH GNB
142
143
144 txWaveform = cell(1,numgNBs);
145 for waveIdx = 1:numgNBs
146     carrier(waveIdx).NSlot = 0;
147     txWaveform{waveIdx} = nrOFDMModulate(carrier(waveIdx),prsGrid{waveIdx} ...
148         + dataGrid{waveIdx});
149 end
150 % Compute OFDM information using first carrier, assuming all carriers are
151 % at same sampling rate
152 ofdmInfo = nrOFDMInfo(carrier(1));
153
154 %RIS channel configuration
155 risCh = hpre6GRISChannel("SampleRate",ofdmInfo.SampleRate,"RISSize", ...
156     ris.Size,"CarrierFrequency",fc);
157
158 %Angle calculation
159 [azA, elA, azD, elD, azRG, elRG, distRG] = computeAoAandAoD(UEPos, ris.Pos, ...
160     gNBPos{idxMin});
161 fprintf("geometric AoD     Az: %.2f  , El: %.2f  \n", rad2deg(azD), ...
162     rad2deg(elD));
163 % DIRECTIVITY ESTIMATION -> GAIN
164 [th, phi, gain] = calculateRISgainCoeff(ris.Enable, risCh, azD, ...
165     elD, ris);
166
167 % 8. ADD RIS DELAY AND PATH LOSS
168 sampleDelay = zeros(1,numgNBs);
169 radius = cell(1,numgNBs);
170 for gNBIdx = 1:numgNBs
171    radius{gNBIdx} = rangeangle(gNBPos{gNBIdx}',UEPos');
```

```
172     delay = radius{gNBIdx}/c;                          % Delay in seconds
173     sampleDelay(gNBIdx) = round(delay*ofdmInfo.SampleRate);   % Delay in samples
174 end
175 rxWaveform = zeros(length(txWaveform{1}) + max(sampleDelay),1);
176 rx = cell(1,numgNBs);
177 for gNBIdx = 1:numgNBs
178     % Calculate path loss for each gNB and UE pair
179     losFlag = true; % Assuming the line of sight (LOS) flag as true, as we are
    only considering the LOS path delays in this example
180     PLdB = nrPathLoss(plCfg,fc,losFlag,gNBPos{gNBIdx}(:),UEPos(:));
181     if PLdB < 0 || isnan(PLdB) || isinf(PLdB)
182         error('nr5g:invalidPL',"Computed path loss (" + num2str(PLdB) + ...
183             ") is invalid. Try changing the UE or gNB positions, or path loss
    configuration.");
184     end
185     PL(gNBIdx) = 10^(PLdB/10);
186
187     % Add delay, pad, and attenuate
188     rx{gNBIdx} = [zeros(sampleDelay(gNBIdx),1); txWaveform{gNBIdx}; ...
189                 zeros(max(sampleDelay)-sampleDelay(gNBIdx),1)]/sqrt(PL(gNBIdx));
190
191     % Sum waveforms from all gNBs
192     rxWaveform = rxWaveform + rx{gNBIdx};
193 end
194
195
196 % 1) Distances gNB-to-RIS and RIS-to-UE
197 d_g2r     = norm(gNBPos{idxMin} - ris.Pos);  % m
198 d_r2u     = norm(ris.Pos     - UEPos);      % m
199
200 % 2) Delay in samples
201 delay_g2r = round((d_g2r/c) * ofdmInfo.SampleRate);
202 delay_r2u = round((d_r2u/c) * ofdmInfo.SampleRate);
203 totalDelay= delay_g2r + delay_r2u ;
204
205 % 3) Path-loss constants
206 PLlin_g2r = 10^( nrPathLoss(plCfg,fc,true, gNBPos{idxMin}(:), ris.Pos(:)) / 10 )
    ;
207 PLlin_r2u = 10^( nrPathLoss(plCfg,fc,true, ris.Pos(:),      UEPos(:)) / 10 );
208
209 % Use the gNB{1} tx signal
210 txRef   = txWaveform{idxMin};      % [nSamples 1]
211 nSamp   = numel(txRef);
212 numGphi    = numel(gain(:,1));
213 numGth = numel(gain(1,:));
214 outLen  = totalDelay + nSamp;
215
```

```
% Pre-aloccate: outLen numGphixnumGth
rxRIS = zeros(outLen,numGphi, numGth);

% For each RIS coefficient:
for k = 1:numGphi
    for l = 1:numGth
    % a) Attenuation  g N B RIS
    RISsignal = txRef / sqrt(PLlin_g2r);

    % b) Aplicar ganancia del RIS (vector    gain   )
    RISsignal = RISsignal * gain(k,l)*ris.A;

    % c) Attenuation  R I S UE
    RISsignal = RISsignal / sqrt(PLlin_r2u);
    RISsignal_nodelay(:,k,l) = RISsignal; %To later calculate SNR
    % d) Padding for the total geometric delay
    rxRIS(:,k,l) = [ zeros(totalDelay,1);    % ceros first
                     RISsignal ];                  % processed signal
    end
end

% Equal the samples in RIS and gNB
lenGNB = size(rxWaveform,1);
lenRIS = size(rxRIS(:,1),    1);
diflen = abs(lenRIS - lenGNB);
% If RISrx is larger, we padd
if lenRIS > lenGNB
    rxWaveform_padded = [ rxWaveform;
                          zeros(diflen, 1) ];
else
   rxWaveform_padded = rxWaveform;
   rxRIS(end+1:end+diflen, :, :) = 0;
end

% ADD noise
ue=[5e3 0 2];
gnB=[0 0 28];
pathLoss5km_dB  = nrPathLoss(plCfg,fc,true,ue(:),gnB(:));
pathLoss5km_lin = 10.^(-pathLoss5km_dB/10);
SNR_dB  = 10; % Wanted SNR at 5km
SNR_lin = 10.^(SNR_dB/10);
N0      = pathLoss5km_lin/(sqrt(2)*double(ofdmInfo.Nfft)*SNR_lin);
noise = N0*complex(randn(size(rxWaveform_padded)),randn(size(rxWaveform_padded))
    );
noise_notpadded = noise((numel(noise)-numel(txWaveform{1})):end);

rxWaveform_padded= rxWaveform_padded/10; % Extra Attenuation (10)
```

```
rxnoisy = rxWaveform_padded + noise;
rxRISnoisy = rxRIS + rxWaveform_padded+ noise;

% 9.TOA ESTIMATION

% CALCULATE RIS CORRELATION (1024xNgphixNgth)
delayRIS=zeros(numGphi, numGth);
delaygNB=zeros(numGphi, numGth);


Ncorr = ceil(ofdmInfo.Nfft * RIScarrier.SubcarrierSpacing/15);
for GphiIdx = 1:numGphi
    for GthIdx = 1:numGth

     [~,RISmag] = nrTimingEstimate(RIScarrier, ...
         rxRISnoisy(:,GphiIdx,GthIdx),RISprsGrid);
     corrRIS{GphiIdx, GthIdx} = RISmag(1:(Ncorr));

     [pks, locs] = findpeaks(corrRIS{GphiIdx, GthIdx}, ...
         'SortStr','descend', 'NPeaks',2);
     % Findpeaks gives the highest two peaks, sort them in time of arrival
     if locs(2) < locs(1)
     temp = locs(1);
     locs(1) = locs(2);
     locs(2) = temp;
     pks = [pks(2),pks(1)];
     end

     peak1(GphiIdx,GthIdx)  = pks(1); % Estimated gNB peak
     peak2(GphiIdx,GthIdx)  = pks(2); % Estimated RIS peak

     delaygNB(GphiIdx,GthIdx) = locs(1)-1; % Estimated gNB sample delay
     delayRIS(GphiIdx,GthIdx) = locs(2)-1; % Estimated RIS sample delay

    end
end
% Add all the correlation, the correct phi and th should be NyxNz
sumCorr = cellfun(@sum, corrRIS);
[bestValue, linIdx]      = max(sumCorr(:));
[bestPhiIdx, bestThIdx]  = ind2sub(size(sumCorr), linIdx);


bestRISPeakValue = peak2(bestPhiIdx, bestThIdx);

% Range difference estimation:
difDist =  c*(delayRIS(bestPhiIdx, bestThIdx) - delaygNB(bestPhiIdx, bestThIdx))
    /ofdmInfo.SampleRate;
```

```
308
309 % Angle estimation:
310 estAz = (phi(1,bestPhiIdx));
311 estEl = th(bestThIdx);
312
313 % Graph the correlation result:
314 Fs   = ofdmInfo.SampleRate;
315 tMag = (0:numel(corrRIS{1})-1)/Fs;
316
317 figure;
318 plot(tMag, corrRIS{bestPhiIdx, bestThIdx}, 'LineWidth',1.4);
319 xlabel('Time (s)');
320 ylabel('Correlation magnitude');
321 title('Correlation (mag) from nrTimingEstimate');
322 grid on;
323
324 % SNR calculation, it is advisable to do it if the correlations have been
325 % done separatedly, if not, results may be not correct
326 S_gNB = mean(abs(txWaveform{idxMin}/sqrt(PL(idxMin))).^2);
327 S_RIS = mean(abs(RISsignal_nodelay(bestPhiIdx,bestThIdx)).^2);
328 SNR_lin        = [ S_gNB, S_RIS ] ./ mean(abs(noise_notpadded));
329 SNRdB     = 10*log10( SNR_lin );
330
331
332
333
334 % 10. UE POSITION ESTIMATION:
335
336
337 % RIS
338 xyz_est = solvePOS(difDist, distRG, azRG, estAz, gNBPos{idxMin}, estEl, -elRG);
339
340 % Error computation
341
342 EstErrRIS  =  norm(UEPos - xyz_est);
343 EstErrRISX = abs( UEPos(1) - xyz_est(1) );
344 EstErrRISY = abs( UEPos(2) - xyz_est(2) );
345 EstErrRISZ = abs( UEPos(3) - xyz_est(3) );
346
347
348
349 %% Functions %%
350 function [azA, elA, azD, elD, azRG, elRG, distRG] = computeAoAandAoD(UEPos,
    RISPos, gNBPos)
351 % computeAoAandAoD  Calculates  U E RIS  and  R I S gNB  angles, always positive
352 %   [azA, elA, azD, elD, azRG, elRG] = computeAoAandAoD(UEPos, RISPos, gNBPos)
353 %     azA, elA  : azimuth and elevation of arrival  U E RIS  (input angle)
```

```
%     azD, elD  : azimuth and elevation of departure  R I S UE  (output angle)
%     azRG, elRG: azimuth and elevation of departure  R I S gNB
%     distRG    : distance between RIS and gNB
%   All outputs are in radians in the range [0, 2*pi).

    % ---- UE     RIS
    dx  = RISPos(1) - UEPos(1);
    dy  = RISPos(2) - UEPos(2);
    dz  = RISPos(3) - UEPos(3);
    azA = atan2(dy, dx);
    elA = atan2(dz, hypot(dx, dy));

    % ---- RIS     UE (inverse)
    azD = azA + pi;
    elD = -elA;

    % ---- RIS     gNB
    dx2 = gNBPos(1) - RISPos(1);
    dy2 = gNBPos(2) - RISPos(2);
    dz2 = gNBPos(3) - RISPos(3);
    azRG = atan2(dy2, dx2);
    elRG = atan2(dz2, hypot(dx2, dy2));
    distRG = sqrt(dx2^2 + dy2^2 + dz2^2);

    % --- Ensure positive ranges [0, 2*pi)
    azA  = mod(azA,  2*pi);
    azD  = mod(azD,  2*pi);
    azRG = mod(azRG, 2*pi);

end









function idxMin = choosegNB(gNBPos, RISPos, UEPos)
% choosegNB   Selects the index of the gNB on the same    side    as the UE
%             (relative to the RIS) and, if there are several, the one closest
    to the RIS.
%
%   gNBPos : 1 N  cell array where gNBPos{i} = [x y z] of the i-th gNB
%   RISPos : [x y z] of the RIS
%   UEPos  : [x y z] of the UE
%
%   idxMin : index (1  N  ) of the selected gNB

```

```
400     %  U E RIS  vector in XY
401     ueVec = UEPos(1:2) - RISPos(1:2);
402
403     % Initialize distances to Inf
404     N = numel(gNBPos);
405     dist2R = inf(N,1);
406
407     % Loop through each gNB
408     for i = 1:N
409         pos = gNBPos{i}(:);
410         relX = pos(1) - RISPos(1);
411
412         % Check if it's on the same    half    (X side):
413         if ueVec(1) * relX >= 0
414             % Calculate distance to the RIS in the XY plane
415             dist2R(i) = norm(pos - RISPos(1:2));
416         end
417     end
418
419     % Choose the minimum among those that meet the condition
420     [minDist, idxMin] = min(dist2R);
421     if isinf(minDist)
422         error("There is no gNB on the same side as the UE.");
423     end
424 end
425
426 function xy_est = solvePOS(drest, dgNBRIS, betaAz, alphaAz, gNBPOS, estTH, psi)
427
428 alpha = pi - alphaAz ;
429 beta = betaAz - pi;
430
431
432 Xg =  gNBPOS(1);
433 Yg =  gNBPOS(2);
434 Zg = gNBPOS(3);
435 num = (dgNBRIS)^2 - (dgNBRIS - drest)^2;
436 den = 2*( dgNBRIS*(1 - cos(psi)*cos(estTH)*(sin(beta)*sin(alpha) - cos(beta)*cos
        (alpha)) + sin(psi)*sin(estTH)) - drest);
437 if abs(den) < eps
438     error('very small denominator; revise beta and alpha.');
439 end
440 dRU = num / den;
441
442
443 % XYZ
444
445
```

```
446 x = dgNBRIS*cos(beta)*cos(psi) - dRU*cos(alpha)*cos(estTH) + Xg;
447 y = dgNBRIS*sin(beta)*cos(psi) + dRU*sin(alpha)*cos(estTH) + Yg;
448 z = dgNBRIS*sin(psi) + dRU*sin(estTH) + Zg;
449 xy_est = [x, y, z];
450 end
451
452
453 function [thList, phiList, gain] = calculateRISgainCoeff(enableRIS, risCh, ueAz,
        ueTh, ris)
454 % calculateRISgainCoeff   RIS coefficients with controlled beamwidth via
       tapering and iterative pattern plotting
455 %   enableRIS: flag to enable RIS optimization
456 %   risCh    : hpre6GRISChannel object
457 %   carrier  : carrier config
458 %   ueAz     : known UE azimuth (rad)
459
460 % 1) Constants & RIS geometry
461 c      = physconst("lightspeed");
462 lambda = c/risCh.CarrierFrequency;
463
464 risSize = risCh.RISSize;  % [M N P]
465 M = risSize(1);
466 N = risSize(2);
467 P = risSize(3);
468 dz = ris.dx/lambda;
469 dy = ris.dy/lambda;
470
471
472 anY = ones(1,M);
473 anZ = ones(1,N);
474
475 phiList = deg2rad(180):-deg2rad(5):deg2rad(90);
476
477
478
479 thList = [
480   -0.523598775598303, -0.339836909454126, -0.252680255142078,
      -0.201357920790330, ...
481   -0.167448079219690, -0.143347568905365, -0.125327831168065,
      -0.111341014340964, ...
482   -0.100167421161560, -0.0910347780374153, -0.0834300866106150,
      -0.0769991406568236, ...
483   -0.0714894498855205, -0.0667161484102252, -0.0625407617964915,
      -0.0588575059470812, ...
484   -0.0555841732809176, -0.0526559082615699, -0.0500208568057700,
      -0.0476370626244031, ...
485   -0.0454702124169971, -0.0434919707901158, -0.0416787324225779,
```

```
    -0.0400106743539889, ...
  -0.0384710274073283, -0.0370455098120920, -0.0357218823980788,
    -0.0344895959616788, ...
  -0.0333395092613021, -0.0322636616682469
];

alphaListY = -2*pi * dy * sin(phiList);
alphaListZ = -2*pi * dz * sin(thList);
K    = numel(phiList);
L    = numel(thList);

if ~enableRIS
    % RIS turned OFF
    gain = zeros(K,L);
    return;
end


for k = 1:K

    for n = 1:L
       % We extract the gain from the specific phiList(k) and thList(n)
    [gainFA,~,~,~]=array2d(anY,anZ,alphaListY(k),alphaListZ(n),dy,dz,ueAz,ueTh,
    phiList,thList);

    gain(k,n)      = gainFA;
    end
end
end

function [gain,FAaz,FAth,Daz]=array2d(anY,anZ,alfaY,alfaZ,dy,dz,angAz,angEl,phi,
    th)

% Modified function from Josep Parron, I added one dimension extra

%Verificando las entradas
[M,N]=size(anY);
if (M~=1) | (N<1), error('an debe ser un vector fila'); end;
aux=size(alfaY);
if (aux~=1), error('alfa tener dimensiones 1x1');end;
aux=size(dy);
if (aux~=1), error('d tener dimensiones 1x1');end;
if (dy<0), error('d tiene que ser mayor que cero');end;


%Angulo electrico
dpsi = pi/1000;
```

```
529 lenY = 2*pi*(1+2*dy);
530 lenZ = 2*pi*(1+2*dz);
531 n_ptosY = lenY/dpsi;
532 n_ptosZ = lenZ/dpsi;
533 psi_phi=linspace(-pi-2*pi*dy+alfaY,+pi+2*pi*dy+alfaY,n_ptosY);
534 psi_th = linspace(-pi-2*pi*dy+alfaZ,+pi+2*pi*dy+alfaZ,n_ptosZ);
535 %Diagrama de radiacion en el espacio electrico
536 FA_az=abs(freqz(anY,1,psi_phi));
537 FA_el=abs(freqz(anY,1,psi_th));
538 %Angulo real
539
540
541 angfa= linspace(pi,0, 2*360+1);
542 %psi=k*d*cos(th)+alfa
543 psi_re_az=2*pi*dy*cos(angfa)+alfaY;
544 psi_re_th=2*pi*dz*cos(angfa)+alfaZ;
545 %Diagrama de radiacion en el espacio real
546 FAaz=abs(freqz(anY,1,psi_re_az));
547 FAth=abs(freqz(anZ,1,psi_re_th));
548 %Calculo directividad
549 raz=find((psi_phi > min(psi_re_az)) & (psi_phi < max(psi_re_az)));
550 rel=find((psi_th > min(psi_re_th)) & (psi_th < max(psi_re_th)));
551 [~, phiest] = min(abs(angfa - angAz + pi/2));            % mejor azimut
552 Daz=4*pi*dy*abs(FAaz(phiest)).^2/dpsi/sum(abs(FA_az(raz).^2));
553
554 [~, thest] = min(abs(angfa  - (pi/2- angEl)));              % mejor elevación
555 Del=4*pi*dz*abs(FAth(thest)).^2/dpsi/sum(abs(FA_el(rel).^2));
556 gain=Daz*Del;
557
558 end
559 %% From here on if you want to compile the code you have to insert
560 % the functions validateCarriers, validateNumLayers, colors and plotGrid if
561 % you want to plot, the other functions have been omitted or are not
562 % necessary to compile. Also it is necessary to have the hpre6G functions
    installed
```

Bibliography

[1] Nokia. (2024) Spectrum for 6g explained. Nokia Newsroom. Accessed: 14-Feb-2025. [Online]. Available: https://www.nokia.com/about-us/newsroom/articles/spectrum-for-6G-explained/

[2] PyLayers Development Team. (2017) Pylayers: Site specific radio propagation simulator. GitHub repository. Accessed: Mar-2025. [Online]. Available: https://pylayers.github.io/pylayers/auto_examples/plot_exAbsGas.html

[3] J. Parrón Granados, "Radio communications notes," Class notes, Universitat Autònoma de Barcelona, 2024, in-class material for the course on Radio Communications.

[4] S. Ju, S. H. A. Shah, M. A. Javed, J. Li, G. Palteru, J. Robin, Y. Xing, O. Kanhere, and T. S. Rappaport, "Scattering mechanisms and modeling for terahertz wireless communications," in *ICC 2019 - 2019 IEEE International Conference on Communications (ICC)*, 2019, pp. 1–7.

[5] M. Di Renzo, A. Zappone, M. Debbah, M.-S. Alouini, C. Yuen, J. de Rosny, and S. Tretyakov, "Smart radio environments empowered by reconfigurable intelligent surfaces: How it works, state of research, and the road ahead," *IEEE Journal on Selected Areas in Communications*, vol. 38, no. 11, pp. 2450–2525, 2020.

[6] Y. Feng, Q. Hu, K. Qu, W. Yang, Y. Zheng, and K. Chen, "Reconfigurable intelligent surfaces: Design, implementation, and practical demonstration," *Electromagnetic Science*, vol. 1, no. 2, pp. 1–21, 2023.

[7] Z. Wei, Y. Wang, L. Ma, S. Yang, Z. Feng, C. Pan, Q. Zhang, Y. Wang, H. Wu, and P. Zhang, "5g prs-based sensing: A sensing reference signal approach for joint sensing and communication system," *IEEE Transactions on Vehicular Technology*, vol. 72, no. 3, pp. 3250–3263, 2023.

[8] C. J. Pawase and K. Chang, "5g-nr physical layer-based solutions to support high mobility in 6g non-terrestrial networks," *Drones*, vol. 7, no. 3, 2023. [Online]. Available: https://www.mdpi.com/2504-446X/7/3/176

[9] MathWorks. (2025) Nr positioning using prs toolbox. MATLAB PRS Positioning Toolbox User Manual. Previous version; Accessed: 2-Apr-2025. [Online]. Available: https://es.mathworks.com/help/5g/ug/nr-prs-positioning.html

[10] Google LLC. (2025) Google maps. Data © 2025 Google; Accessed: 19-May-2025. [Online]. Available: https://maps.google.com

[11] ShareTechnote. (2025) 5g sharetechnote. Accessed: Mar-2025. [Online]. Available: https://www.sharetechnote.com/html/5G/5G_FrameStructure.html

[12] M. Alghisi and L. Biagi, "Positioning with gnss and 5g: Analysis of geometric accuracy in urban scenarios," *Sensors*, vol. 23, no. 4, 2023. [Online]. Available: https://www.mdpi.com/1424-8220/23/4/2181

[13] T. S. Rappaport, Y. Xing, O. Kanhere, S. Ju, A. Madanayake, S. Mandal, A. Alkhateeb, and G. C. Trichopoulos, "Wireless communications and applications above 100 ghz: Opportunities and challenges for 6g and beyond," *IEEE Access*, vol. 7, pp. 78 729–78 757, 2019.

[14] T. Oyedare, V. K. Shah, D. J. Jakubisin, and J. H. Reed, "Interference suppression using deep learning: Current approaches and open challenges," *IEEE Access*, vol. 10, p. 66238–66266, 2022. [Online]. Available: http://dx.doi.org/10.1109/ACCESS.2022.3185124

[15] C. Huang, S. Hu, G. C. Alexandropoulos, A. Zappone, C. Yuen, R. Zhang, M. D. Renzo, and M. Debbah, "Holographic mimo surfaces for 6g wireless networks: Opportunities, challenges, and trends," *IEEE Wireless Communications*, vol. 27, no. 5, pp. 118–125, 2020.

[16] Q. Wu and R. Zhang, "Towards smart and reconfigurable environment: Intelligent reflecting surface aided wireless network," *IEEE Communications Magazine*, vol. 58, no. 1, pp. 106–112, 2020.

[17] B. M. Heffernan, Y. Kawamoto, K. Maekawa, J. Greenberg, R. Amin, T. Hori, T. Tanigawa, T. Nagatsuma, and A. Rolland, "60 gbps real-time wireless communications at 300 ghz carrier using a kerr microcomb-based source," *APL Photonics*, vol. 8, no. 6, p. 066106, 06 2023. [Online]. Available: https://doi.org/10.1063/5.0146957

[18] Y. Tokizane, S. Okada, T. Kikuhara, H. Kishikawa, Y. Okamura, Y. Makimoto, K. Nishimoto, T. Minamikawa, E. Hase, J.-I. Fujikata, M. Haraguchi, A. Kanno, S. Hisatake, N. Kuse, and T. Yasui, "Wireless data transmission in a 560-ghz band using low-phase-noise terahertz wave generated by photomixing of a pair of distributed feedback lasers injection-locking to kerr micro-resonator soliton comb," 2023. [Online]. Available: https://arxiv.org/abs/2308.02999

[19] Electronics Stack Exchange. (2018) Why microwave links on cell towers have high frequency? Accessed: 03-Mar-2025. [Online]. Available: https://electronics.stackexchange.com/questions/396573/why-microwave-links-on-cell-towers-have-high-frequency

[20] M. Solé i Gasset, "Notes on multipath," Class notes, *Aplicacions Multidisciplinars I*, 2024, internal teaching material.

[21] J. Parrón, "Capítulo 4: Agrupación de antenas y capítulo 2: Fundamentos de radiación," Class notes, *Apuntes de Antenas*, 2024.

[22] A. Cardama, L. Jofre, J. Rius, and J. Romeu, *Antenas*, 2nd ed. Barcelona, España: Edicions UPC, 2002.

[23] M. M. Amri, "Recent trends in the reconfigurable intelligent surfaces (ris): Active ris to brain-controlled ris," in *2022 IEEE International Conference on Communication, Networks and Satellite (COMNETSAT)*, 2022, pp. 299–304.

[24] I. Jung, Z. Peng, and Y. Rahmat-Samii, "Recent advances in reconfigurable electromagnetic surfaces: Engineering design, full-wave analysis, and large-scale optimization," *Electromagnetic Science*, vol. 2, no. 3, pp. 1–25, 2024.

[25] S. Kumar Reddy Vuyyuru, L. Hao, M. Rupp, S. A. Tretyakov, and R. Valkonen, "Modeling ris from electromagnetic principles to communication systems—part i: Synthesis and characterization of a scalable anomalous reflector," *IEEE Transactions on Antennas and Propagation*, vol. 73, no. 3, pp. 1743–1755, 2025.

[26] W. Tang, X. Chen, M. Z. Chen, J. Y. Dai, Y. Han, M. D. Renzo, S. Jin, Q. Cheng, and T. J. Cui, "Path loss modeling and measurements for reconfigurable intelligent surfaces in the millimeter-wave frequency band," *IEEE Transactions on Communications*, vol. 70, no. 9, pp. 6259–6276, 2022.

[27] M. Sode, M. Ponschab, L. N. Ribeiro, S. Haesloop, E. Tohidi, M. Peter, S. Stańczak, B. H. Mohamed, W. Keusgen, H. Mellein, E. Yassin, and B. Schroeder, "Reconfigurable intelligent surfaces for 6g mobile networks: An industry rd perspective," *IEEE Access*, vol. 12, pp. 163 155–163 171, 2024.

[28] R. Ghazalian, G. C. Alexandropoulos, G. Seco-Granados, H. Wymeersch, and R. Jäntti, "Joint 3d user and 6d hybrid reconfigurable intelligent surface localization," *IEEE Transactions on Vehicular Technology*, vol. 73, no. 10, pp. 15 302–15 317, 2024.

[29] Z. Cui, F. Minucci, R. Hersyandika, R. M. Alonso, A. P. Guevara, H. Sallouha, and S. Pollin, "Electric field evaluation of reconfigurable intelligent surface in wireless networks," in *2024 IEEE International Symposium on Dynamic Spectrum*

Access Networks (DySPAN). IEEE, May 2024, p. 420–428. [Online]. Available: http://dx.doi.org/10.1109/DySPAN60163.2024.10632800

[30] X. Mu, J. Xu, Y. Liu, and L. Hanzo, "Reconfigurable intelligent surface-aided near-field communications for 6g: Opportunities and challenges," *IEEE Vehicular Technology Magazine*, vol. 19, no. 1, pp. 65–74, 2024.

[31] 3GPP. (2025) 5g system overview. 3GPP. Accessed: 25-Jun-2025. [Online]. Available: https://www.3gpp.org/technologies/5g-system-overview

[32] MathWorks. (2025) Model reconfigurable intelligent surfaces with cdl channels. MathWorks 6G Exploration Library for 5G Toolbox Documentation. Accessed: 2-Apr-2025. [Online]. Available: https://es.mathworks.com/help/5g/ug/model-reconfigurable-intelligent-surfaces-with-cdl-channels.html

[33] E. J. Oughton and A. Jha, "Supportive 5g infrastructure policies are essential for universal 6g: Assessment using an open-source techno-economic simulation model utilizing remote sensing," *IEEE Access*, vol. 9, pp. 101 924–101 945, 2021.

[34] MathWorks. (2025) 5g nr positioning reference signals (prs). 5G Toolbox online documentation. Accessed: 02-Apr-2025. [Online]. Available: https://es.mathworks.com/help/5g/ug/5g-new-radio-prs.html

[35] ShareTechnote. (2025) 5g nr – synchronization signal block (ssb). Technical note (PDF); Accessed: 20-Jun-2025. [Online]. Available: https://www.sharetechnote.com/html/5G/5G_NR_SSB.html

[36] ——. (2025) 5g nr – channel status information (csi-rs). Accessed: 19-Jun-2025. [Online]. Available: https://www.sharetechnote.com/html/5G/5G_NR.html

[37] ——. (2025) 5g nr – sounding reference signal (srs). Accessed: 20-Jun-2025. [Online]. Available: https://www.sharetechnote.com/html/5G/5G_SRS.html